

AD-A159 178

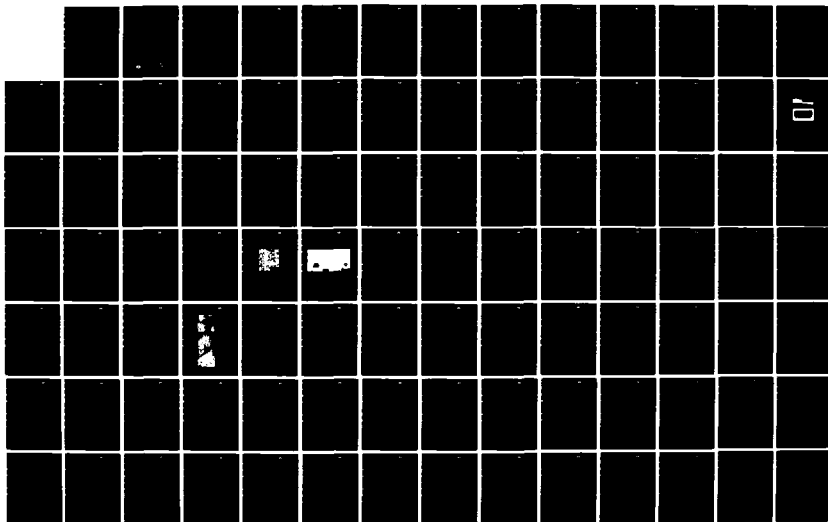
STRENGTHENING AND STRENGTH UNIFORMITY OF STRUCTURAL
CERAMICS(U) ROCKWELL INTERNATIONAL THOUSAND OAKS CA
SCIENCE CENTER F F LANGE ET AL APR 85 SC5295 4FR
AFOSR-TR-85-0731 F49620-81-C-0036

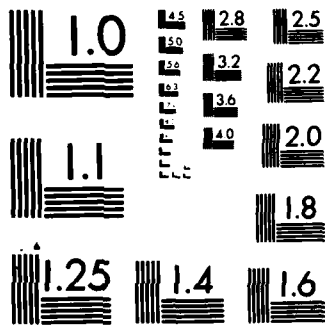
1/2

UNCLASSIFIED

F/G 11/2

NL





MICROCOPY RESOLUTION TEST CHART
NATIONAL BUREAU OF STANDARDS-1963-A

SC5295.4FR

SC5295.4FR
Copy No.

STRENGTHENING AND STRENGTH UNIFORMITY OF STRUCTURAL CERAMICS

FINAL REPORT FOR THE PERIOD
February 1, 1981 through January 31, 1985

AD-A159 170

CONTRACT NO. F49620-81-C-0036

Prepared for

Air Force Office of Scientific Research
Directorate of Electronic and Material Sciences
Building 410
Bolling Air Force Base, DC 20332

F.F. Lange/D.B. Marshall
Principal Investigators

April 1985

Approved for public release; distribution unlimited



Rockwell International
Science Center

DTIC
ELECTRIC
SEP 13 1985
D

DTIC FILE COPY

REPORT DOCUMENTATION PAGE

1a. REPORT SECURITY CLASSIFICATION UNCLASSIFIED		1b. RESTRICTIVE MARKINGS	
2a. SECURITY CLASSIFICATION AUTHORITY		3. DISTRIBUTION/AVAILABILITY OF REPORT Approved for public release; distribution unlimited	
2b. DECLASSIFICATION/DOWNGRADING SCHEDULE			
4. PERFORMING ORGANIZATION REPORT NUMBER(S) SC5295.4FR		5. MONITORING ORGANIZATION REPORT NUMBER(S) AFOSR/NE	
6a. NAME OF PERFORMING ORGANIZATION ROCKWELL INTERNATIONAL Science Center	6b. OFFICE SYMBOL <i>(If applicable)</i>	7a. NAME OF MONITORING ORGANIZATION AFOSR/NE	
6c. ADDRESS (City, State and ZIP Code) 1049 Camino Dos Rios Thousand Oaks, CA 91360		7b. ADDRESS (City, State and ZIP Code) Bolling AFB, D.C. 20332	
8a. NAME OF FUNDING/SPONSORING ORGANIZATION Air Force Office of Scientific Research	8b. OFFICE SYMBOL <i>(If applicable)</i>	9. PROCUREMENT INSTRUMENT IDENTIFICATION NUMBER Contract No. F49620-81-C-0036	
8c. ADDRESS (City, State and ZIP Code) Directorate of Electronic and Material Sciences Building 410 Bolling Air Force Base, D.C. 20332		10. SOURCE OF FUNDING NOS	
		PROGRAM ELEMENT NO 61102F	PROJECT NO. 2306
		TASK NO. A2	WORK UNIT NO.
11. TITLE <i>Include Security Classification:</i> STRENGTHENING & STRENGTH UNIFORMITY STRUCTURAL CERAMICS (U)			
12. PERSONAL AUTHOR(S) Lange, F.F., Marshall, D.B.			
13a. TYPE OF REPORT FINAL REPORT	13b. TIME COVERED FROM 02-01-81 TO 01-31-85	14. DATE OF REPORT (Yr., Mo., Day) April 1985	15. PAGE COUNT 109
16. SUPPLEMENTARY NOTATION			
17. COSATI CODES		18. SUBJECT TERMS <i>Continue on reverse if necessary and identify by block number.</i>	
FIELD	GROUP	SUB GR	
19. ABSTRACT <i>Continue on reverse if necessary and identify by block number.</i> The results of a four year study aimed at improving the strength and reliability of structural ceramics are summarized. Strength-degrading flaw populations were identified and processing methods were developed to eliminate each flaw population, thereby increasing the strength of $Al_2O_3-ZrO_2$ composites by a factor of three. The final year's work, which is reported in detail here, concentrated on the introduction of beneficial surface stresses by grinding, identification of strength-controlling characteristics of transformation toughened ceramics, and manipulation of microstructure by controlling grain growth. Requirements for inhibition of grain growth by several phase particles (particle size, volume fraction) were identified and grain-size control in transformation toughened materials was achieved by sintering in a two-phase field.			
20. DISTRIBUTION/AVAILABILITY OF ABSTRACT UNCLASSIFIED/UNLIMITED <input checked="" type="checkbox"/> SAME AS RPT. <input type="checkbox"/> DTIC USERS <input type="checkbox"/>		21. ABSTRACT SECURITY CLASSIFICATION UNCLASSIFIED	
22a. NAME OF RESPONSIBLE INDIVIDUAL Frank W. Hager		22b. TELEPHONE NUMBER <i>(Include Area Code)</i> (202) 767-4933	22c. OFFICE SYMBOL Y/E



TABLE OF CONTENTS

	<u>Page</u>
INTRODUCTION.....	1
LIST OF PUBLICATIONS RESULTING FROM PROGRAM.....	8
PERSONNEL INVOLVED IN PROGRAM.....	10
APPENDIX I RESIDUAL STRESSES IN MACHINED CERAMIC SURFACES.....	11
APPENDIX II GRAIN GROWTH PHENOMENA IN TWO-PHASE CERAMICS: AL ₂ O ₃ INCLUSIONS IN ZrO ₂	31
APPENDIX III TRANSFORMATION TOUGHENED ZrO ₂ : CORRELATIONS BETWEEN GRAIN CONTROL AND COMPOSITION IN THE ZrO ₂ -Y ₂ O ₃ SYSTEM.....	45
APPENDIX IV ON THE RETENTION OF EQUIAXED GRAIN STRUCTURE AFTER SUPERPLASTIC AND OTHER FORMS OF HIGH TEMPERATURE DEFORMATION.....	56
APPENDIX V STRENGTH CHARACTERISTICS OF TRANSFORMATION-TOUGHENED ZIRCONIA.....	72



Accession For	
NTIS CRA&I	
DTIC TAB	
Unannounced	
Justification	
By	
Distribution/	
Availability Codes	
Avail and/or	
Dist Special	
A-1	



INTRODUCTION

The goals of this work are to uncover flaw populations which limit strength, to identify the processing steps responsible for introducing the flaws, to develop new processing methods which eliminate flaw populations, and to identify methods of engineering special microstructures which also eliminate flaw populations - all with the underlying objective of increasing the reliability of structural ceramics.

During the first year's effort, flaw populations associated with hard and soft agglomerates, were identified as major strength limiting defects in sintered ceramics. Hard agglomerates originate during powder manufacture and soft agglomerates form during powder processing. Both types of agglomerates shrink differently relative to other agglomerates and the surrounding powder matrix to produce crack-like voids during sintering. The mechanism of formation of these crack-like voids was examined through model experiments. With insight provided by these experiments, processing methods based on colloidal treatment of powders were developed to minimize the agglomerate sizes and to consolidate powder compacts prior to sintering. Using these new powder processing methods, it was demonstrated that the strength of certain transformation toughened ceramics (which have a high potential strength due to their high fracture toughness) could be increased from 550 MPa to 1035 MPa. It was also demonstrated that post-sintering hot-gas isopressing (HIPing) could close crack-like voids produced by the differential shrinkage of agglomerates.

Effort during the second year concentrated on estimating the magnitude of the maximum stresses produced by differential shrinkage of agglomerates during sintering, and the control of other flaw populations, viz those associated with organic inclusions and large grains. Experimental results showed that that maximum stresses produced by differential shrinkage arise at low temperatures (during the early stages of sintering) where viscoelastic behavior of the powder compact is more elastic than viscous. This result



suggests that the stresses due to differential sintering, and thus, the likely formation of a crack-like void, might be controlled by decreasing the heating rate during sintering, i.e., by increasing the viscoelastic relaxation time constant. Experiments aimed at exploring this concept have been initiated under a related ONR contract concerned with the sintering behavior of ceramic powders. New processing methods aimed at controlling flaw populations associated with organic inclusions and large grains were also investigated. It was demonstrated that organic inclusions (e.g., lint, etc) which can be incorporated with the powder during manufacture (thereby making clean rooms ineffective), can be eliminated by using the following processing steps: 1) consolidating the powder compact; 2) burning the organic inclusions from the compact at a temperature below that required for sintering; 3) iso-pressing to close the voids left by removal of the inclusions; and 4) sintering. Using this organic-burn-out/iso-pressing method, the strength of a colloiddially processed, transformation toughened ceramic was increased from 1035 MPa to 1340 MPa.

The control of grain growth by inclusion phases was also studied, with the aim of eliminating defects associated with large grains. Unlike metal systems where grain growth is controlled with a precipitated inclusion phase during post-deformation heat treatments (recrystallization), the inclusion phase used to control grain growth in ceramics must be introduced prior to sintering, either as a second phase powder or by sintering in a two-phase field. Studies of alumina, in which zirconia inclusions were introduced as a second phase powder, showed that abnormal grain growth could be controlled if the inclusions were uniformly dispersed to fill most four-grain junctions. This requires an inclusion volume fraction greater than a critical value. Materials with inclusion volume fractions less than the critical value experienced more abnormal grain growth than the material without inclusions. It was shown that the critical volume fraction is dependent on the ratio of the sizes of the inclusions and the major phase particulates and the homogeneity of the two-phase powder mixture.



SC5295.4FR

Investigations during the third year concentrated on refining the method of eliminating voids caused by organic inclusions, developing a technique for defining the phase distribution in polyphase ceramics, and investigating the effect of milling contaminants on the fabrication, microstructure and properties of transformation toughened zirconia ceramics. The organic-burn-out/iso-pressing method was studied by introducing polystyrene spheres of various sizes and examining the effect of closure pressure on the morphology of void closure. Shrinkage of the powder-compact/organic-inclusion composite during drying resulted in the formation of microcracks around the larger organic inclusions ($>50 \mu\text{m}$ for the case studied), consistent with the thermodynamics of microcracking due to residual stresses around inclusions. It was found that the heat treatment required to produce organic burn-out also produced sufficient interparticle bonding that a critical pressure had to be exceeded to induce pore closure. Once the critical pressure was exceeded, pore closure proceeded by the 'deformation' of agglomerates, which continued to fill the void as the pressure was increased. A method of defining the phase distribution of polyphase systems, using energy dispersive x-ray analysis (EDAX), was investigated. It was demonstrated that variations in the EDAX spectra obtained as a function of magnification could be used to define the smallest area (or volume) element which contained the same phase distribution as the whole specimen. These results strongly suggest that the EDAX/Scanning Electron Microscope Method could be used as a quality assurance tool throughout the processing and fabrication of multiphase materials.

The effects of attrition milling on the fabrication, phase relations, microstructure and properties of ZrO_2 , a transformation toughened material, were examined. As expected, milling introduced contaminants, viz alumina particles and a glassy phase (the alumina milling media contains a silicious glass). The glass phase advantageously reduced the residual stresses produced at low temperatures by thermal expansion anisotropy, but detrimentally allowed more deformation at higher temperatures. The alumina inclusions introduced during milling not only produced an unwanted flaw population, but also formed a solid-solution with the zirconia and changed the phase relations in the



SC5295.4FR

ZrO₂-Y₂O₃ system. Post-sintering heat treatment caused formation of large pores because of the release of high pressure oxygen during the decomposition of the tetragonal phase (the toughening agent in these materials) to the cubic phase. These pores were larger and more pronounced for milled material containing the glass phase. These results not only produced new insight into the fabrication of transformation toughened ceramics based on the ZrO₂-Y₂O₃ system and requirements for retaining the tetragonal toughening agent, but also emphasized the attributes of colloidal processing relative to the conventional methods of powder preparation (attrition milling).

During this final year, effort was concentrated on: 1) surface stresses that are induced during diamond grinding and their effect on limiting the extension of surface flaws; 2) grain growth phenomena as influenced by inclusion phases, stresses applied during fabrication, and the retention of the tetragonal phase in transformation toughened ZrO₂(+Y₂O₃) ceramics; and 3) the fracture behavior of transformation toughened materials based on precipitated microstructures. Dr. David Marshall, who became a co-investigator on this program, was responsible for Tasks 1 and 3, and Dr. Fred Lange was responsible for Task 2. Prof. Rishi Raj (Cornell University) contributed to the effect of stress on grain growth behavior. Margaret Hirlinger, a M.I.T. undergraduate student, also contributed her technical expertise during summer employment. The following paragraphs briefly outline the major results in these areas. Details are reported in appendices.

The study of surface stresses (Appendix I) evolved from previous work in which we found that residual compression induced by diamond grinding of ceramics could dramatically improve the damage tolerance of the surface (strength improvements by up to a factor of 2 were observed - Ref. 4 of Appendix I). The present study was aimed at characterizing the compressive layer and determining the factors that control the magnitude of the stress. Stresses as high as ~ 500 MPa over depths of ~ 20 μm, were observed. For given grinding conditions, the stress increased with the hardness of the material. More than an order of magnitude variation was found between



materials covering most of the range of hardnesses in ceramics. The stress in a given material was insensitive to the material removal rate during grinding for a given grinding medium, but very sensitive to changes in grinding medium. For example, dressing of a diamond wheel (which caused the particles to protrude further from the surface of the wheel) yielded a factor of two increase in stress. Significant surface stresses were also induced by diamond polishing. The results of this study suggest that grinding conditions can be tailored to optimize the beneficial influence of the compressive layer.

As detailed in Appendix II, the effect of inclusions with average size ($0.6 \mu\text{m}$) larger than that of the major phase powder ($< 0.1 \mu\text{m}$) on grain growth was examined. This was done by sintering $\text{ZrO}_2/\text{Al}_2\text{O}_3$ composites (0, 3, 5, 10, and 20 volume % of Al_2O_3) at 1400°C and then heat treating at temperatures up to 1700°C . Normal grain growth was observed for all conditions. The Al_2O_3 inclusions appeared to have no effect on grain growth until the ZrO_2 grain size was 1.5 times the average inclusion size. Grain growth inhibition then increased with volume fraction of the Al_2O_3 inclusion phase. At temperature $< 1600^\circ\text{C}$, the inclusions were relatively immobile and most were located within the ZrO_2 grains for volume fractions < 0.20 ; at higher temperatures the inclusions could move with the grain boundary to coalesce eventually at 4-grain junctions. Grain growth was less inhibited when the inclusions could move with the boundaries, resulting in a larger increase in grain size than observed at lower temperatures. Analogies are made between observation of mobile voids, entrapped within grains at a lower temperature owing to abnormal grain growth during the last stage of sintering, and the observations concerning the mobile inclusions. These analogies suggest that grain boundary movement can 'sweep' voids to grain boundaries and eventually to 4-grain junctions, where they are more likely to disappear by mass transport. The results of this investigation show that immobile inclusions are far more effective at limiting grain growth than mobile inclusions that migrate to four-grain junctions. The size of the inclusion phase introduced into the major phase powder should also be much smaller than the size of the major phase powder.



SC5295.4FR

As detailed in Appendix III, control of grain size can also be achieved by sintering in a two-phase field. This was demonstrated by experiments in the ZrO_2 - Y_2O_3 system. The average grain size of ZrO_2 ($+Y_2O_3$) materials sintered at $1400^\circ C$ was observed to depend significantly on Y_2O_3 contents between 0.8 to 1.4 m/o and increased with Y_2O_3 content. The average grain size decreased by a factor of 4 to 5 for Y_2O_3 contents between 0.8 to 1.4 m/o and increased at Y_2O_3 contents of 6.6 m/o. Grain growth control by a second phase is the concept used to interpret these data. Namely, the compositions that yielded small grain sizes lie within the two-phase, tetragonal + cubic phase field, and the size of the tetragonal grains is controlled by the cubic grains. This interpretation suggests that the Y_2O_3 -rich boundary of the two-phase field lies between 0.8 and 1.4 m/o Y_2O_3 and that transformation toughened materials fabricated in this binary system must have a composition that lies within the two-phase field to obtain the small grain size which is required, in part, to retain the tetragonal toughening agent.

As detailed in Appendix IV, the morphology of grains (elongated or equiaxed) produced during deformation depends on the kinetics of two competing processes, viz, elongation by plastic deformation (e.g., dislocation motion) vs diffusional restoration of the equiaxed grain shape by preferred grain boundary motion in an attempt to impose equilibrium dihedral angles at grain junctions. Theory is presented to estimate the temperature ranges where the elongated grain structure will dominate and those where equiaxed microstructures will be produced during stressing.

The study of strength-limiting characteristics of precipitated transformation toughened materials (Appendix V) was initiated to enable optimum microstructures to be defined. The work has revealed that relations between strength, load bearing capacity, defects, and toughness, differ considerably in these materials and in nontoughened ceramics. In situ observations indicated that both reversible and irreversible transformation, as well as extensive microcracking, precede failure, and that eventual failure occurs after stable growth of a microcrack to a critical configuration. Measurements of



tensile stress-strain curves confirmed the existence of extensive nonlinear deformation prior to failure. These observations have important implications for the design and evaluation of optimum microstructures: 1) the stable crack growth indicates that strength is controlled by a crack growth resistance curve (similar to many metals) rather than by pre-existing defects and conventional fracture toughness (the insensitivity of strength to defects was confirmed by measurements of the strengths of surfaces containing artificially induced flaws); 2) the observation of reversible transformation indicates that the transformation is stress-induced rather than strain-induced and sheds new light on interpretations of the critical conditions for transformation; and 3) the nonlinear stress-strain response allows redistribution of stresses in certain loading configurations, resulting, for example, in higher apparent strengths in flexure than in tension.



LIST OF PUBLICATIONS RESULTING FROM THIS AFOSR PROGRAM

1. F.F. Lange, "Processing Related Fracture Origins: Part 1, Observations in Sintered and HIP Treated Al_2ZrO_2 ," J. Am. Ceram. Soc. 66, 396 (1983).
2. F.F. Lange and M. Metcalf, "Processing Related Fracture Origins: Part 2, Agglomerate Motion and Crack-Like Internal Surface Produced by Differential Sintering," J. Am. Ceram. Soc. 66, 398 (1983).
3. F.F. Lange, I.A. Aksay, and B.I. Davis, "Processing Related Fracture Origins: Part 3, Differential Sintering of ZrO_2 Agglomerates in $\text{Al}_2\text{O}_3/\text{ZrO}_2$ Composites," J. Am. Ceram. Soc. 66, 407 (1983).
4. F.F. Lange, "Formation of Crack-Like Voids and Agglomerate Motion Due to Differential Sintering," 5th CIMTEC.
5. B. Kellelt and F.F. Lange, "Stresses Induced by Differential Sintering in Powder Compacts," J. Am. Ceram. Soc. (in press, May 1984).
6. F.F. Lange and N. Claussen, "Some Processing Requirements for Transformation Toughened Ceramics," Proc. Conf. on Ceramic Ultrastructures, University of Florida, Gainesville, Feb. 1983 (AFOSR-sponsored).
7. F.F. Lange and M. Hirlinger, "Hindrance of Grain Growth in Al_2O_3 by ZrO_2 Inclusions," J. Am. Ceram. Soc. 67, 164 (1984).
8. F.F. Lange, "Structural Ceramics: A Question of Fabrication," ASM Conf. on Materials for Future Energy Systems, J. Mat. for Energy Systems 6, 107 (1984).



9. F.F. Lange, B.I. Davis, and E. Wright, "Processing Related Fracture Origins IV: Eliminating Voids Produced by Organic Inclusions," J. Am. Ceram. Soc., in press.
10. F.F. Lange and M.M. Hirlinger, "Phase Distribution Studies using Energy Dispersive X-Ray Spectra Analysis," J. Am. Ceram., in press.
11. F.F. Lange, H. Shubert, N. Claussen, and M. Ruhle, "Effects of Attrition Milling and Post-Sintering Heat Treatment on Fabrication, Microstructure and Properties of Transformation Toughened ZrO_2 ," J. Mat. Sci., in press.
12. F.F. Lange and M.M. Hirlinger, "Grain Growth Phenomena in Two-Phase Ceramics: Al_2O_3 Inclusions in ZrO_2 ," sent to J. Am. Ceram. Soc.
13. F.F. Lange, "Transformation Toughened ZrO_2 : Correlations between Grain Growth Control and Composition in the ZrO_2 - Y_2O_3 System," sent to J. Am. Ceram. Soc.
14. R. Raj and F.F. Lange, "On the Retention of Equiaxed Grain Structure after Superplastic and Other Forms of High Temperature Deformation," Acta. Met. (in press).
15. D. Johnson-Walls, A.G. Evans, and D.B. Marshall, "Residual Stresses in Machined Ceramic Surfaces," J. Am. Ceram. Soc., to be published.
16. D.B. Marshall, "The Strength of Transformation Toughened Ceramics," J. Am. Ceram. Soc., to be published.
17. D.B. Marshall and M.R. James, "Reversible Martensitic Transformation in ZrO_2 ," J. Amer. Ceram. Soc., to be published.



PERSONNEL INVOLVED IN PROGRAM

F.F. Lange
D.B. Marshall
M. Hirlinger
R. Raj
M. James
D. Johnson-Walls
A.G. Evans



Rockwell International
Science Center

SC5295.4FR

APPENDIX I



Rockwell International
Science Center

SC5295.4FR

RESIDUAL STRESSES IN MACHINED CERAMIC SURFACES

D. Johnson-Walls and A.G. Evans

Department of Materials Science & Mineral Engineering
University of California
Berkeley, CA 94720

and

D.B. Marshall and M.R. James

Rockwell International Science Center
1049 Camino Dos Rios
Thousand Oaks, CA 91360

ABSTRACT

A study has been made of residual surface stresses generated by diamond grinding in ceramic materials. The stresses are characterized by both x-ray measurements of stress magnitudes and by line forces (product of stress and layer thickness) obtained from the bending of plates that were machined on one side. The line forces increase with the hardness of the material and are strongly dependent on grinding media, but are insensitive to the rate of material removal during grinding (over a limited range of variation). Residual stress measurements are compared with measurements of strengths of the ground surfaces.



I. INTRODUCTION

Damage is introduced into brittle materials by surface finishing procedures that remove material mechanically, e.g., grinding and polishing.¹⁻¹⁰ This damage leaves residual stresses, both compressive and tensile, which can have a major influence on the mechanical properties and integrity of the surface.^{4,5}

The existence of residual compression in abraded glass was demonstrated as early as 1922 by measurements of bending forces in strips that were abraded on one face.¹ In a later study,² residual compressive stresses surrounding microabrasions in diamond were measured using x-ray topography. More recently, shallow layers of residual compression have been detected in machined (i.e., surface-ground) surfaces using several methods: a photoelastic technique in MgO;³ indentation testing in a glass ceramic⁴ and Si₃N₄;⁵ an x-ray diffraction technique in Al₂O₃;⁶ and measurement of the bending of thin plates of Si₃N₄ machined on one surface.⁷ The formation of these residual stresses does not seem to be limited to severely damaged surfaces; even in a very finely polished surface of Al₂O₃ (0.25 μm diamond polishing), residual compression was found to cause severe buckling of thin foils prepared for transmission electron microscopy.⁸

The most recent machining studies have shown that, in addition to the compressive layer, an underlying residual tension exists at the site of the strength-controlling damage.^{5,7,9,10} This tension has an important bearing on strength properties. The influence of the tension was detected using acoustic wave scattering to monitor the response of strength-controlling cracks in Si₃N₄ during failure testing,⁵ and by measuring strength/crack size relations in several materials.^{9,10}

The origin of residual stresses can be understood by regarding the machining damage as an accumulation of a large number of isolated sharp particle contact events. In the early abrasion studies, residual stresses were thought to arise from debris at fracture interfaces preventing perfect healing



SC5295.4FR

of the cracks formed by the abrasion. However, the observation that localized contacts in machining and abrasion cause irreversible deformation,⁸ as well as fracture, has led to an alternative interpretation. It is now well established that an isolated elastic/plastic contact gives rise to a radially compressive residual field, with tangential tension outside the plastic zone which surrounds the contact site.^{11,12} Strength-degrading cracks form on median planes within the tensile field,^{11,12} whereas the overlap of residual fields from neighboring damage sites in a machined surface gives rise to a layer of residual compression. This compression tends to reduce, but does not eliminate, the residual tension acting on the strength-controlling flaw.^{5,7,9,10}

The competing influences of the layer of compression and the localized tension at the strength-controlling flaw present a possibility to modify machining treatments to improve mechanical properties. Clearly, any enhancement of the compressive layer relative to the localized tension would increase the strength. A closely related strengthening mechanism has already been demonstrated on ZrO_2 -containing materials, where additional compression arises from a volume-increasing phase transformation which occurs in the machined surface.¹³⁻¹⁵ An additional benefit of the compressive layer is an improved resistance to in-service strength degradation by mechanical contact, as demonstrated by the indentation studies cited above.^{4,5} With these effects in mind, the objective of the present study is to measure the residual compression in a wide range of ceramic materials, and to make a preliminary investigation of the effect of varying machining conditions on the compressive layer and on the strength of the machined surface.

II. EXPERIMENTAL PROCEDURE

Two techniques were used to evaluate the residual compressive surface layers in machined surfaces. One technique involved measurement of the elastic bending caused by the residual stress in thin plates, and the other was an x-ray diffraction technique in which the change in lattice spacing resulting



SC5295.4FR

from the residual stress was measured. The x-ray method has been used previously to measure surface stresses in Al_2O_3 .⁶ In the present experiments, Cr radiation was used, with penetration depths $< 5 \mu m$ for 50% of the x-rays and $< 19 \mu m$ for 90%.

The plate-bending measurements required preparation of a thin plate with one surface polished and the other machined. This was done by first preparing a flat polished surface on one side of a thick plate, then bonding the polished surface to a rigid support base and reducing the thickness of the plate by machining from the opposite side. When the plate was removed from the support base, the compression in the machined surface caused the plate to bend such that the polished surface became concave (Fig. 1(A)). Measurement of the radius of curvature, ρ , by an optical interference method then allowed the product of the average compression, σ_R , and the thickness, t , of the compressive layer to be evaluated from the relation,¹⁶

$$\sigma_R t = Ed^2/6 \rho(1-\nu) \quad , \quad (1)$$

where d is the thickness of the plate ($d \ll t$), E is Young's modulus, and ν is Poisson's ratio.

The line force, $\sigma_R t$, was measured using this method at fixed grinding conditions* for the materials listed in Table I. Then, the variation of $\sigma_R t$ with depth-of-cut (all other grinding parameters remaining constant) was measured in two of the materials, Si_3N_4 and glass, and a preliminary investigation on the effect of grinding particle size on $\sigma_R t$ was made from measurements before and after dressing of the grinding wheel. In all these measurements, the plate dimensions were approximately $20 \times 6 \times 0.4$ mm, giving curvatures within the range 1 to 10 m.

* 240 grit diamond grinding wheel, 8 in. diameter, 3300 rpm, $2 \text{ cm} \cdot \text{s}^{-1}$ horizontal speed, $2 \mu m$ depth-of-cut.



SC5295.4FR

The corresponding variation in strength with depth-of-cut was measured in Si_3N_4 and glass. The strengths were measured by four-point bending of 10 bars for each combination of material and depth-of-cut, with loading spans of 6 and 40 mm for Si_3N_4 (cross section of bars, 3 x 5 mm) and 6 and 70 mm for glass (cross sections 5 x 10 mm). The glass strength measurements were done in an oil environment at a loading rate of $10 \text{ MPa}\cdot\text{s}^{-1}$ to suppress effects of moisture-assisted slow crack growth during the failure tests.

The residual stress layer was investigated in more detail in one material, Si_3N_4 . This was done using both bending measurements and x-ray measurements to monitor changes in the compressive layer as a function of surface removal. The machined surface of a plate prepared as described above was removed in 5-10 μm increments using diamond polishing media, with the plate bonded under pressure to a rigid flat base to remove the the residual bending. X-ray measurements were made after each polishing increment, before removing the plate from the base for the residual bending measurement. The initially flat polished surface of this plate was prepared (before preparing the machined side) using 0.25 μm diamond.

III. RESULTS

An optical interference micrograph of a thin plate of Si_3N_4 prepared in the manner described above is shown in Fig. 1(B). A similar observation prior to the machining step established that any initial curvature of the polished surface was negligible. Thus, the elliptical shape of the interference rings in Fig. 1(B) indicates that machining stresses are not equibiaxial; the compression is maximum (i.e., radius of curvature minimum) normal to the machining direction. Similar results were obtained for the other materials in Table I, with the exception of ZnS, in which the compression was maximum parallel to the machining direction.

The residual bending forces at fixed grinding conditions, in the materials listed in Table I, are shown in Fig. 2. These forces were calcu-



SC5295.4FR

lated from Eq. (1), with the radius of curvature determined from interference micrographs such as Fig. 1(B). A strong increase in the residual force with material hardness is evident. A previous measurement (using the x-ray method⁵) for machining damage in Al_2O_3 is consistent with these data. In addition, line forces previously determined for abraded glass¹ ($\sigma_{RT} = 100$ to $1000 \text{ N}\cdot\text{m}^{-1}$) and diamond² ($\sigma_{RT} = 100$ to $500 \text{ N}\cdot\text{m}^{-1}$) lie within the range of the measurements in Fig. 2. It is noted that one material, the transformation-toughened ZrO_2 exhibits a larger bending force than the trend for the other materials would suggest. This result is consistent with observations¹³⁻¹⁵ of a volume-increasing martensitic transformation (tetragonal to monoclinic) induced by grinding in this material. The transformation contributes additional compressive residual stress.

The effects of varying the depth-of-cut while keeping all other grinding parameters constant are shown in Figs. 3 and 4. The residual force was not significantly affected, at least within the range of conditions examined (Fig. 3). The strengths of the machined surfaces decreased with increasing depth-of-cut (Fig. 4), but the decreases were small.

Results of x-ray and bending measurements obtained after removing layers of the machined surface by polishing are shown in Figs. 5 and 6. The degree of residual bending decreases rapidly for the first $10 \mu\text{m}$ of material removal and approaches a level that appears to be characteristic of the polishing procedure. The stress magnitude obtained from x-ray measurements decreases similarly for the first $10 \mu\text{m}$, but thereafter a stress due to $3 \mu\text{m}$ polishing is not detected.



SC5295.4FR

The machined surfaces used for the data in Figs. 2-5 were prepared with a grinding wheel that had been used extensively without being dressed.* Silicon nitride reference specimens were included throughout the experiments to ensure that changes in the condition of the wheel did not influence the results. After completing the experiments, the wheel was dressed and measurements on Si_3N_4 and ferrite were repeated. These measurements yielded values of σ_{Rt} in the transverse and longitudinal directions of 9.9 and 7.6 $\text{GPa}\cdot\mu\text{m}$ for Si_3N_4 , and 2.1 and 1.9 $\text{GPa}\cdot\mu\text{m}$ for ferrite. These values are about a factor of two higher than the corresponding data in Fig. 2.

IV. DISCUSSION AND CONCLUSIONS

Results of the sequential surface removal and line-force measurements suggest that the depth of the compressive layer associated with the machined surface is about $10\ \mu\text{m}$. This depth, combined with the measurement $\sigma_{Rt} = 3.5\ \text{GPa}\cdot\mu\text{m}$ for the as-machined surface (parallel to the machining direction) gives $\sigma_R = 350\ \text{MPa}$. The bending measurements also imply that polishing with 15 and $3\ \mu\text{m}$ diamond media produces residual line forces of 2.2 and $1.5\ \text{GPa}\cdot\mu\text{m}$, respectively. The observation of significant residual stress layers in mechanically polished surfaces of Si_3N_4 is in accord with the previously mentioned observations by Hockey⁸ on polished Al_2O_3 .

The x-ray measurements (Fig. 6) imply a similar depth of compressive stress, but the stress magnitudes for both the machined and polished surfaces are lower than those calculated from the bending measurements. This apparent

* One exception is the measurement for the transformation-toughened ZrO_2 in Fig. 2. This measurement was made after the wheel was dressed, yielding $\sigma_{Rt} = 12.8\ \text{GPa}\cdot\mu\text{m}$ (transverse) and $\sigma_{Rl} = 8.9\ \text{GPa}\cdot\mu\text{m}$ (longitudinal). To enable comparison with the data in Fig. 2, these values were reduced by a factor of 2 for plotting, corresponding to the measured differences before and after dressing for Si_3N_4 and ferrite.



SC5295.4FR

discrepancy most likely arises because the penetration depth of the x-rays (19 μm for 90%) exceeds the depths of the compressive layers.

The residual force, σ_{RT} , clearly increases with the hardness of the material. Other parameters which, on the basis of preliminary analysis,¹⁸ are expected to influence the material removal process are the fracture toughness and elastic modulus. However, the data in Fig. 2 are not sufficiently extensive to discern any significant trends of the residual forces with these parameters.

The insensitivity of the residual force and strength to the depth-of-cut has the obvious practical implication that machining can be conducted at relatively large cut depths (at least on the materials and under the grinding conditions investigated here). However, it is interesting to note that the constancy of the residual force and strength suggest that the force on an individual diamond within the wheel during grinding is essentially independent of the depth-of-cut, whereas the total force on the grinding wheel is generally observed to increase with the depth-of-cut.¹⁶ Presumably, therefore, the number of diamonds involved in machining increases with the cut depth. Details of this effect require additional investigation.

The distinction between the local and total forces involved in the grinding process is further illustrated by comparison with single-point scratching experiments.^{16,17} An increase in depth-of-cut from 2 to 10 μm for Si_3N_4 increases the grinding force by a factor of three,¹ but decreases the strength by only 5% (Fig. 4). A corresponding increase in normal load in scratching experiments degrades the strength by 30%, thus reaffirming that the force on individual diamonds cannot increase as rapidly as the total grinding force.

The increase in residual force observed after dressing the grinding wheel suggests that the residual compressive layer is very sensitive to the size of the grinding particles (since dressing the wheel causes grinding particles to protrude further from the surface of the wheel). The result also implies that the maximum force on individual diamonds during grinding is



SC5295.4FR

limited by the extent that they protrude from the wheel surface, consistent with the above hypothesis that the forces on individual diamonds do not increase with increasing depth-of-cut.

The nonequibiaxial nature of the residual stress, having a maximum compression normal to the machining direction, is consistent with notions of residual stress development due to the elastic accommodation of the volume of the grinding grooves.¹⁰ However, the relative uniformity of the residual compression evident in the ZnS remains to be explained.



REFERENCES

1. A.J. Dalladay, "Some Measurements of the Stresses Produced at the Surfaces of Glass by Grinding with Loose Abrasives," *Trans. Opt. Soc. Lond.* 23, 170 (1922).
2. F.C. Frank, B.R. Lawn and A.R. Lang, "A Study of Strains in Abraded Diamond Surfaces," *Proc. Roy. Soc. Lond.* A301, 239-52 (1967).
3. E. Bernal and B.G. Koepke, "Residual Stresses in Machined MgO Crystals," *J. Am. Ceram. Soc.* 56 [12], 634-39 (1973).
4. R.F. Cook, B.R. Lawn, T.P. Dabbs and P. Chantikul, "Effect of Machining Damage on the Strength of a Glass Ceramic," *J. Am. Ceram. Soc.* 64 [9], c121-122 (1981).
5. D.B. Marshall, A.G. Evans, B.T. Khuri-Yakub, J.W. Tien and G.S. Kino, "The Nature of Machining Damage in Brittle Materials," *Proc. Roy. Soc. Lond.* A385, 461-475 (1983).
6. F.F. Lange, M.R. James and D.J. Green, "Determination of Residual Surface Stresses Caused by Grinding in Polycrystalline Al_2O_3 ," *J. Am. Ceram. Soc.* 66 [2], c16-17 (1983).
7. D.B. Marshall, "Failure from Contact-Induced Surface Flaws," *ASTM STP 844*, eds., S.W. Freiman and C.M. Hudson (1984).
8. B.J. Hockey, "Plastic Deformation of Aluminum Oxide by Indentation and Abrasion," *J. Am. Ceram. Soc.* 54 [5], 223-31 (1971).
9. H.P. Kirchner and E.D. Isaacson, in *Fracture Mechanics of Ceramics*, vol. 5, ed. by R.C. Bradt, A.G. Evans, D.P.H. Hasselman and F.F. Lange, Plenum Press, NY, 1983.



SC5295.4FR

10. H.P. Kirchner and E.D. Isaacson, "Residual Stresses in Hot-Pressed Si_3N_4 Grooved by Single-Point Grinding, J. Am. Ceram. Soc. 65 [1], 55-60 (1982).
11. D.B. Marshall and B.R. Lawn, "Residual Stress Effects in Sharp Contact Cracking," J. Mater. Sci. 14 [8], 2001-12 (1979).
12. B.R. Lawn, A.G. Evans and D.B. Marshall, "Elastic/Plastic Indentation Damage in Ceramics: The Median/Radial Crack System," J. Am. Ceram. Soc. 63 [9-10], 574-81 (1980).
13. R.T. Pascoe and R.C. Garvie, in Ceramic Microstructures 1976, ed. by R.M. Fulrath and J.A. Pask, Westview Press, Boulder, CO, 1977.
14. M.V. Swain, "Grinding-Induced Tempering of Ceramics Containing Metastable Tetragonal Zirconia," J. Mater. Sci. 15 [8], 1577-79 (1980).
15. T.K. Gupta, "Strengthening by Surface Damage in Metastable Zirconia," J. Am. Ceram. Soc. 63 [1-2], 117 (1980).
16. H.J. Oel and V.D. Frechett, "Stress Distribution in Multiphase Systems: I. Composites with Planar Interfaces," J. Am. Ceram. Soc. 50 [10], 542-49 (1967).
17. A.G. Evans and D.B. Marshall, Fundamentals of Friction and Wear (Ed., D.A. Rigney), ASM (1980), p. 439.
18. T. Uchiyama, D.B. Marshall and A.G. Evans, unpublished work.
19. D.B. Marshall, unpublished work.



SC85-31233

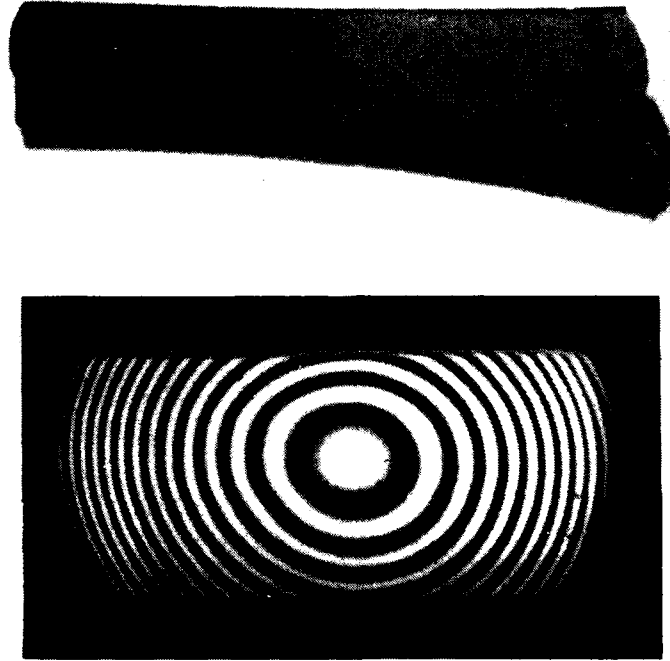


Fig. 1 (a) Thin plate of Si_3N_4 (thickness 0.1 mm) with upper surface polished (initially flat) and lower surface subsequently machined. (b) Optical interference photograph of polished surface of a plate similar to that in (a) (thickness 0.34 mm). Machining direction on lower surface is horizontal. Wavelength of illumination, 546 nm. Width of field, 10.7 mm.



SC5295.4FR

SC83-23993

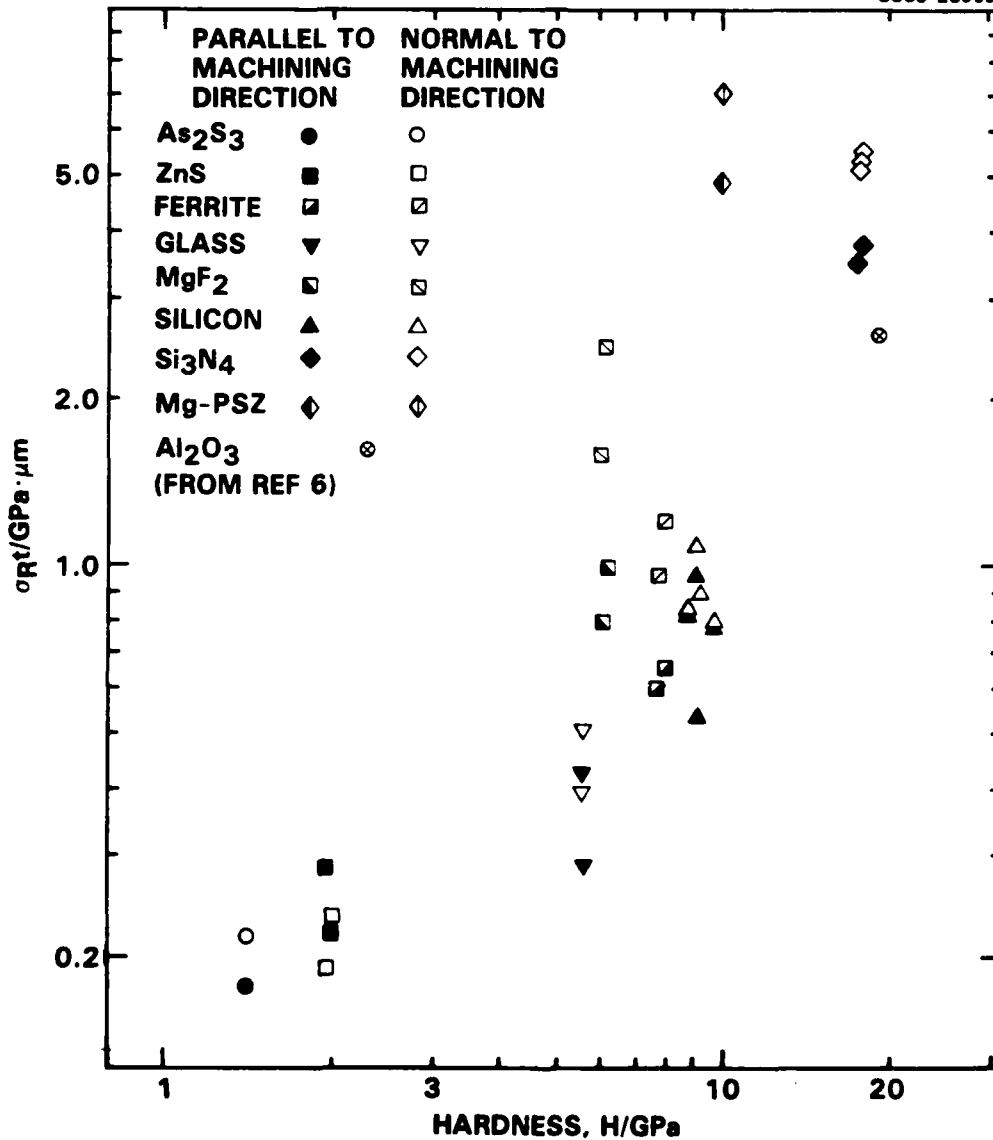


Fig. 2 Plot showing correlation between compressive forces in machined surfaces and hardness at fixed machining conditions. Data from several plates of each material are offset slightly along the hardness axis to allow distinction of the pairs of measurements from each plate parallel and normal to the machining direction.

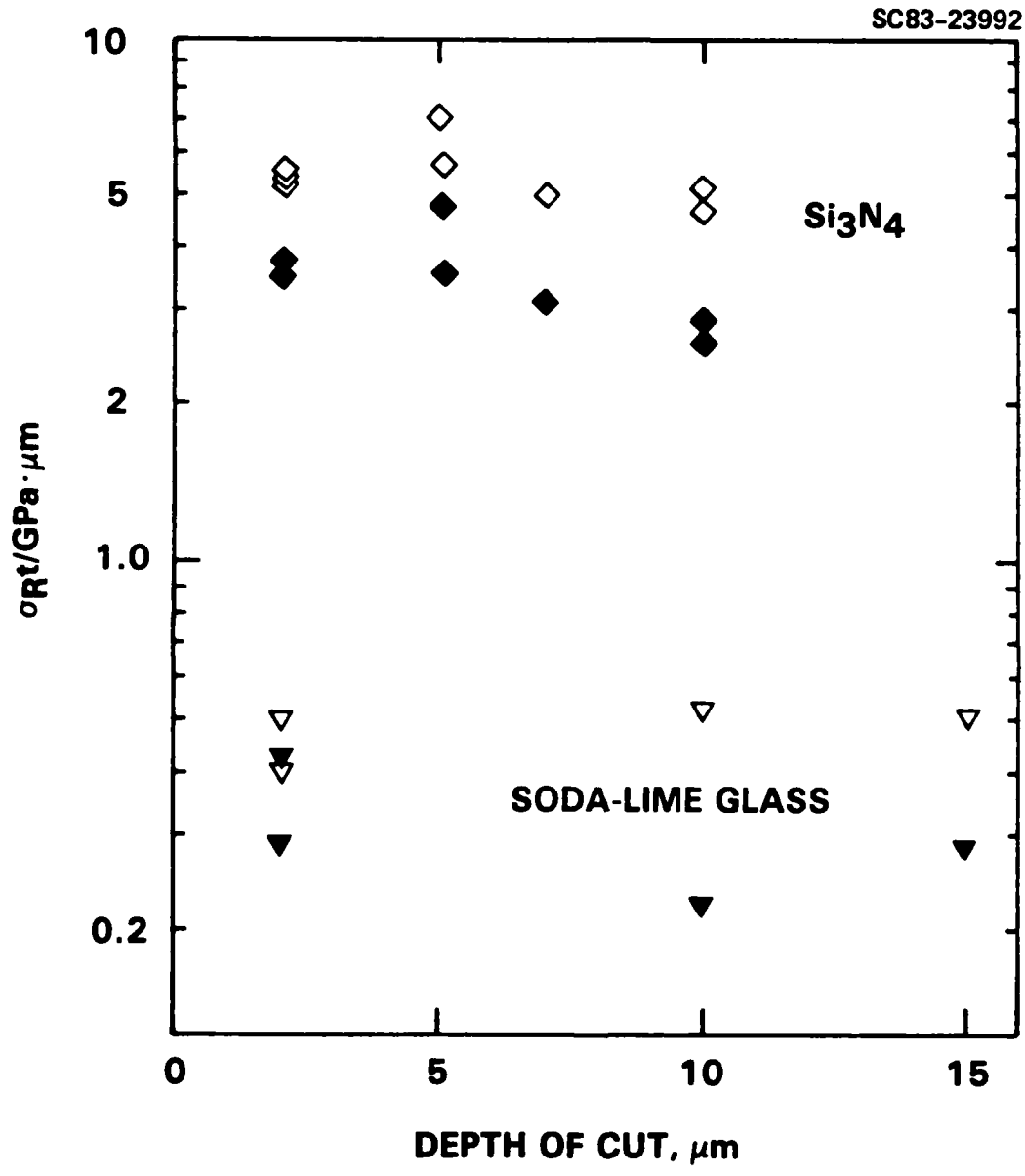


Fig. 3 Variation of compressive forces in machined surfaces of Si₃N₄ and glass with depth-of-cut during machining.

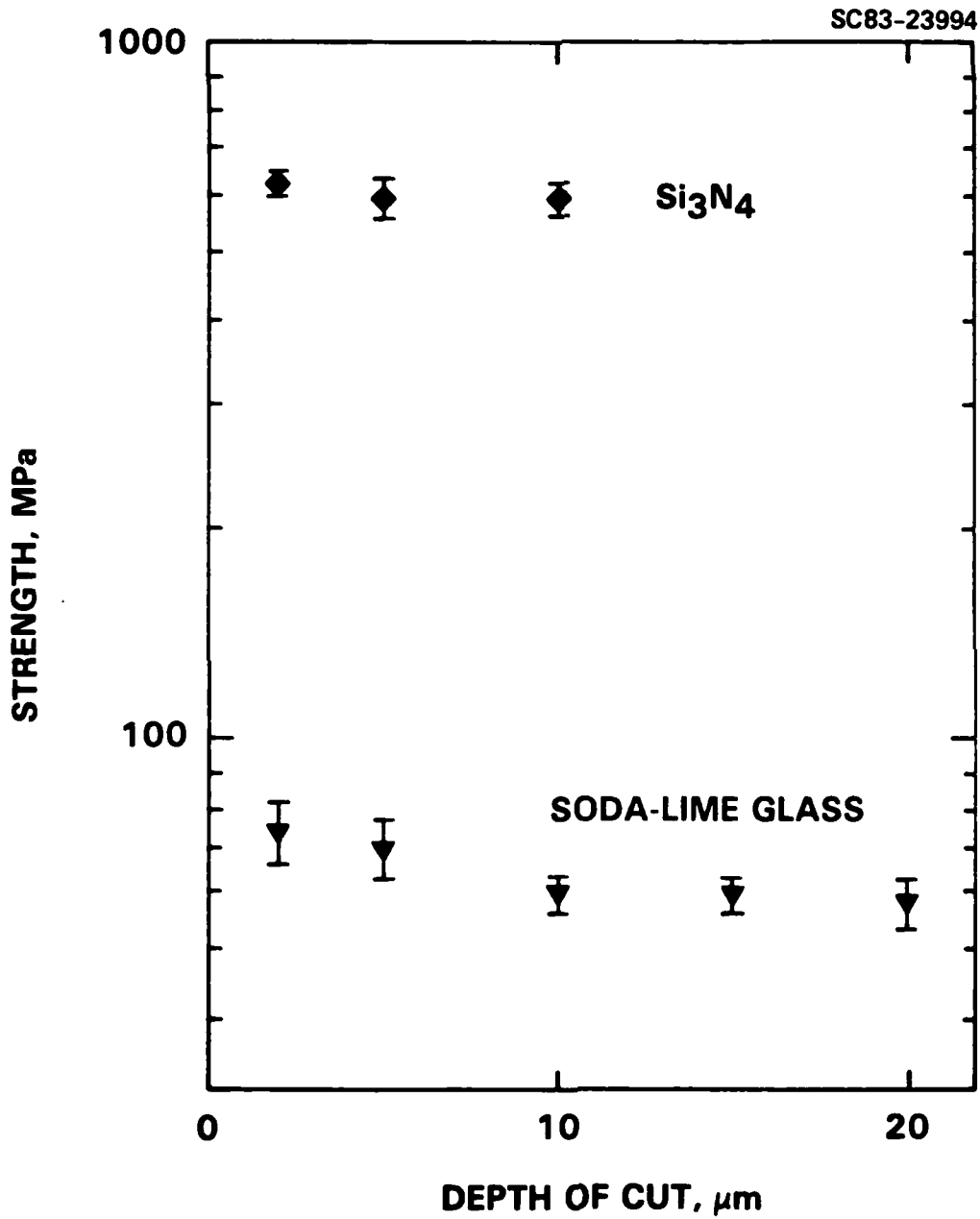


Fig. 4 Variation of strengths of machined surfaces of Si_3N_4 and glass with depth-of-cut during machining.

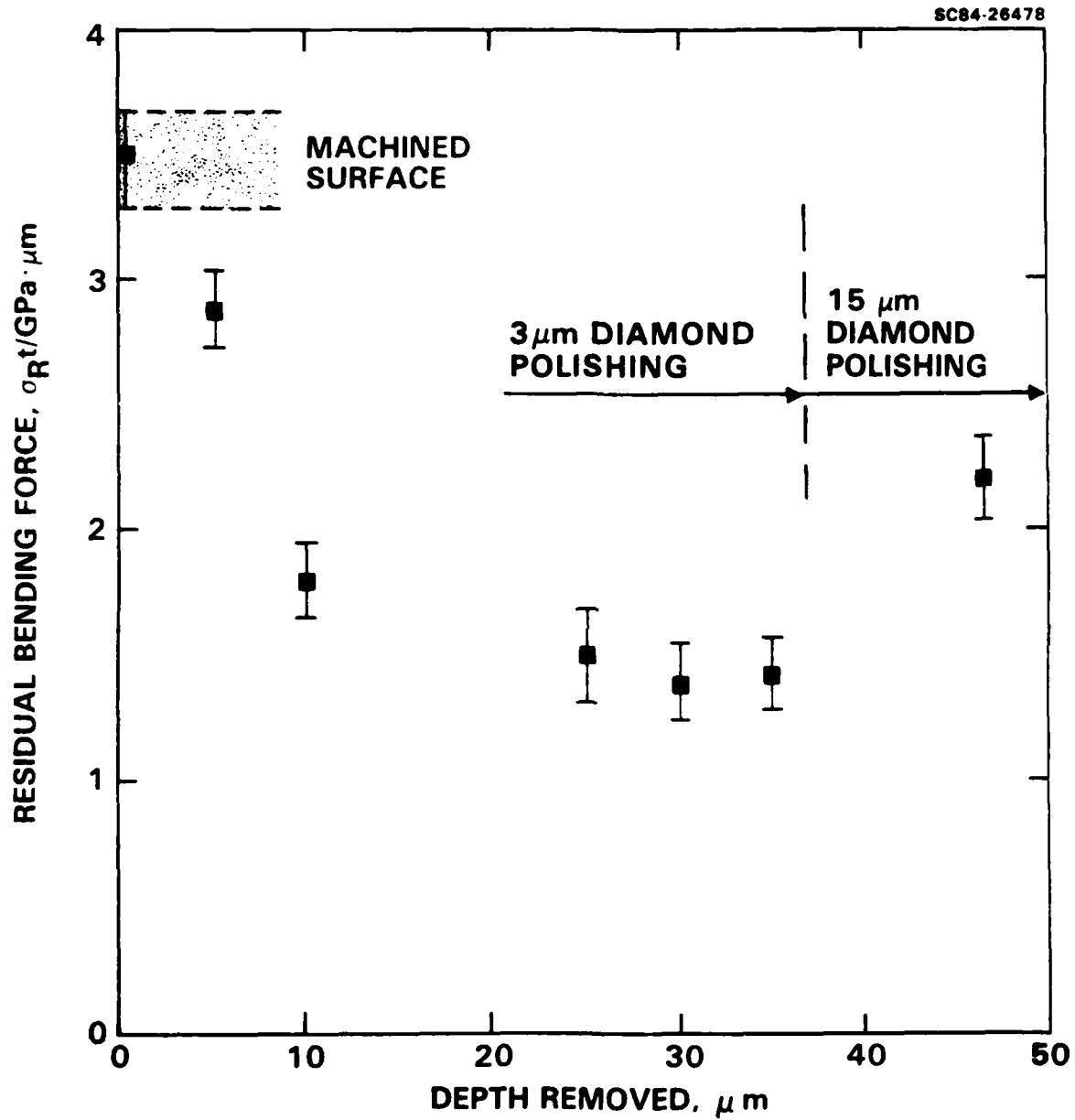


Fig. 5 Variation of residual bending force (parallel to the grinding direction) with removal of grinding damage by polishing with 3 and 15 μm diamond.

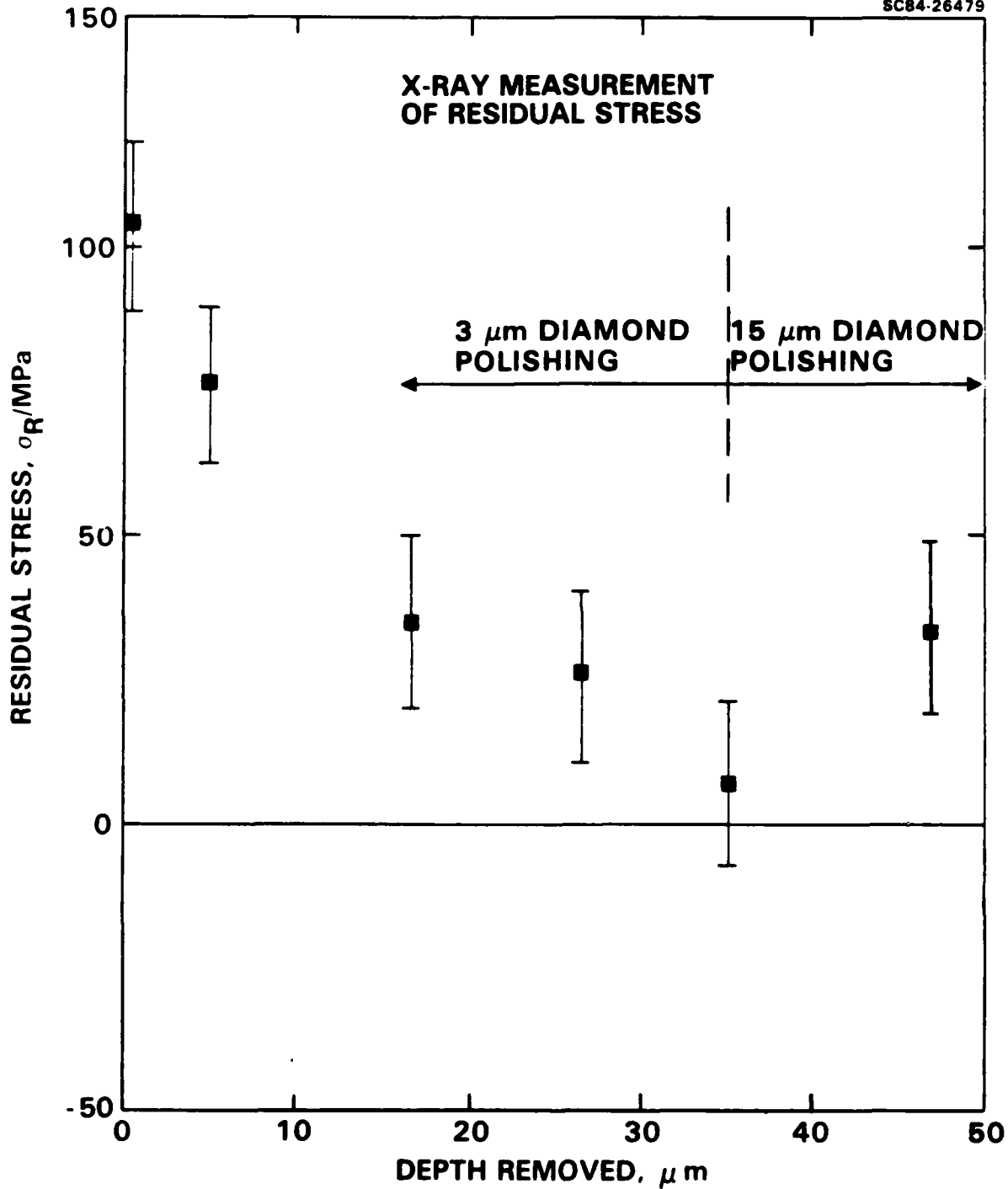


Fig. 6 X-ray stress measurements for the surface removal experiments in Fig. 5.



Table I
Materials Used for Residual Stress Measurement

Material	E (GPa)	H (GPa)	K_C (MPa·m ^{1/2})
As ₂ S ₃ ⁽¹⁾	16	1.4	0.23
ZnS ⁽²⁾	98	1.9	0.6
Ferrite ⁽³⁾	200	8.0	0.9
Soda-Lime Glass	70	5.5	0.75
MgF ₂ ⁽²⁾	120	6.0	0.6
Silicon ⁽⁴⁾	168	10.6	0.7
Si ₃ N ₄ ⁽⁵⁾	300	18.0	4.0
Mg-PSZ ⁽⁶⁾	200	10.0	13.0

1. Glass
2. Irtran, Eastman Kodac Co., Rochester, NY
3. Micronetics, W. Hurley, NY
4. Single crystal
5. NC-132 Norton Co., Worcester, MA
6. Magnesia partially stabilized zirconia, transformation-toughened, Nilcra, Australia.



APPENDIX II



GRAIN GROWTH PHENOMENA IN TWO-PHASE CERAMICS:
 Al_2O_3 INCLUSIONS IN ZrO_2

F.F. Lange and Margaret M. Hirlinger*

Structural Ceramics
Rockwell International Science Center
Thousand Oaks, CA 91360

ABSTRACT

The effect of inclusions with a greater average size ($0.6 \mu\text{m}$) than the average particles size of the major phase powder ($< 0.1 \mu\text{m}$) on grain growth was examined by sintering $\text{ZrO}_2/\text{Al}_2\text{O}_3$ composites (0, 3, 5, 10, and 20 volume % Al_2O_3) at 1400°C and then heat treating at temperatures up to 1700°C . Normal grain growth was observed for all conditions. The inclusions appeared to have no effect on grain growth until the ZrO_2 grain size was 1.5 times the average inclusion size. Grain growth inhibition increased with volume fraction of the Al_2O_3 inclusion phase. At temperatures $< 1600^\circ\text{C}$, the inclusions were relatively immobile and most were located within the ZrO_2 grains for volume fractions < 0.20 ; at higher temperatures, the inclusions could move with the grain boundary to coalesce eventually at four-grain junctions. Grain growth was less inhibited when the inclusions could move with the boundaries, resulting in a larger increase in grain size than observed at lower temperatures. Analogies between mobile voids, entrapped within grain at lower temperatures due to abnormal grain growth during the last stage of sintering, and the observations concerning the mobile inclusions are made suggesting that grain boundary movement can 'sweep' voids to grain boundaries and eventually, to four-grain junctions, where they are more likely to disappear by mass transport.



INTRODUCTION

Microstructural control is a critical issue facing fabricators of advanced cermics. Many advanced ceramics are polyphase materials with microstructures designed and fabricated using empirical notions discovered through trial and error. Second phases, historically introduced to aid sintering, have become increasingly important in controlling the average grain size and size distribution of the major phase. Abnormally large grains can be a critical, strength-degrading flaw populations in many ceramics. Abnormal grain growth can be prevented with the addition of the appropriate second phase to result in dramatic strengthening, as demonstrated with additions of SiC to Al_2O_3 ,¹ ZrO_2 (tetragonal or cubic) to $\beta''\text{-Al}_2\text{O}_3$ ² and Al_2O_3 to cubic ZrO_2 ³. Rhodes⁴ has demonstrated that abnormal grain growth can be prevented during the latter stages of sintering by choosing the appropriate binary system of interest that sinters in a two-phase compositional region. In this case, the second phase prevents the growth of abnormal grain that usually 'swallow' pores to limit their disappearance; annealing at lower temperatures in a single phase, solid-solution region can result in a single phase, transparent, polycrystalline material. More recently, Lange⁵ has shown that the exceptionally small grain size ($< 0.5 \mu\text{m}$) required to retain the tetragonal ZrO_2 phase in transformation toughened ceramics fabricated in the $\text{ZrO}_2\text{-Y}_2\text{O}_3$ system requires a composition selected in the two-phase (tetragonal + cubic) region of this binary system. Here, the cubic grains constrain the growth of the tetragonal grains required for toughening.

For ceramics, inclusions used to control grain size must be introduced either by mixing two-phase powders or by a partitioning reaction in a two-phase field during the densification process. Namely, the second phase must be effective prior to achieving relative densities > 0.90 , where rapid grain growth is commonly observed in single-phase materials.^{6,7} Experimental and theoretical issues of major importance, viz, effects of second-phase distribution (e.g., powder mixing), size distribution, volume fraction, inclusion location and mobility have not received much study primarily because con-



SC5295.4FR

trolled grain growth in metal systems (the source of most information) is approached by a method (precipitation, deformation, and recrystallization) which is not amenable to ceramics.

In a previous paper,⁸ the authors described the effect of ZrO_2 inclusions (volume fractions up to 0.10) on the grain growth behavior of Al_2O_3 . The inclusion phase was introduced as a powder and dispersed in the Al_2O_3 powder with a colloidal method prior to consolidation and sintering. The average size of the ZrO_2 inclusions was much smaller than the average size of the Al_2O_3 particles (the size ratio was <0.2). It was shown that the ZrO_2 inclusions would locate at four grain junctions during densification and would grow by coalescence to remain at these junctions under conditions of normal grain growth by the major phase Al_2O_3 grains. Abnormal growth of the Al_2O_3 grains was prevented by the ZrO_2 inclusions at volume fractions > 0.05 . For the condition of normal growth, the inclusion phase hindered growth of the major phase to result in a smaller, average grain size. For volume fractions less than 0.05, the inclusion phase promoted abnormal grain growth relative to the pure Al_2O_3 , due to its nonuniform distribution, i.e., Al_2O_3 grains unhindered by inclusions were nuclei for abnormal grain growth. Theoretical arguments based on the requirement for filling all four-grain junctions to uniformly inhibit the growth of all grains suggested that a critical volume fraction of inclusions was necessary to prevent abnormal grain growth. These conclusions were based on the premise that the inclusion particles in the initial powder are significantly smaller than the major phase particles.

Based on the observations outline above, experiments were designed to examine the grain growth phenomena for the case where the initial inclusion size was larger than the average size of the major phase particles. Based on the energetics of inclusion location first introduced by Zener,⁹ it was reasoned for this case that the major grains would grow unhindered until they were somewhat larger than the inclusions. Beyond this size, hindrance of grain growth was expected to be governed by the inclusion volume fraction and their mobility. To examine this case, the system studied before⁸ was simply



SC5295.4FR

turned around, viz the large Al_2O_3 particles became the inclusion phase in a much smaller size ZrO_2 powder matrix.

EXPERIMENTAL

Composite powders of cubic ZrO_2 (+ 6.6 mole % Y_2O_3)* and Al_2O_3 ** were prepared for consolidation using a colloidal method. As detailed elsewhere,⁸ the colloidal method involves separately dispersing each powder in water at pH = 2, sedimenting each dispersion to reject all particles or agglomerates > 1 μm , floccing (pH = 8) each dispersion to prevent mass segregation during storage, and then mixing appropriate amounts of the two flocced slurries with a high speed homogenizer¹⁰ which locally redisperses and mixes the two phases within its high shear rate field and then allows the two phases to co-floc as they leave the high shear rate field. This mixing procedure is analogous to the mixing of two nonreactive gases. The size distribution of the two dispersed powders were determined.***

Composite powder slurries containing 0, 3, 5, 10, and 20 v/o Al_2O_3 were prepared. The flocced slurries were slip casted to form discs which were dried and sintered at 1400°C for 2 h. The densities of all the sintered materials were > 96% of theoretical based on the densities of the two phases. Different specimens of each composite were heat treated at 1500°C, 1600°C, and 1700°C for 2 h, diamond cut to obtain an internal surface which was polished and thermally etched at either 1350°C (as-sintered and 1500°C specimens) or 1550°C to reveal grain boundaries.

Micrographs were taken with a scanning electron microscope which was operated in a combined secondary emission and backscatter mode to best reveal grain boundaries and to contrast the Al_2O_3 inclusions from the polycrystalline

* Zircar, Inc., Florida, NY.

** Sumotomo Chemical Co., Japan (AKP-30, $-\text{Al}_2\text{O}_3$).

*** Sedigraph 5000D, Micromeritics, Norcross, GA.



ZrO₂ matrix. The size distribution of the ZrO₂ grains was obtained by tracing the grain boundaries on the micrographs with black ink on a transparent overlay suitable for image analyzing. The image analyzer[†] was programmed to convert each grain area into an equivalent circle to obtain its equivalent diameter. These data were reduced to pertinent statistical parameters.

RESULTS

Figure 1 illustrates the size distribution of the two, colloiddally-treated powders. The distribution of the Al₂O₃ inclusion phase is narrow with a mean size of ~ 0.6 μm. The ZrO₂ powder had a wider distribution with a large fraction below the detectibility limit (< 0.1 μm) of the instrument.

Table 1 reports the pertinent ZrO₂ grain size data for each of the five materials heat treated at the four different temperatures. As reported, the ratio of the largest grain observed to the mean size (R) is < 3 for all materials and heat treatments. Theory developed by Kurtz and Carpay¹¹ shows that 'normal' grain growth (lack of abnormally large grains) is characterized by a lognormal grain size distribution, which requires that the largest grain in such a distribution be < 2.72 times the median size. Judging the values of R reported in Table 1 and the fact that a bimodal size distribution was never observed, it can be concluded that the materials examined undergo normal grain growth behavior.

Figure 2 illustrates the mean ZrO₂ grain size vs the heat treatment temperature for the five materials. This figure shows that volume fractions of the Al₂O₃ inclusion phase < 0.05 had no effect on the grain size of the as-sintered materials, but did effect grain growth to heat treatment temperatures up to 1600°C. Volume fractions > 0.10 dramatically inhibited grain growth to 1600°C. Between 1600°C and 1700°C, the inclusions are less effective in inhibiting grain growth than at lower temperatures, viz for volume fraction

† Cambridge Institute, England



SC5295.4FR

< 0.05 , the inclusion phase had no effect. As it will be shown in the next paragraphs, this change was coincidental with a redistribution of the Al_2O_3 phase.

Microstructural observations showed that the Al_1O_3 inclusions did not significantly change in size distribution relative to the initial powder at $1400^\circ C$ and $1500^\circ C$. The inclusions were well dispersed and the relatively few agglomerates that were observed were formed with a small number (< 4) of particles. These agglomerates could have been either present during powder mixing, or produced by coalesce during ZrO_2 grain growth. For volume fractions < 0.05 , a majority of the inclusions are observed within the ZrO_2 grains. The proportion of inclusions located at two- and three-grain junctions increased with volume fraction; a majority of inclusions were located at two-grain junctions in the material containing 0.20 v/o Al_2O_3 , as shown in Fig. 3.

Coarsing of the inclusions appeared to initiate during the $1600^\circ C$ heat treatment, as indicated by a small fraction of inclusions with larger sizes than observed in the initial Al_2O_3 powder. At $1700^\circ C$, the inclusion size distribution was bimodal for volume fractions > 0.10 . As shown in Fig. 4, both large single-grain inclusions and clusters of large inclusions were observed at three-grain junctions, whereas the smaller inclusions with size distribution of the initial powder are observed within the grains. Figure 4 also illustrates the common feature that portions of each grain are denuded of inclusions. This feature indicates that the small inclusions intersected by the moving grain boundary migrate with the boundary and are eventually 'swept' to the three- and four-grain junctions. For volume fractions < 0.05 , all of the smaller inclusions had been 'swept' to the three- and four-grain junctions at $1700^\circ C$.



DISCUSSION

As first suggested by Zener,⁹ an energy barrier must be overcome to remove an inclusion from a grain boundary to within a crystal. As detailed elsewhere,¹² similar barriers, but of lower magnitude, must be overcome to relocate an inclusion from a higher order grain junction to a lower order junction (viz, from a four-grain junction to a three-grain junction or a three- to two-grain junction). For this reason, inclusions will offer no hindrance to grain growth until they are somewhat smaller than the grains that are trying either to grow (or disappear) where they can be moved from either junction to junction or junction to interior. As shown in either Table 1 or Fig. 2, the smallest average grain size observed (as-sintered, 20 v/o inclusion material) was approximately 1.5 times the average inclusion size.

Zener also pointed out that the height of the energy barrier for boundary motion will be proportional to both the inclusion size and the number of the inclusions on the grain boundary. Thus increasing the volume fraction of inclusions will increase the hindrance to grain growth. This is certainly observed in the above data.

For the system studied here, the inclusions were relatively immobile at temperature $< 1600^{\circ}\text{C}$; grain boundaries, although somewhat impeded, could break away to locate most of the inclusions, for volume fractions < 0.20 , within the growing grains without significantly disturbing their initial spatial distribution. At higher temperatures, microstructural evidence showed that the inclusions obtained sufficient self-diffusion to migrate with the grain boundary which lead to their coalescence^{††} (see discussion in last paragraph concerning inclusion/void coalescence kinematics) at two-, three-, and eventually, four-grain junctions (their location of lowest free energy).

†† The observation of multiple, large inclusions at three-grain junctions strongly suggests that coalescence, and not Oswald-type diffusion was the cause of coarsening.



SC5295.4FR

One can easily show that coalescence, even at a grain boundary, will reduce the energy barrier for boundary break away. The area reduction of a grain boundary on which n identical, spherical inclusions reside $(1 - n^{-1/3})$ if these inclusions coalesce to form one larger sphere on the same grain boundary. The energy barrier for boundary break away will be reduced by a comparable amount. Thus, coalescence will reduce the effect of the inclusions on impeding grain growth, as indicated by the grain size data obtained at 1700°C .

We can now form an analogy between mobile inclusions and mobile voids, initially trapped within grains during the final stages of sintering due to abnormal grain growth. The major difference between the void and the inclusion is the void can disappear by diffusion, whereas, the inclusion cannot, otherwise the kinematics are identical. The analogy is straightforward. Voids trapped within grains at lower temperature during abnormal grain growth become more mobile at a higher temperature. Grain boundaries that move during the higher temperature regime will drag the voids with them. Voids collected at grain boundaries in this fashion can coalesce at three-grain junctions when a six-faced grain shrinks to a five-faced grain (see the topological parameters described by Kurtz and Carpay¹¹ in their discussion of the grain shrinkage that must accommodate grain growth); likewise the voids at the three-grain junction can coalesce at four-grain junctions when the five-faced grain shrinks to the four-faced grain. The voids at the four-grain will further coalesce when the four-faced grain disappears. During this process, the voids are placed on surfaces that are paths for fast diffusion. Also, and just as important, this process will more uniformly relocate the voids at four-grain junctions which will decrease the diffusion path length to one-half the distance to the next void to allow void disappearance with uniform shrinkage.

ACKNOWLEDGMENT

Support of this work by the Air Force Office of Scientific Research under Contract No F49620-81-C-0036 is greatly appreciated.



REFERENCES

1. F.F. Lange and Nils Claussen, "Some Processing Requirements for Transformation Toughened Ceramics," *Ultrastructure Processing of Ceramics, Glasses, and Composites*, ed. by L.L. Hench and D.R. Ulrich, pp. 493, John Wiley (1984).
2. D.J. Green, "Transformation Toughening and Grain Size Control in β - $\text{Al}_2\text{O}_3/\text{ZrO}_2$ Composites," *J. Mat. Sci.*, in press.
3. F.J. Esper, I.H. Friese, and H. Geier, "Mechanical, Thermal, and Electrical Properties in the System of Stabilized $\text{ZrO}_2(\text{Y}_2\text{O}_3)/\text{Al}_2\text{O}_3$," *Advances in Ceramics*, Vol. 12, Ed. by N. Claussen, M. Ruhle, and A.H. Heuer, pp. 528, Am. Ceram. Soc., Columbus, OH (1985).
4. W. Rhodes, "Controlled Transient Solid Second-Phase Sintering of Yttria," *J. Am. Ceram. Soc.* 64[1], 13 (1981).
5. F.F. Lange, "Transformation Toughened ZrO_2 Correlation Between Controlled Grain Growth and Composition in the $\text{ZrO}_2\text{-Y}_2\text{O}_3$ System," to be published.
6. T.K. Gupta, "Possible Correlations Between Density and Grain Size During Sintering," *J. Am. Ceram. Soc.* 55[5], 176b (1972).
7. F.F. Lange and B. Kellett, "Influence of Particle Arrangement on Sintering," 2nd Int. Conf. on Ultrastructure Processing of Ceramics, Glasses and Composites, ed. by L. Hench and D. Ulrich, Palm Coast, FL, February 1985, to be published.
8. F.F. Lange and M.M. Hirlinger, "Hindrance of Grain Growth in Al_2O_3 by ZrO_2 Inclusions," *J. Am. Ceram. Soc.* 67[3], 164 (1984).
9. C. Zener, kindly quoted by C.S. Smith, *Trans. Met. Soc. AIME*, 175, 15 (1949).
10. E. Carlstrom and F.F. Lange, "Mixing of Flocced Suspensions," *J. Am. Ceram. Soc.* 67[8], C169 (1984).
11. S.K. Kurtz and F.M.A. Carpay, "Microstructure and Normal Grain Growth in Metals and Ceramics: Part 1, Theory," *J. Appl. Phys.* 51[11], 5725 (1980).
12. F.F. Lange, to be published.

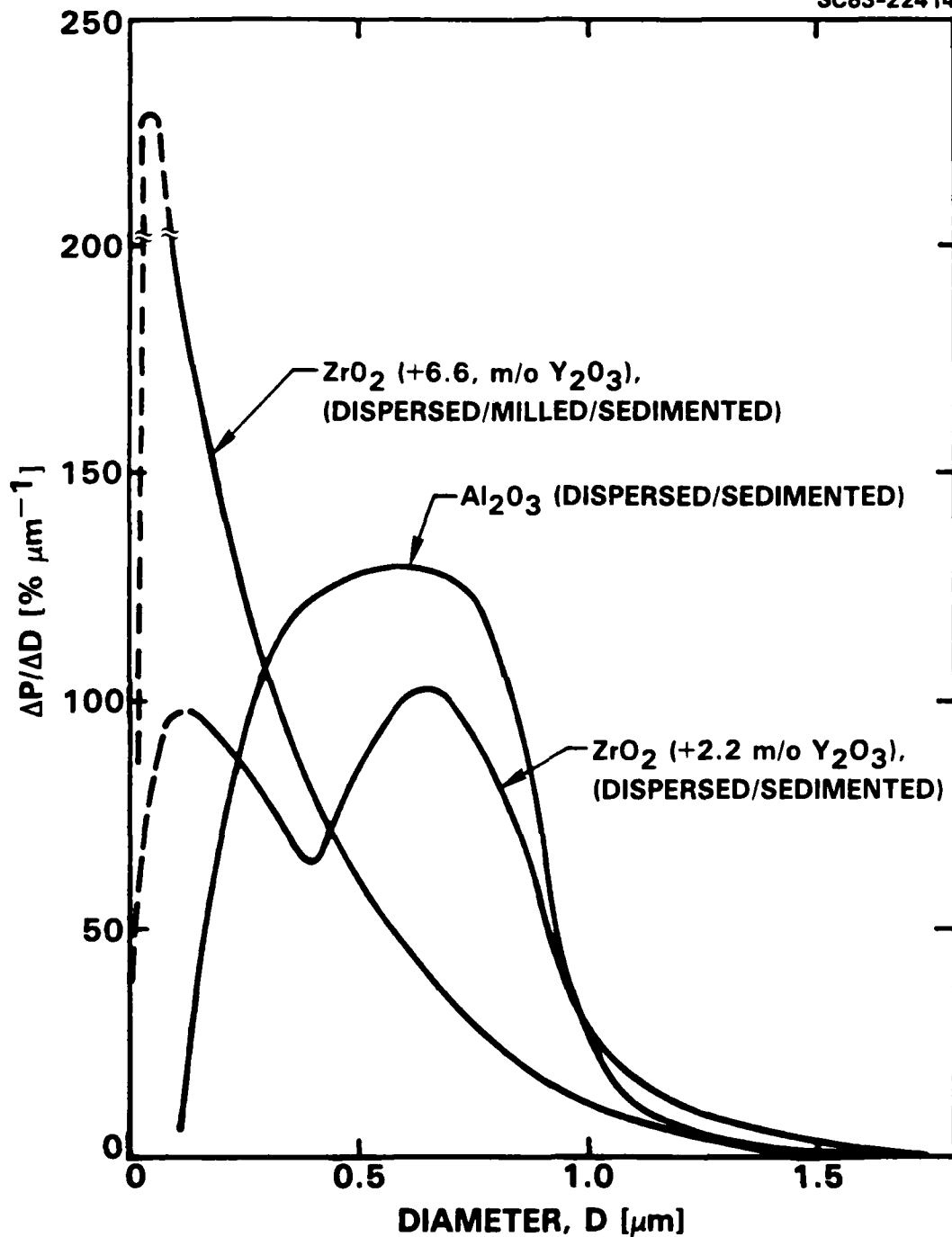


Fig. 1 Size distribution of colloiddally-treated ZrO_2 and Al_2O_3 powders (distribution for sizes $< 0.1 \mu\text{m}$ was not determined and is given by dashed line.)



SC5295.4FR

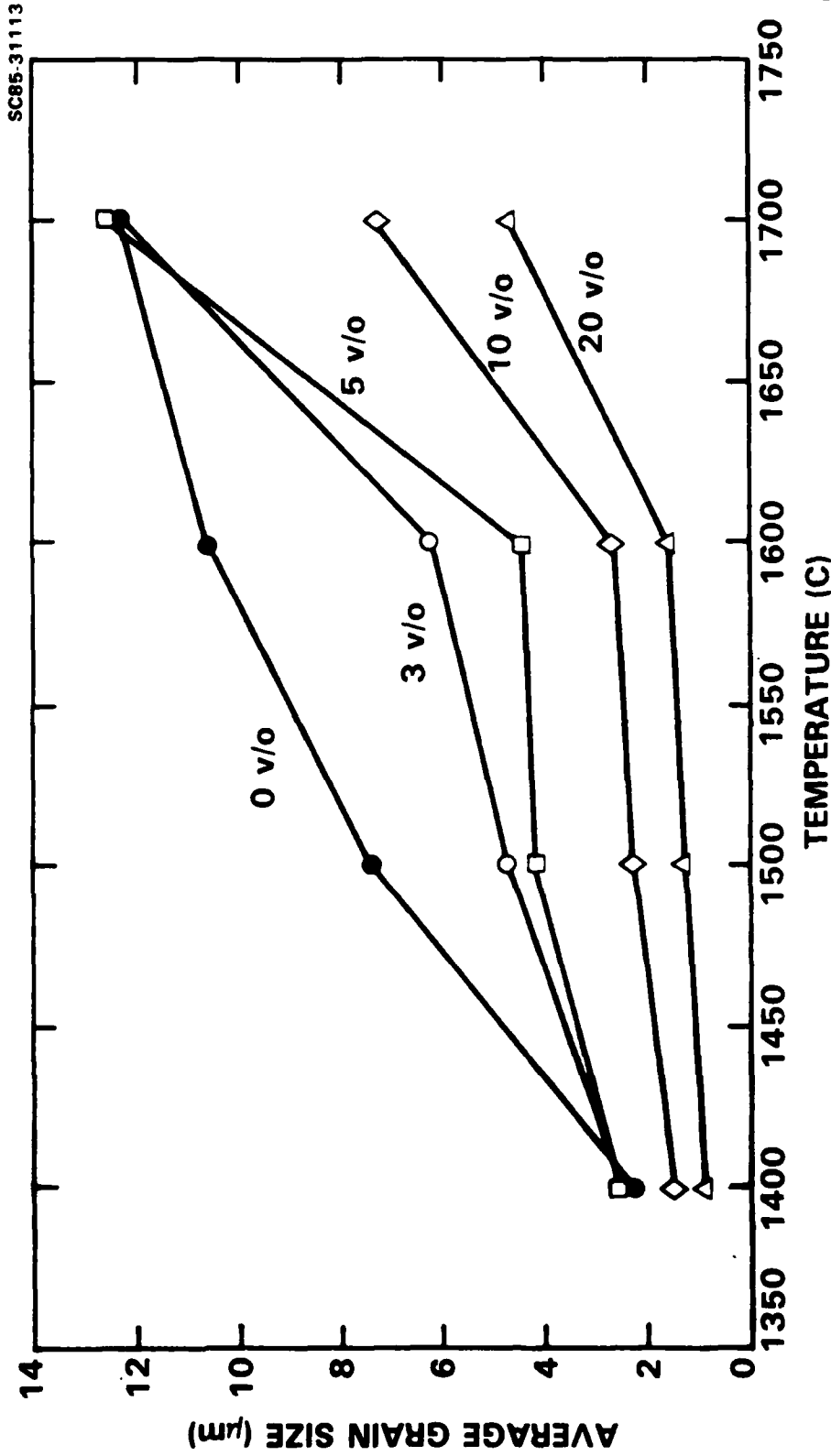


Fig. 2 Mean grain size vs heat treatment temperature for ZrO_2 and Al_2O_3 composite materials.



SC85-30714

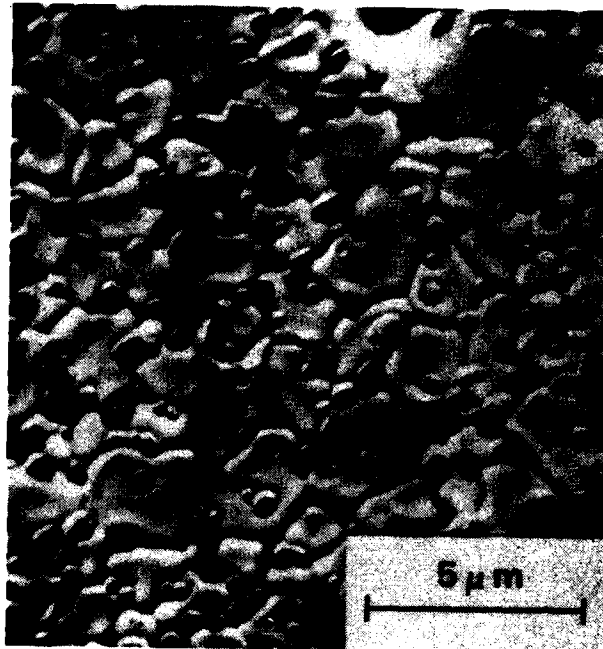


Fig. 3 Micrograph of 20 v/o Al_2O_3 composite heat treated at $1500^\circ C$ showing location and size distribution of Al_2O_3 inclusion phase.



SC85-30716

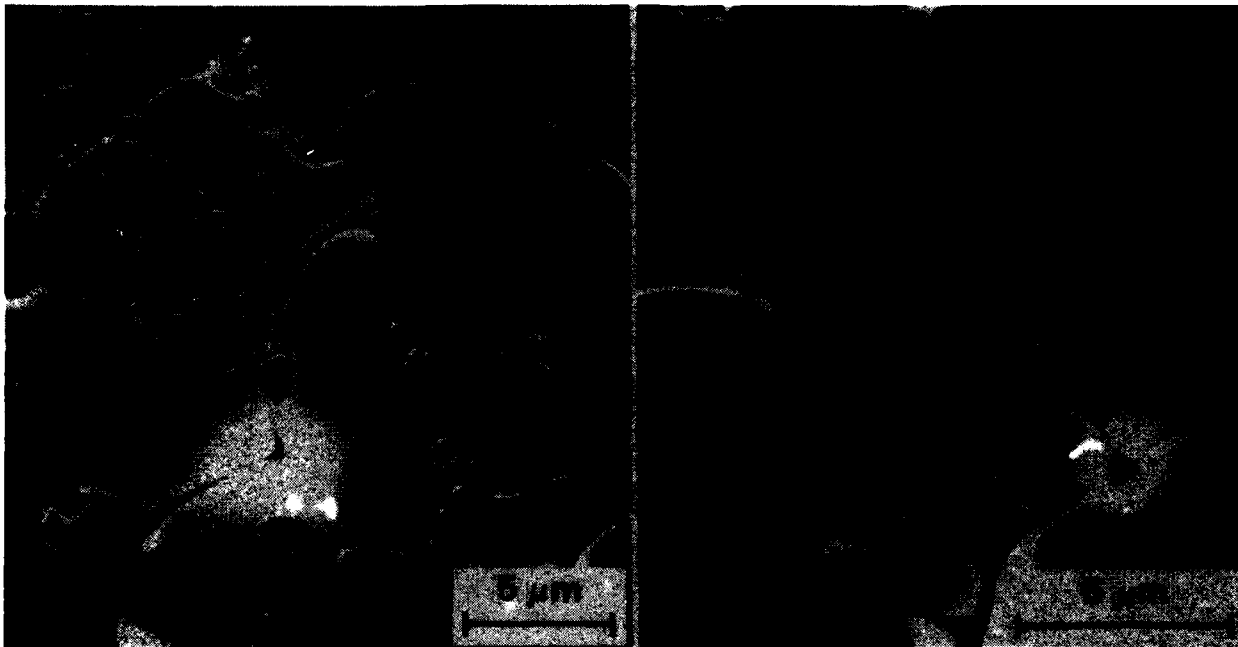


Fig. 4 Two micrographs of 10 v/o Al₂O₃ composite heat treated at 1700°C showing redistribution of Al₂O₃ inclusion phase. Note denuded portions of grains and coalescence of Al₂O₃ inclusions at three- (or four-) grain junctions.



Table 1
Grain Size Parameters

v/o Al ₂ O ₃	Parameter*	1400°C/2 h	1500°C/2 h	1600°C/2 h	1700°C/2 h
0	M (μm)	2.3	7.4	10.6	12.3
	SD (μm)	1.1	3.6	5.4	9.8
	R 2.3	2.5	2.1	3.0	
3	M (μm)	2.5	4.7	6.2	12.2
	SD (μm)	1.2	2.2	3.4	8.3
	R 2.8	2.3	2.3	2.3	
5	M (μm)	2.5	4.2	4.5	12.5
	SD (μm)	1.1	2.0	2.6	7.7
	R 2.2	2.2	2.2	2.4	
10	M (μm)	1.5	2.3	2.7	7.3
	SD (μm)	0.7	1.0	1.3	4.8
	R 2.2	2.1	2.3	2.7	
20	M (μm)	0.9	1.3	1.6	4.7
	SD (μm)	0.4	0.6	0.9	2.5
	R 2.0	2.1	2.1	2.4	

* M = Mean size of ZrO₂ grains.

SD = Standard deviation.

R = Ratio largest grain to mean size.



**Rockwell International
Science Center**

SC5295.4FR

APPENDIX III



SC5295.4FR

TRANSFORMATION TOUGHENED ZrO_2 :
CORRELATIONS BETWEEN GRAIN CONTROL AND COMPOSITION
IN THE ZrO_2 - Y_2O_3 SYSTEM

F.F. Lange

Structural Ceramics
Rockwell Science Center
Thousand Oaks, CA 91360

ABSTRACT

The average grain size of ZrO_2 (+ Y_2O_3) materials sintered at $1400^\circ C$ was observed to significantly depend on the Y_2O_3 content. The average grain size decreased by a factor of 4-5 for Y_2O_3 contents between 0.8-1.4 m/o and increased at Y_2O_3 contents of 6.6 m/o. Grain growth control by a second phase is the concept used to interpret these data. Namely, compositions with a small grain size lie within the two-phase, tetragonal + cubic phase field, and the size of the tetragonal grains is believed to be controlled by the cubic grains. This interpretation suggests that the Y_2O_3 -rich boundary of the two-phase field lies between 0.8 and 1.4 m/o Y_2O_3 . Transformation toughened materials fabricated in this binary system must have a composition that lies within the two-phase field to obtain the small grain size required, in part, to retain the tetragonal toughening agent.



INTRODUCTION

As first demonstrated by Gupta and co-workers^{1,2} for certain ZrO_2 - Y_2O_3 compositions, Y_2O_3 has become a very important solid-solution addition to ZrO_2 which helps in the retention of the tetragonal structure, i.e., the toughening agent, in several different transformation toughened materials, e.g., Al_2O_3/ZrO_2 ,^{3,4} β - Al_2O_3/ZrO_2 ,^{5,6} Mullite/ ZrO_2 .⁷ Retention of the tetragonal structure also requires that the ZrO_2 grains (or inclusions) be less than a critical size.^{2,8,9} Different theoretical studies^{10,11,12} have attempted to explain this critical size effect, but it appears that no one theory is presently consistent with all information.

Figure 1 schematically illustrates the ZrO_2 -rich portion of the ZrO_2 - Y_2O_3 binary system determined by different compositional studies described below. Transformation toughened materials fabricated in this system by different investigators generally contain between 2-4 mole % (m/o) Y_2O_3 and are generally sintered at temperatures between 1300°C and 1600°C. Retention of the tetragonal phase requires that the tetragonal grains be $< 0.3 \mu m$.^{2,10,13} Complete retention of the tetragonal phase below ~ 2 m/o Y_2O_3 has not been reported.

The compositional boundaries of the two-phase, tetragonal (t) + (c), field has been reported by several investigators who have extensively studied the ZrO_2 -rich portion of the ZrO_2 - Y_2O_3 system. Srivastava, et al,¹⁴ indicated that the two-phase field extends from 3.9 to 7.5 mole % Y_2O_3 with the t + m + c eutectoid composition and temperature of 3.9 m/o Y_2O_3 and 565°C, respectively. Scott¹⁵ reported a eutectoid at 2.6 m/o Y_2O_3 and 565°C and indicated that both boundaries slightly curved towards lower Y_2O_3 contents with increasing temperature. Ruhle, et al,¹⁶ analyzed different materials fabricated between 1300°C and 1600°C and reported similar boundary curvatures as indicated by Scott. Pascual and Duran¹⁷ reported the eutectoid at 4.5 m/o Y_2O_3 and 490°C and also indicated that the boundaries curved toward lower Y_2O_3 contents at higher temperatures. Ruh, et al,¹⁸ report "... a two-phase solid



SC5295.4FR

solution plus cubic solid solution exists from 1.5 to 7.5[mole] % Y_2O_3 from 500°C to 1600°C." The Ruh, et al, interpretation of the ZrO_2 - Y_2O_3 system would place all transformation toughened materials presently fabricated in the two-phase field, whereas all other interpretations would indicate that some of the transformation toughened materials (those containing < 2.5 m/o Y_2O_3) are fabricated in the single phase, tetragonal field. As it will be shown, this seemingly insignificant difference in the interpretation of phase boundary location results in a significant difference in grain growth behavior and in the retention of the tetragonal toughening agent.

EXPERIMENTAL PROCEDURE AND RESULTS

Based on the disputed phase boundaries for the two-phase, t + c, field in the ZrO_2 -rich portion of the ZrO_2 - Y_2O_3 system and the well-known fact that second phases can hinder grain growth, experiments were initiated to determine the grain size that is obtained after sintering ZrO_2 powders containing different Y_2O_3 contents (viz., 0, 0.8, 1.4, 2.3, 4.5, and 6.6 m/o Y_2O_3). All powders were obtained from one commercial source*, which manufactured the ZrO_2 (+ Y_2O_3) powder by decomposing $ZrOCl_2$ + yttrium salt solutions at temperatures < 800°C. Although agglomerated, the average crystallite size of these powders is < 0.05 μm .¹⁹ The Y_2O_3 content was determined by spectroscopy.** Preconsolidation powder treatment and the consolidation method is reported elsewhere.²⁰ Powder compacts were sintered in an air furnace at 1400°C for 1 h. Densities for materials that did not exhibit extensive microcracking were determined to be > 0.97 of theoretical. Table 1 lists the phases determined by x-ray diffraction analysis (XRD) of the as-sintered surfaces (or the coarse powder resulting from the highly microcracked materials). It should be noted that small fractions of either cubic phase in

* Zircar Inc., Florida, NY.

** Spectrochemical Laboratories, Inc., Pittsburgh, PA.



SC5295.4FR

a predominately tetragonal material or visaversa, would not be detected because of mutual overlap of discriminating diffraction peaks.

Table 1
Phases Observed by X-Ray Diffraction Analysis

Y ₂ O ₃ Content (m/o)	Structure of ZrO ₂ Phase(s)
0.0	monoclinic
0.8	monoclinic
1.4	monoclinic (+ trace tetragonal)
2.3	tetragonal
4.5	tetragonal + cubic
6.6	cubic

Grain size was determined from scanning electron micrographs of either thermally etched surfaces or fracture surfaces for materials containing < 0.8 m/o Y₂O₃ exhibiting extensive microcracking during cooling. Figure 1 reports the average grain size for the different materials as determined by the line intercept method without correction for either grain shape or volume. Figure 2 illustrates microstructures typical of the a) < 0.8 m/o Y₂O₃ materials, b) 2.3 m/o Y₂O₃, and c) 6.6 m/o Y₂O₃ materials. As reported in Figs. 1 and 2, the average grain size abruptly decreases for Y₂O₃ contents between 0.8 and 1.4 m/o Y₂O₃. Material containing 4.5 m/o Y₂O₃ had larger (~ 1 μm) grains distributed among the smaller grains, which appears to account for the slight increase in grain size. Selected area electron diffraction analysis of similar materials by other investigators have shown that the larger grains have the cubic structure, whereas, the smaller grains are tetragonal.¹⁶ Table 1 also shows that this material contains both cubic and tetragonal phases, consistent with all phase equilibrium studies mentioned above.



DISCUSSION

The above data show that grain size is governed by composition. Since materials with the smallest grain sizes have compositions that could lie within the $t + c$ two-phase field, it can be argued that the cubic grains control the growth of the tetragonal grains. Control of grain growth is lacking for composition < 0.8 m/o Y_2O_3 . All phase investigations mentioned above conclude that these compositions lie within a single-phase (monoclinic) field. Likewise, grain growth control is lacking for compositions > 6.6 m/o Y_2O_3 , which most investigations agree lies close to the Y_2O_3 -rich boundary of the two-phase field. If one accepts the argument that one phase controls the size of the other phase, one might conclude that microstructure, which can be more sensitive to the presence of a second phase relative to differential thermal analysis and XRD techniques commonly used to define phase boundaries might be a better judge for the location of a two-phase boundary, particularly for systems that undergo a constrained phase transformation. With this in mind, the present data appear more consistent with the phase boundaries recently reported by Ruh, et al.¹⁸

ACKNOWLEDGEMENT

Support of this work by the Air Force Office of Scientific Research under Contract No. F49620-81-C-0036 is greatly appreciated.



REFERENCES

1. T.K. Gupta, J.H. Bechtold, R.C. Kuznicki, L.H. Cadoff, and B.R. Rossing, "Stabilization of Tetragonal Phase in Polycrystalline Zirconia," *J. Mat. Sci.* 12, 2421 (1977).
2. T.K. Gupta, F.F. Lange, and J.H. Bectold, "Effect of Stress-Induced Phase Transformation on the Properties of Polycrystalline Zirconia Containing Tetragonal Phase," *J. Mat. Sci.* 13, 1464 (1978).
3. F.F. Lange, "Transformation Toughening: Part 4, Fabrication, Fracture Toughness, and Strength of $Al_2O_3-ZrO_2$ Composites," *J. Mat. Sci.* 17, 247 (1982).
4. F.F. Lange, " Al_2O_3/ZrO_2 Ceramic," U.S. Patent 4,316,964, February 23, 1982.
5. F.F. Lange, B.I. Davis, and D.O. Raleigh, "Transformation Strengthening of $-Al_2O_3$ with Tetragonal ZrO_2 ," *J. Am. Ceram. Soc.* 66[3], C-50 (1983).
6. F.F. Lange, "Sodium Ion Conductor, Solid Electrolyte Strengthening with Zirconia," U.S. Patent 4,358,516, Nov. 9, 1982.
7. F.F. Lange and I.A. Aksay, "Transformation-Toughened Mullite/ $ZrO_2(+ Y_2O_3)$," to be published.
8. F.F. Lange, *ibid* ref 3, "Part III, Experimental Observations in the $ZrO_2-Y_2O_3$ System," pp 240.
9. D.J. Green, "Critical Microstructures for Microcracking in $Al_2O_3-ZrO_2$ Composites," 65[12], 610 (1982).
10. F.F. Lange, *ibid* Ref. 3, "Part I, Size Effects Associated with the Thermodynamics of Constrained Transformations," pp 225.
11. M. Ruhle and A.H. Heuer, "Phase Transformation in ZrO_2 -Containing Ceramics: II, The Martensitic Reaction in $t-ZrO_2$," *Advances in Ceramics*, Vol 12, Science and Technology of Zirconia II, ed. by Nils Claussen, Manfred Ruhle, and Arthur H. Heuer, pp 14, Am. Ceram. Soc., Columbus, OH (1984).
12. I-Wei Chen and Y-H Chiao, "Martensitic Transformations in ZrO_2 and HfO_2 -An Assessment of Small-Particle Experiments with Metal and Ceramic Matrices," *ibid*, pp 33.
13. M. Watanabe, S. Lio, and I Fukuura, "Aging Behavior of Y-TZP," *ibid*, pp 391.



SC5295.4FR

14. K.K. Srivastava, R.N. Patil, C.B. Chaudhary, K.V. Gokhale, and E.C. Subbarao, "Revised Phase Diagram of the System ZrO_2-YO_{1-5} ," Trans. J. Br. Ceram. Soc. 73, 85 (1975).
15. H.G. Scott, "Phase Relationship in the Zirconia-Yttria System," J. Mat. Sci. 10, 1527 (1974).
16. M. Ruhle, N. Claussen, and A.H. Heuer, "Microstructural Studies of Y_2O_3 -Containing Tetragonal ZrO_2 Polycrystals (Y-TZP)," ibid Ref 11, pp 352.
17. C. Pascual and P. Duran, "Subsolidus Phase Equilibria and Ordering in the System $ZrO_2-Y_2O_3$," J. Am. Ceram. Soc. 66, 23 (1983).
18. R. Ruh, K.S. Mazdhyasni, P.G. Valentine, and H.O. Bielstein, "Phase Relations in the System $ZrO_2-Y_2O_3$ at Low Y_2O_3 Contents," ibid, 67, C-190 (1984).
19. I.A. Aksay, F.F. Lange, and B.I. Davis, "Uniformity of $Al_2O_3-ZrO_2$ Composites by Colloidal Filtration," J. Am. Ceram. Soc. 66[10], C-190 (1983).
20. F.F. Lange and B.I. Davis, "Sinterability of ZrO_2 and Al_2O_3 Powders: The Role of Pore Coordination Number Distribution," ibid Ref. 11, pp 669.

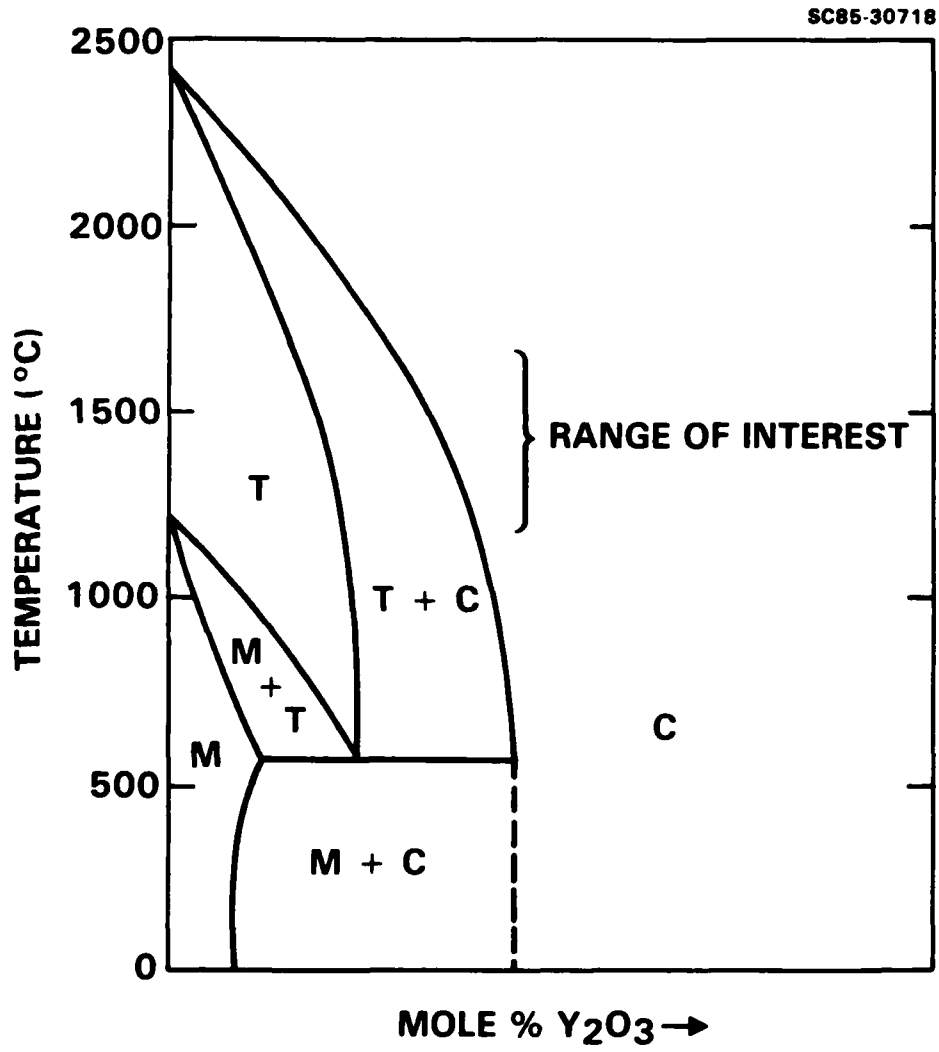


Fig. 1 Schematic of the ZrO_2 -rich portion of the ZrO_2 - Y_2O_3 system.

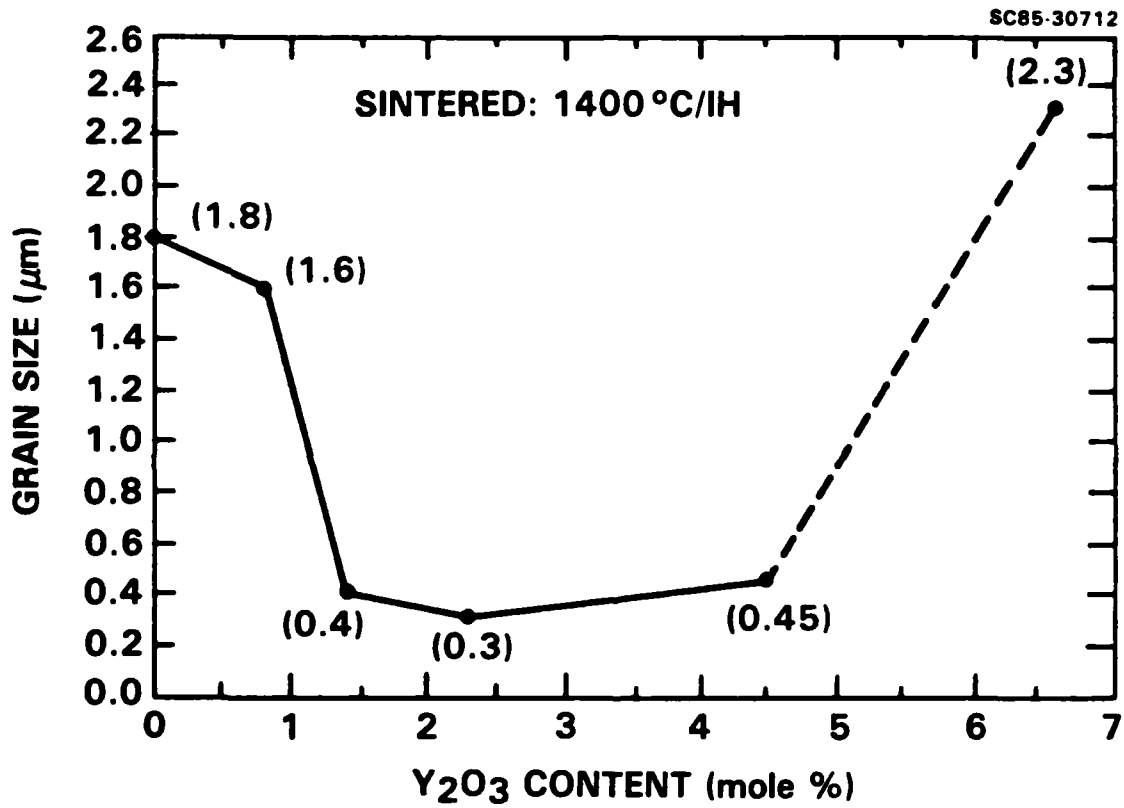


Fig. 2 Average grain size vs Y₂O₃ content measured on () thermally etched surface or () fracture surfaces. Numbers in brackets are the average grain size in microns.



SC85-30715

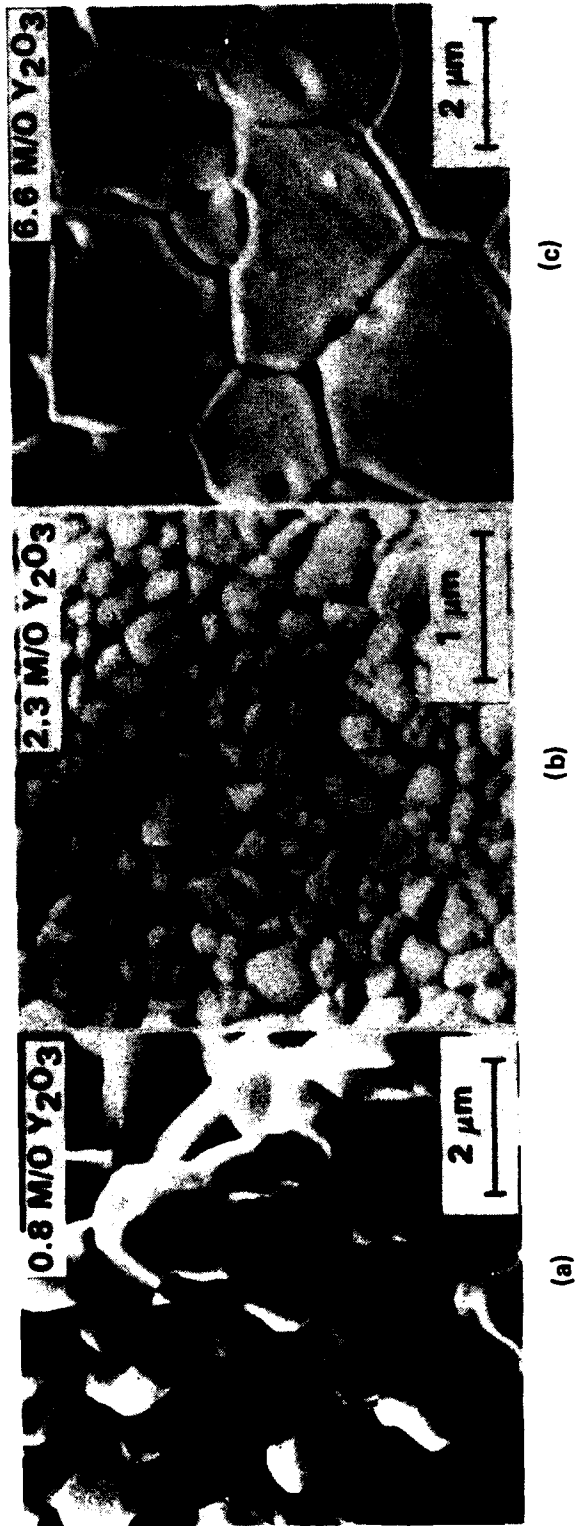


Fig. 3 Micrographs of different materials containing (a) 0.8 m/o Y₂O₃,
(b) 2.3 m/o Y₂O₃ and (c) 6.6 m/o Y₂O₃.



**Rockwell International
Science Center**

SC5295.4FR

APPENDIX IV



ON THE RETENTION OF EQUIAXED GRAIN STRUCTURE AFTER SUPERPLASTIC
AND OTHER FORMS OF HIGH TEMPERATURE DEFORMATION

R. Raj*
Department of Materials Science and Engineering
Cornell University
Ithaca, NY 14853

and

F.F. Lange
Rockwell International Science Center
Thousand Oaks, CA 91360

ABSTRACT

Whereas deformation of grains in a polycrystal will tend to produce nonequilibrium dihedral angles at the triple grain junctions, local diffusive migration of grain boundaries will seek to restore the equilibrium configuration at triple junctions. The kinetics of this equilibration process is estimated and is shown to be fast compared to the usual rates of deformation at elevated temperature. It is further proposed that the equilibrium dihedral angles in deformed polycrystals will give rise to curved interfaces, which will force migration of boundaries in such a direction that the equiaxed grain structure of the polycrystal is restored. An approximate expression for the critical strain-rate below which the rate of migration of the boundaries will be fast enough to maintain the equiaxed structure is derived. The result is in fair agreement with the experiments by Rachinger. The role of applied stress in inducing migration of grain boundaries is also discussed, but in a qualitative way.

*Consultant, Rockwell International Science Center.

To be submitted to Acta Metallurgica



INTRODUCTION

Although there is little doubt that stress induced diffusion transport between grain interfaces, across distances of about the grain size (1-4), plays a significant role in superplastic flow of polycrystalline materials, certain microstructural observations, such as strain induced grain growth, grain rotation, and the equiaxed grain size, have yet to be satisfactorily explained. In this paper we describe a mechanism for the retention of the equiaxed grain shape even after the material has been deformed to large superplastic deformations.

Perhaps the suggestion by Ashby and Verrall (5,6), who developed an idea proposed by Rachinger (7), is the only viable mechanism by which grains, by switching their neighbors, can produce large strains without changing their shape. The model is not quite complete, however, since the grain switching events are discrete each producing a tensile strain of 0.55 units, and can occur only once for a given direction of strain. Superplastic deformations can be considerably greater which suggests that other mechanisms for grain boundary migration and grain shape change must operate, either independently or in concert with the grain-switching mechanism.

In fact from experiments of Rachinger (7) it would appear that diffusional creep is not a pre-requisite for the retention of equiaxed grain shape. If that is the case then the mechanism by which boundaries migrate to restore the equiaxed grain shape may be independent of the grain-switching process used to describe superplastic flow. Before describing an alternative mechanism we discuss Rachinger's observations in detail.

RACHINGER'S EXPERIMENTS ON DEFORMATION AND GRAIN ELONGATION

Equiaxed polycrystals of 99.95% aluminum, with a grain size of 98.8 μm were deformed to a strain of approximately 0.5, at a slow strain-rate, $2.8 \times 10^{-7} \text{ s}^{-1}$, and at a fast strain-rate, $1.7 \times 10^{-3} \text{ s}^{-1}$, in the temperature range 293K-623K. The aspect ratio of the grains after deformation, and the



SC5295.4FR

ratio of volume of the average grain after deformation to the volume before deformation, were measured. The results are summarized in Table I. They show that if the strain rate is slower than $2.8 \times 10^{-7} \text{ s}^{-1}$ and the temperature is between 523K and 623K then the grains remain equiaxed in spite of the strain of 0.5 applied to the specimen. Furthermore at 523K and 573K, grain growth was insignificant suggesting that deformation induces a driving force for migration which restores equiaxed grain shape, but it does not necessarily also induce an additional driving force for grain-growth. (If one takes the liberty of extrapolating this result to superplasticity it would mean that strain induced grain growth in such deformation is not necessarily coupled to that aspect of the migration of boundaries which keeps the grains equiaxed.)

In order to show that diffusional creep is not a pre-requisite for the retention of the equiaxed grain shape, we seek to determine the mechanism of deformation for the strain rate at which the equiaxed structure was observed (Table I: $2.8 \times 10^{-7} \text{ s}^{-1}$ at 523K). Consider that aluminum is deforming through diffusional and power law creep. The flow equation is then given by:

$$\dot{\epsilon} = 14 \frac{\sigma \Omega}{kT} \frac{1}{L^2} (D_V + \frac{\delta D_b}{L} D_b) + A \frac{D_V G b}{kT} \left(\frac{\sigma}{G}\right)^n \quad [1]$$

where σ and $\dot{\epsilon}$ are the tensile stress and strain-rate, L is the grain size and the other parameters have their usual meaning. For aluminum, we use the values given in Ref. 8: $\Omega = 1.66 \times 10^{-29} \text{ m}^3$, $b = 2.86 \times 10^{-10} \text{ m}$, G (at 523K) = $2.23 \times 10^{10} \text{ Pa}$, $D_V = 1.71 \times 10^{-4} \exp(-142 \text{ kJ mole}^{-1}/RT) \text{ m}^2 \text{ s}^{-1}$, $\delta D_b = 5 \times 10^{-14} \exp(-84 \text{ kJ mole}^{-1}/RT) \text{ m}^3 \text{ s}^{-1}$, $A = 3.4 \times 10^6$ and $n = 4.4$. The plot of Eq. [1], given in Fig. 1, shows that the transition from diffusion to power-law creep is expected at $1.5 \times 10^{-11} \text{ s}^{-1}$. Since the strain-rate in Rachinger's experiments was faster by a factor of more than 10^4 , we can be quite certain that at 523K his material was deforming predominantly by dislocation flow mechanisms, and not by diffusional creep.



SC5295.4FR

In summary, we conclude from Rachinger's experiments that the retention of the equiaxed grain shape after large strains can occur even when a polycrystal is deforming by dislocation mechanisms. The observation that grains remain equiaxed after large superplastic strains does not necessarily imply that the retention of the equiaxed structure is coupled to the diffusional creep (or to the grain switching) mechanism.

A NEW MODEL FOR RETAINING EQUIAXED STRUCTURE BASED ON THE DIHEDRAL ANGLE

a. Equilibration of Dihedral Angles at Triple Junctions

If grain-interface energies are isotropic then the dihedral angles where three grains meet will each be equal to $2\pi/3$. At elevated temperatures, if that equilibrium configuration is distorted due to deformation, then local grain boundary diffusion will seek to restore equilibrium. Consider, for example, fast deformation of a polycrystal from an equiaxed structure, Fig. 2(a), to a flattened structure shown in Fig. 2(b). The dihedral angles at the triple point will then be restored to their equilibrium value by diffusive boundary migration in the manner shown in Figs. 2(c)-(e). The boundaries will migrate from the triple junction, outwards, driven generally by the need to reduce interface energy, but locally by the curvature in the grain boundary, denoted by ρ in Fig. 2. An approximate expression for the distance z that the boundary would have migrated in time t can be calculated by assuming the ρ is approximately equal to z . The driving force for boundary migration, ΔP_b , will then be given by:

$$\Delta P_b = \frac{2\gamma_b \Omega}{\rho} \sim \frac{2\gamma_b \Omega}{z} \quad [2]$$

where γ_b is the grain boundary energy and Ω is the atomic volume. Following Turnbull (9) and assuming that z is approximately equal to the migration velocity we have the equation:

$$z \approx \frac{\Delta P_b}{kT} \frac{\delta D_b}{\Omega^{2/3}} \quad [3]$$



SC5295.4FR

where we assume that kinetics of boundary migration is controlled by grain boundary diffusivity (this assumption is reasonably valid for pure metals but not when impurities are present or when the boundaries are special coincidence boundaries (10)). Combining Eqs. [2] and [3] and integrating we obtain:

$$z^2 = \frac{4\gamma_b \Omega^{1/3}}{kT} \delta D_b \cdot t \quad [4]$$

A plot of Eq. [4] for aluminum, assuming $\gamma_b = 0.6 \text{ Jm}^{-2}$ and the value for δD_b given earlier, is given in Fig. 3. Note that close to the triple junction the dihedral angle is restored very quickly: for example at 523K it takes only 1 ms to achieve the equilibrium configuration up to a distance of 0.1 μm from the triple junction.

b. Grain Boundary Migration Induced by Deformation

Here we shall derive a condition on the applied strain-rate such that when the applied strain rate is less than a critical value, the grains will remain equiaxed even though deformation has the effect of elongating the grains in the direction of the applied strain. The basis of the analysis is that deformation distorts the dihedral angles. As those angles seek to reestablish their equilibrium configuration they produce a driving force for grain boundary migration such that the equiaxed grain shape is restored.

Except for one nearly impossible case (illustrated in Fig. 4 where all grains are identical, equiaxed and two-dimensional) deformation of grains, by any mechanism, will lead to nonequilibrium dihedral angles if the grain facets are forced to remain flat. The equilibrium angles can be conserved if the grain facets assume a curvature, the degree of curvature being related to the aspect ratio of the grains. In general, the sense of the curvature will be such as to restore the grain to its equiaxed shape, as illustrated in Fig. 5. Consider for example the change in the dihedral angle θ at triple junction A. A horizontal tensile strain will move the triple junction to A' and cause θ to decrease if the curvature of the grain facets forming that



SC5295.4FR

angle does not change. If, however, the new angle is required to remain at equilibrium, that is $\theta = \theta' = 2\pi/3$, then the curvature of the grain facets will change in such a manner that the boundaries will seek to migrate and restore the equiaxed shape of the grain. We wish to caution that a polycrystal consists of grains of different shapes and sizes. All grain-boundaries, therefore, will not migrate together in a self-similar fashion. Rather the migration would be stochastically and spatially distributed, although deformation will have the effect of increasing the relative probability for that direction of migration which seeks to restore the equiaxed shape of the grains.

Since grain boundary migration is a diffusion controlled, time dependent process the grains will remain equiaxed during deformation only if the applied strain-rate is slow enough to allow time for migration to occur. An approximate expression for the strain-rate below which the grains remain equiaxed can be derived as follows. Assume that the equiaxed grain-size is L , that at a given strain-rate the grains assume a "steady state" aspect ratio of A_b , and the radius of curvature of the grain facets is approximately ρ . Then from geometrical and scaling arguments we can write that

$$\frac{L}{\rho} = \alpha A_b \quad [5]$$

where α is a constant. It must be $\ll 1$ since when $A_b = 1$ (perfectly equiaxed grains) then $\rho \gg L$ since the grain facets will be almost flat. In our judgment $\alpha = 0.01$ would be a reasonable working number for engineering calculations.

Substituting for ρ from Eq. [5] in [2] and [3] and replacing \dot{z} by the migration velocity v_b we get the result:

$$v_b = 2\alpha A_b \frac{\gamma_b \Omega^{1/3}}{kTL} \delta D_b \quad [6]$$



The critical strain-rate, $\dot{\epsilon}_c$, below which the grains remain equiaxed will be given by:

$$\dot{\epsilon}_c = \frac{v_g}{L} \quad [7]$$

Combining [6] and [7] leads to the result that:

$$\dot{\epsilon}_c = 2\alpha A_b \frac{\gamma_b \Omega^{1/3}}{L^2 kT} \delta D_b \quad [8]$$

where $\alpha \approx 10^{-2}$ and $A_b \approx 1$ for equiaxed grain structure. Interestingly, according to Eq. [8], for a given applied strain-rate a smaller grain-size is more likely to remain equiaxed.

DISCUSSION

Rachinger's experiments can be compared with the prediction from Eq. [8]. As discussed earlier, he found that the grain-structure remained equiaxed if the temperature was greater than 523K at a strain-rate of $2.8 \times 10^{-7} \text{ s}^{-1}$ in aluminum having a grain size of 98.8 μm .

Substituting $\gamma_b = 0.6 \text{ Jm}^{-2}$, $\Omega = 1.66 \times 10^{-29} \text{ m}^3$, $\delta D_b = 5 \times 10^{-14} \exp(-84 \text{ kJ mole/RT}) \text{ m}^3 \text{ s}^{-1}$, $T = 523\text{K}$, $L = 98.8 \mu\text{m}$, $\alpha = 10^{-2}$ and $A_b = 1$, we obtain that $\dot{\epsilon}_c = 8.6 \times 10^{-6} \text{ s}^{-1}$. Even though this is about 30 times faster than the measured value of $2.8 \times 10^{-7} \text{ s}^{-1}$, the comparison is not far fetched in view of the approximations made in the derivation of Eq. [8]. Another possible source of the discrepancy may be that Rachinger's experiments were done on 99.95% pure aluminum, and even trace amounts of impurity can retard the rate of grain boundary migration. Equation [3], which was used in the derivation of [8], has been shown to hold only for zone-refined metals [10].



Rockwell International
Science Center

SC5295.4FR

ACKNOWLEDGMENT

This work was supported by the Air Force Office of Scientific Research, Contract No. F49620-81-C-0036. Stimulating discussions with Prof. H.J. Frost and Dr. A.K. Ghosh are gratefully acknowledged.



REFERENCES

1. F.R.N. Nabarro, Conf. Strength of Solids, p. 75, Inst. Phys. (1948).
2. C. Herring, J. Appl. Phys. 21, 437 (1950).
3. R.L. Coble, J. Appl. Phys. 34, 1679 (1963).
4. R. Raj and M.F. Ashby, Trans. Metall. Soc. AIME, 2, 1113 (1971).
5. M.F. Ashby and R.A. Verrall, Acta Metall. 21, 149 (1973).
6. J.R. Springarn and W.D. Nix, Acta Metall. 26, 1389 (1978).
7. W.A. Rachinger, J. Inst. Metals 81, 33 (1952-3).
8. H.J. Frost and M.F. Ashby, Deformation Mechanism Maps, 1982, Pergamon Press, NY.
9. D. Turnbull, Trans. TMS-AIME, 191, 661 (1951).
10. P. Gordon and R.A. Vandermeer, "Grain Boundary Migration," Recrystallization Grain Growth and Textures, ASM, Metals Park, p. 205, 1966.

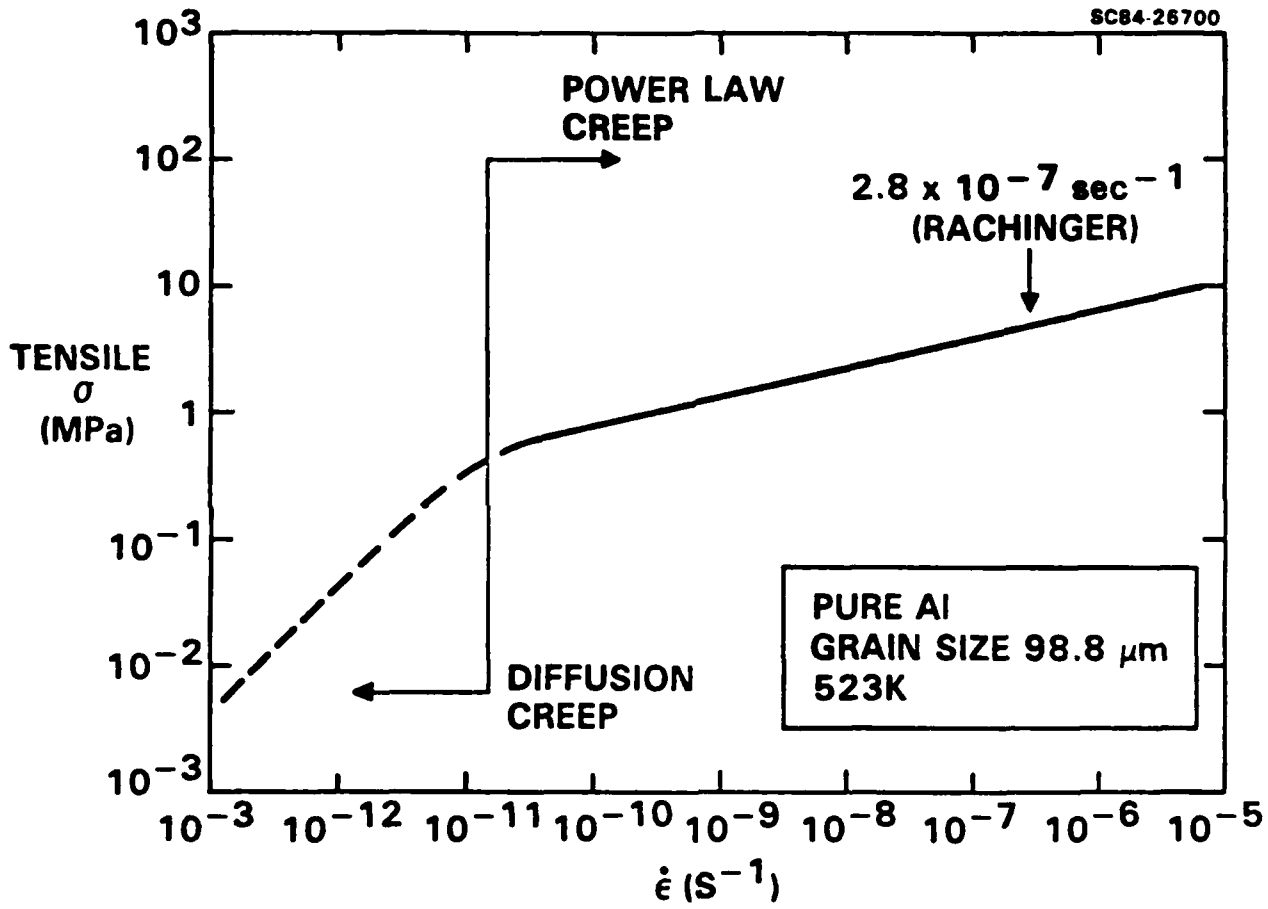


Fig. 1 A deformation map separating regimes of diffusional creep and power law creep for pure aluminum of 98.8 μm grain size at 523K. Rachinger's experiments were well within the region of power-law creep.

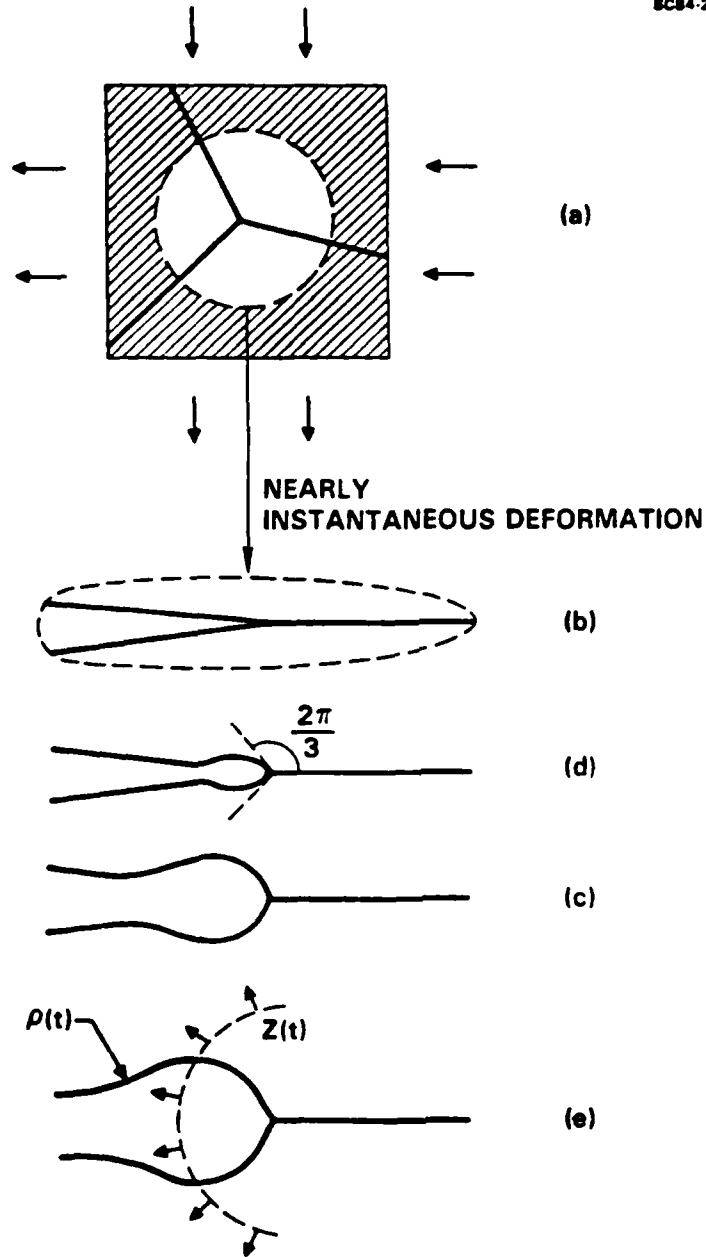


Fig. 2 Fast deformation will lead to nonequilibrium dihedral angles at triple junctions (a - b). Boundary migration (c - e) will attempt to restore the angles to $2\pi/3$.

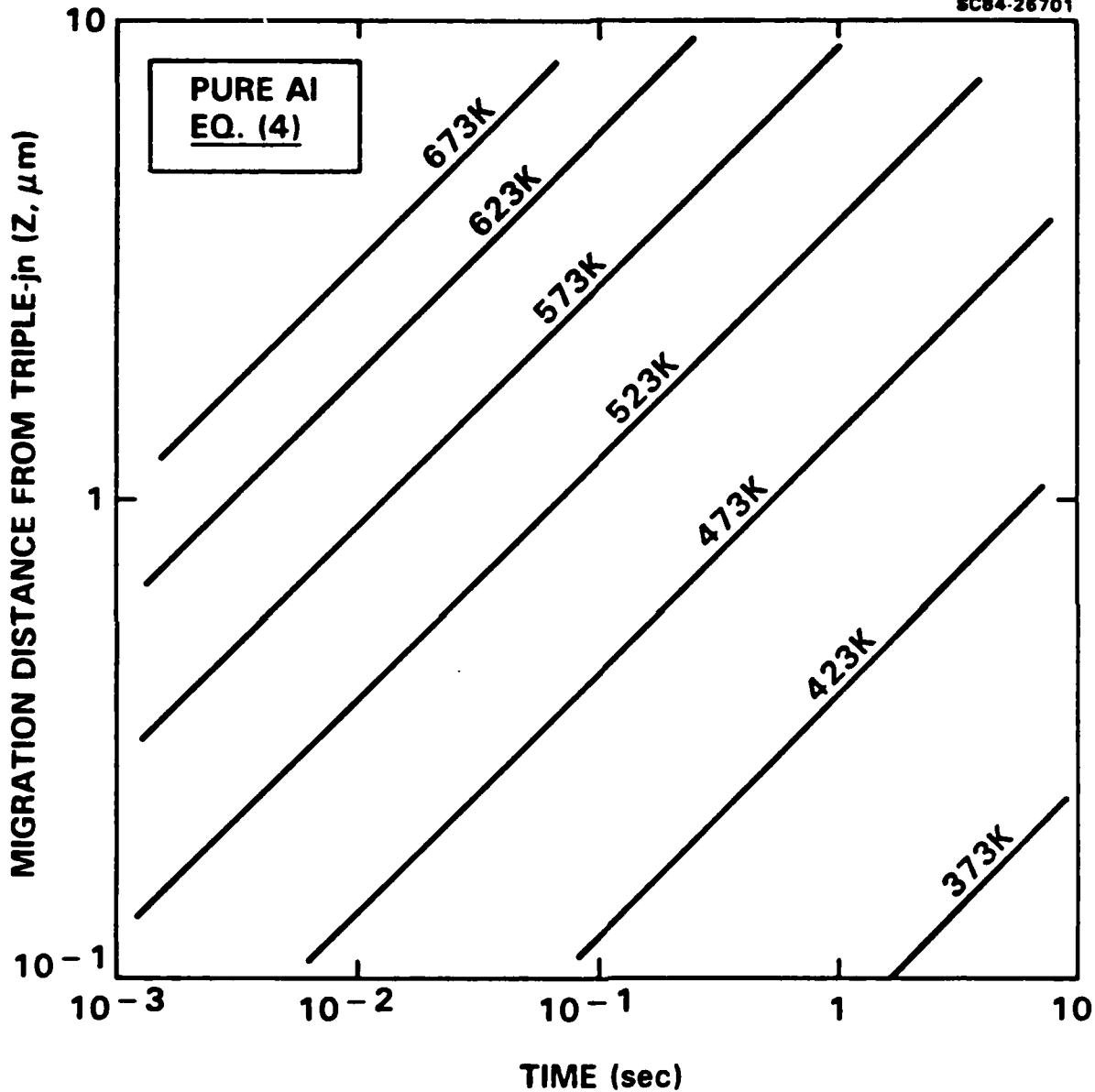


Fig. 3 The distance z in Fig. 2 (e) as a function of time at various temperatures for pure aluminum, as given by Eq. [4].



SC84-26702

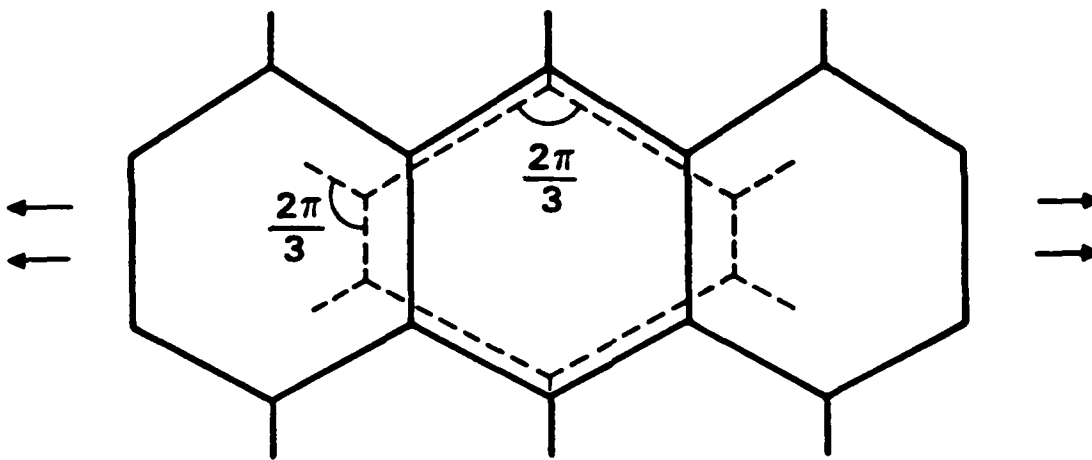


Fig. 4 In a two dimensional, perfectly equiaxed microstructure, it is conceivable that all grains can deform in a self-similar manner and still conserve the dihedral angles at the triple grain junctions. In a real, three dimensional packing such an event would be unlikely.

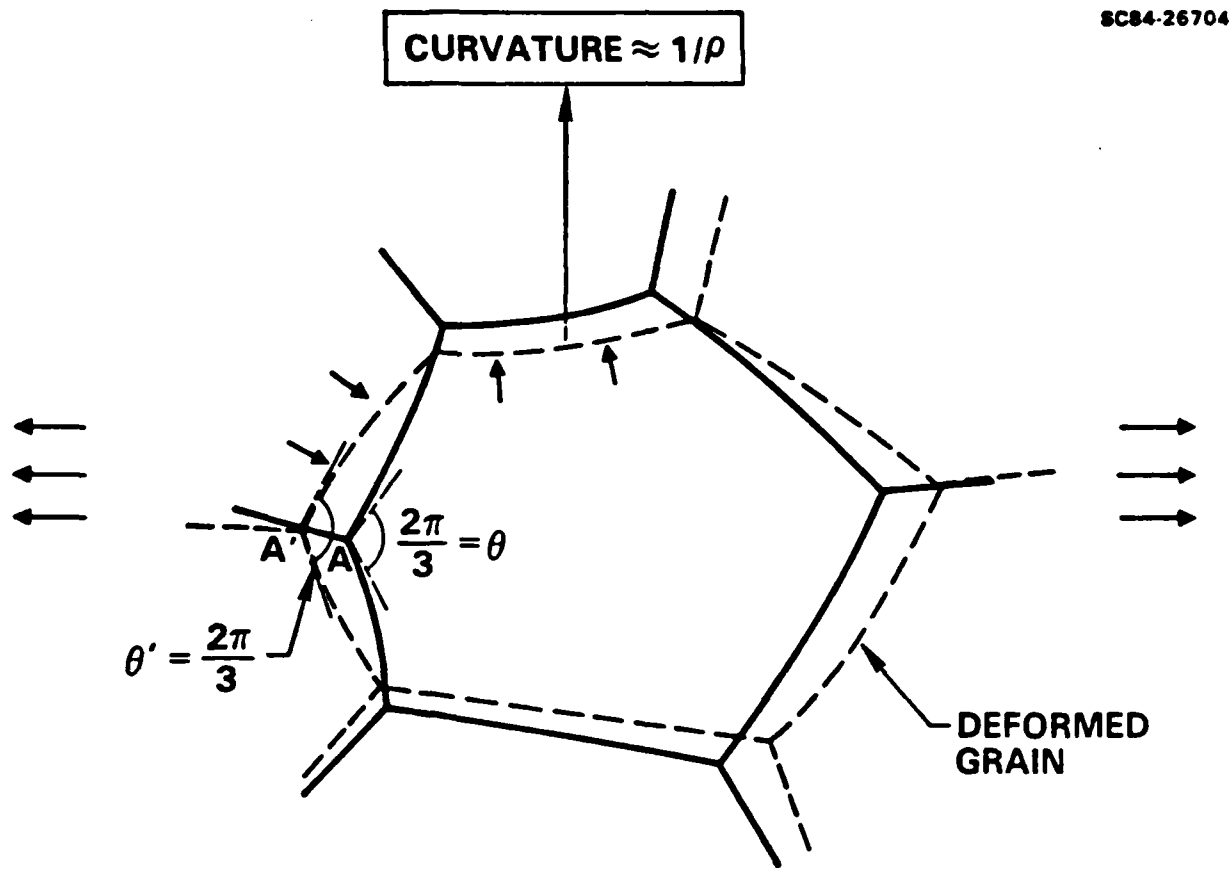


Fig. 5 In polycrystal containing a distribution of grain size and grain shapes, deformation followed by equilibration of the dihedral angles will lead to curvatures at grain interfaces which will drive migration in a direction such that the equiaxed grain structure is restored.



Table I
A Summary of Results Obtained by Rachinger (7)

T (K)	$\dot{\epsilon}$ s^{-1}	Aspect Ratio After Deformation	Total Applied Strain	Grain Volume After Deformation Grain Volume Before Deformation
293	2.8×10^{-7}	1.91	0.52	0.99
373	2.8×10^{-7}	1.78	0.53	1.04
473	2.8×10^{-7}	1.60	0.42	1.11 *
523	2.8×10^{-7}	1.07	0.48	1.10
573	2.8×10^{-7}	1.09	0.47	1.16
623	2.8×10^{-7}	1.13	0.51	1.52
293	1.3×10^{-3}	1.94	0.49	1.08
623	1.3×10^{-3}	1.85	0.59	1.09

(error \pm 4% to \pm 8%)

*The enclosed area marks the transition from elongated to equiaxed grain shape, without a significant increase in grain size.



Rockwell International
Science Center

SC5295.4FR

APPENDIX V



STRENGTH CHARACTERISTICS OF TRANSFORMATION-TOUGHENED ZIRCONIA

D.B. Marshall and M.R. James

Rockwell International Science Center
Thousand Oaks, CA 91360

ABSTRACT

Mechanisms of failure in a transformation-toughened Mg-PSZ are identified using in situ observations. The observations are related to measured stress-strain curves, strengths under various loading conditions, strength degradation from surface damage, and comparative strengths and toughnesses of toughened and overaged materials. Both reversible and irreversible tetragonal-to-monoclinic transformation, as well as microcracking, are associated with nonlinear stress strain curves. Failure is preceded by stable growth of microcracks, resulting in R-curve behavior and damage-tolerant strength characteristics. The implications of R-curve response on strengthening and toughening characteristics are discussed.

I. INTRODUCTION

Transformation toughened ceramics can possess both high strengths and high fracture toughnesses.¹⁻¹⁵ However, the highest strengths and toughnesses are not generally achieved in the same material. In the Al_2O_3/ZrO_2 and the fully tetragonal ZrO_2 systems, strengths above 2 GPa and toughnesses $\sim 10 \text{ MPa}\cdot\text{m}^{1/2}$ have been reported.¹⁰⁻¹² However the highest toughnesses $\sim 14 \text{ MPa}\cdot\text{m}^{1/2}$ have been obtained in precipitated partially stabilized zirconia (PSZ),^{13,14} where the strength is less than 800 MPa. A lack of correlation between strength and toughness has also been observed within each of the these material systems. Marmach and Swain¹³ showed that, in a series of aging



experiments in magnesia-partially-stabilized zirconia (Mg-PSZ), the peak strength was achieved at shorter aging time than the peak toughness. Similarly, in the Y_2O_3 -tetragonal-zirconia system, Tsukuma and Shimada¹² found that peak toughnesses and strengths were obtained at different Y_2O_3 contents, and in an $Y-ZrO_2$ material containing up to 20 volume percent Al_2O_3 , Tsukuma, et al,¹⁵ found peak toughness and strength at different Al_2O_3 contents. An understanding of factors that govern the strength of these materials and the relation between strength and toughness is needed in order to guide development of improved microstructures.

Observed strength-toughness relations are also not in accord with expectations of simple theories of strength of brittle materials. These theories are based on the concept that strength is governed by the extension of a pre-existing dominant crack at a critical stress. This, along with the notion that the size of strength-controlling defects generally scales with microstructural dimensions, has led to the relatively low strength of Mg-PSZ being attributed to its large grain size. However the same argument cannot be used to explain the strength and toughness variations within each material system, for there the grain size does not change. The inability of conventional strength relations to account for the strength of these materials is also evident from a calculation of the size of the pre-existing defect required to cause failure. According to the Griffith relation¹⁶ ($\sigma = K_c \pi^{1/2} / 2 c^{1/2}$, where σ is the strength, K_c the fracture toughness and c the crack radius) the requisite crack diameter for Mg-PSZ ($K_c = 14$ MPa, $\sigma = 600$ MPa) is $600 \mu\text{m}$, about a factor of 10 larger than the grain size. Cracks of this size are not evident on polished surfaces of this material (see Section III) nor would they be produced directly by microcracking. Moreover, the ability to prepare slices of the material with thickness less than $500 \mu\text{m}$ indicates that such defects do not pre-exist.

Similar discrepancies between calculated and observed crack sizes exist in other large grained materials such as alumina, but the predicted flaw size (~ 3 times the grain size) is not as large as in Mg-PSZ. The existence



of a crack-size-dependent toughness (R-curve) and residual microstructural stresses have been proposed to explain strength/grain-size relations in these materials.¹⁷⁻²¹ R-curve behaviour has been predicted^{22,23} and observed^{9,24} for long cracks (double cantilever beams and notched flexural beams) in Mg-PSZ, but the response of smaller strength-controlling cracks has not been examined.

The strength of transformation toughened materials is also likely to be influenced directly by transformation effects. A recent study²⁵ using beams loaded in flexure has shown that inelastic deformation occurs prior to failure in the high toughness Mg-PSZ. This has been attributed to transformation of tetragonal particles to monoclinic under the influence of the applied stress. Swain¹⁴ has noted discrepancies in strength-toughness relations similar to those discussed above, and has suggested that in such materials the strength is limited by the stress at which transformation occurs.

In the present study, factors that influence the strength of high-toughness Mg-PSZ are examined. In situ observations are used to identify mechanisms of failure and mechanisms of inelastic deformation. The observations are related to measurements of relative strengths of peak-toughened and overaged materials, strength degradation due to surface damage, variations of strength with stress state, and the influence of R-curve behavior on the strength.

II. EXPERIMENTAL PROCEDURE

A precipitated PSZ containing 9 mole % MgO[†] was chosen as the test material because of its high fracture toughness and the prior observation of nonlinear load deflection response in flexural testing.²⁵ The fabrication heat treatments and resultant microstructure of the material have been described in detail by Hannink²⁶ and Hannink Swain.²⁷ Simultaneous sintering

[†] Nilsen, MS grade ZrO₂.



SC5295.4FR

and heat treatment in the cubic phase field, followed by a controlled cooling schedule, yielded a microstructure comprising cubic ZrO_2 grains $\sim 50 \mu m$ diameter, which contained ellipsoidal tetragonal precipitates with largest dimension $\sim 150 \mu m$. There were also some monoclinic particles both within the grains and at grain boundaries. X-ray and Raman microprobe analysis indicated 12-14% monoclinic on polished surfaces and $\sim 30\%$ monoclinic on ground surfaces. The Raman microprobe analysis on polished surfaces did not detect any differences in monoclinic content at grain boundaries and grain interiors. Some specimens were given further heat treatment at $1450^\circ C$ in air for two days. This treatment caused transformation of all tetragonal particles to monoclinic without changing the grain size, and thus, provided a reference "overaged" material with similar microstructure to the "toughened" material, but without the transformation toughening.

Strengths, stress/strain relations and fracture toughnesses were measured by loading specimens in a variety of configurations using a universal testing machine.* Uniaxial tension was applied to flat "dogbone"-shaped specimens using a fixture described previously.²⁸ Strain gages attached to the test sections confirmed that bending stresses in these tests amounted to less than 5% of the uniaxial tension. Uniaxial flexure was applied in four-point bending with a fixture possessing all of the independent movements required to eliminate spurious stresses.²⁹ Beams with dimensions between $3 \times 2 \times 50$ mm and $6 \times 4 \times 50$ mm were tested with inner and outer loading spans of 12 and 45 mm. Biaxial flexure was applied by loading a truncated sphere on the specimen disc (2 mm thickness) that was supported on 3 balls placed symmetrically 12 mm from the loading axis. Fracture toughness was measured using constant-moment double-cantilever beams.

The influence of surface damage on strength was examined by comparing the uniaxial flexural strengths of polished surfaces, ground surfaces, and surfaces that had been indented with a Vickers pyramid at loads within the range

* Instron



10 to 1000 N. Each indented specimen contained 5 nominally identical, equally spaced indentations along a longitudinal line in the center of the tensile surface. All strength tests were done in an air environment at a stress rate of $40 \text{ MPa}\cdot\text{s}^{-1}$.

For in situ observations, specimens were loaded in tension and flexure by fixtures attached to the stage of an optical microscope. Most observations were made using Nomarski interference. Applied stresses in these experiments were calculated from strain measurements obtained from strain gages attached to the test pieces. The fixtures were also transferred to x-ray diffraction equipment for monitoring phase content during stressing.

III. RESULTS

(1) Strength and Toughness Measurements

The fracture toughnesses evaluated from constant moment double cantilever beam measurements were $12.5 \text{ MPa}\cdot\text{m}^{1/2}$ for the toughened material and $4 \text{ MPa}\cdot\text{m}^{1/2}$ for the overaged material. This large difference in toughness is reflected in the nature of the damage produced by Vickers indentation, as noted in other studies.³⁰ In the overaged material, well-defined, although generally somewhat irregular radial and lateral cracks were formed (Fig. 1(A)). Calculation of fracture toughness using measured radial crack dimensions and indentation fracture mechanics analysis³¹ yielded $K_{IC} = 3.9 \pm 0.4 \text{ MPa}\cdot\text{m}^{1/2}$, in agreement with the double cantilever measurement. In the toughened material well-defined cracks are not formed, but extensive transformation is evident around the indentation (Figs. 1(B) and 1(C)). The shape change associated with transformation causes surface distortion, which is made visible by Nomarski interference contrast. Therefore, the indentation cannot be used to evaluate fracture toughness. It is noted, however, that subsequent application of tension causes crack formation around the indentation, which can then serve as a strength-controlling flaw.



The results of flexural strength measurements for both toughened and overaged materials are shown in Fig. 2. The strengths are expressed as modulus of rupture (MOR), i.e., the apparent stress on the tensile surface, calculated from measured loads and specimen dimensions and standard beam bending formulae for linear elasticity. The decrease in strength of the overaged material with increasing indentation load is very similar to data published recently for other large grained ceramics such as alumina.²¹ The inclined broken line in Fig. 2 represents the predicted strength/load relation obtained from indentation fracture mechanics³² and the measured toughness, $K_{Ic} = 4 \text{ MPa}\cdot\text{m}^{1/2}$. In fine grained ceramics and glasses, strength/load data have been observed to follow the indentation fracture predictions over a wide range of loads.^{32,33} However, in large-grained materials a gradual transition in strength (similar to that exhibited by the data in Fig. 2) from the indentation fracture prediction at high loads to a microstructurally limited strength at low loads, has been observed.²¹

The MOR of the toughened material was relatively insensitive to stress state and surface preparation. The strengths of polished surfaces in uniaxial and biaxial flexure were similar and the strengths of polished and ground surfaces were not significantly different (in contrast to the results of other studies on transformation toughened materials which showed higher strengths for ground surfaces³⁴). More importantly, the strength loss with increasing indentation load is small. Consequently, the relative strengths of the toughened and overaged materials increased from a factor of 2 (600 MPa c.f. 300 MPa) for polished or ground surfaces to a factor of 4 for surfaces that had been indented at 500 N load (500 MPa c.f. 120 MPa).

The uniaxial tensile strengths were 400 MPa for the toughened material and 300 MPa for the overaged material. The tensile strength and MOR are therefore identical for the overaged material, but in the toughened material the MOR is 50% higher than the tensile strength. This apparent discrepancy is attributed to the nonlinear stress strain response of the toughened material in the following sections.



(2) Stress-Strain Measurements

Stress-strain measurements for uniaxial tension were obtained for both materials. The stresses were calculated from measured loads and cross-sectional areas, and the strains were obtained from gages attached to the central test sections. For the overaged material, the stress-strain response was linear to failure, with a Young's Modulus of 205 GPa. In contrast, the toughened material exhibited extensive nonlinear deformation prior to failure, as shown in Fig. 3. Stress-strain curves obtained from six strain gages in this material (two test specimens, 3 gages on each specimen) varied by no more than 5% from the curve in Fig. 3. At strains lower than $\sim 10^{-3}$, the stress-strain response is linear with a Young's modulus of 208 GPa, but at higher strains an increasing nonlinear component is evident. The unload/reload curves in Fig. 3, which are linear with modulus close to that of the unloaded material, indicate that the nonlinear deformation is mostly irreversible.

Measurements from four-point flexural tests in the toughened material are shown in Fig. 4(A). In this case, an apparent flexural stress, σ_B , obtained from standard beam bending formulae for linear elasticity, is plotted against the strains obtained from gages attached to the tensile and compressive surfaces. Nonlinear, irreversible deformations are again evident at strains larger than $\sim 10^{-3}$. The nonlinear behavior was also evident in plots of apparent flexural stress versus deflection of the loading points. Similar response was observed in biaxial flexure tests (Fig. 4(B)).

(3) In-Situ Observations; Optical

Optical micrographs of the polished tensile surface of a beam of toughened material during loading in uniaxial flexure are shown in Fig. 5. At strains larger than $\sim 10^{-3}$, surface distortions with periodicity equal to the grain size ($\sim 50 \mu\text{m}$) are evident from the shadowing effect of the Nomarski interference (Fig. 5(B)). Surface rumpling has been observed previously after uniaxial compression testing at very high loads³⁵ ($> 1200 \text{ MPa}$) and in regions



surrounding indentations³⁰ (Fig. 1(C)). This rumpling was attributed to shape changes associated with tetragonal-to-monoclinic transformation.

The surface distortions shown in Fig. 5(B) differ in several respects from the previous observations. First, the magnitude of the rumpling is smaller in Fig. 5(B) than in the previously reported observations from compression³⁵ and indentation³⁰ tests. More careful examination of very high load indentations ($> 50 K_g$, Fig. 1) reveals that two distinct zones of surface rumpling exist; an inner zone with displacements similar in magnitude to those observed in the compression tests, and an outer zone with smaller displacements similar to those in Fig. 5(B). The two types of rumpling are also distinguished by the existence of well-defined parallel-sided bands traversing most individual grains in both the compression experiments and the inner indentation zone, but not in the outer indentation zone or the tensile surface. However, the most important difference is that the rumpling in Fig. 5(B) is reversible when the applied load is removed, as shown in Fig. 6. The compression test observations were made after load removal and thus represent irreversible transformation, whereas the indentation observations were made under load (residual stress).

With further loading, the surface rumpling gradually became more severe and, at strains $\sim 1.8 \times 10^{-3}$, microcracks with dimensions similar to the grain size initiated (Fig. 5(C)). The microcracks were readily visible using Nomarski interference because of the surface uplift caused by zones of transformed material surrounding the cracks.³⁶ Continued loading caused stable growth of the microcracks (and microcrack coalescence) followed by rapid fracture from the dominant microcrack. Measurements of crack size as a function of applied load are discussed in Sect. IV (4).

Observations from specimens loaded in biaxial flexure and uniaxial tension were similar to those in Fig. 5. The only significant difference noted was the existence of larger distortions in the surface rumpling effect in the biaxial flexure experiment. In similar experiments using the overaged material surface rumpling effects were not observed.



(4) In Situ Observations: X-Ray

In situ x-ray measurements were used to confirm that the surface rumpling was caused by the tetragonal to monoclinic transformation. In these experiments beams were loaded in 4-point bending on the stage of x-ray diffraction equipment, with the load being monitored by strain gages between the loading points on the compressive surfaces. With the load held at each selected level, the (111) and (11 $\bar{1}$) peaks of monoclinic, cubic, and tetragonal were scanned, using Cu radiation and a liquid-nitrogen-cooled EDAX detector. Counting times were ~ 6 h. The monoclinic content was then computed from relative peak intensity measurements using the relation.³⁷

$$X = [I(111_m) + I(11\bar{1}_m)]/[I(111_m) + I(11\bar{1}_m) + I(111_t)] \quad (1)$$

where X is the fraction of monoclinic phase and $I(111)$ is the diffracted intensity from the (111) planes, with the subscripts m and t referring to monoclinic and cubic/tetragonal. The peak intensities were derived from area measurements which were obtained by first subtracting the background then curve fitting using Pearson VII functions.³⁸ The results are summarized in Fig. 7. The monoclinic content increased with increasing applied tension (Fig. 7(A)), from 13.5% of the total volume at zero load, to 19.5% just prior to failure. The effect of load removal on the monoclinic content is illustrated in Fig. 7(B). The results in this figure clearly indicate reversibility in the transformation, with about half of the particles that were transformed by the applied stress reverting to tetragonal on removal of the stress.

IV. DISCUSSION

(1) Stress-Strain Relations

The existence of nonlinear tensile stress-strain response in the toughened PSZ invalidates the use of modulus of rupture as a measure of fail-



ure stress in bending. Calculations of the true stresses in flexural loading are given in the Appendix. These calculations are based on the measured tensile stress-strain curve in Fig. 3 and a linear response in compression (which has been demonstrated in other work for stresses smaller than ~ 1200 MPa³⁵). The results (Fig. A3) indicate that the true failure stress in flexure is lower, by up to 40%, than the modulus of rupture. From Fig. A3 and the data in Fig. 2, the true failure stress in flexure is obtained as 400 MPa for undamaged surfaces. This is indistinguishable from the strength in uniaxial tension.

The calculations in the Appendix can also be used to predict the relations between the apparent flexural stress in bending and the strains on the tensile and compressive surfaces, from the measured response in uniaxial loading. The results of such predictions are compared with measured values (Fig. 4(A)) in Fig. 8. The close agreement evident in Fig. 8 between predictions and experimental measurements substantiates the calculated stress corrections discussed above.

(2) Deformation Mechanisms

The in situ x-ray and optical observations indicate that both transformation and microcracking are associated with the nonlinear, nonelastic deformation of the toughened material at tensile stresses above ~ 250 MPa (Fig. 3). Both processes have also been identified in uniaxial compression testing,³⁵ but at considerably higher stress magnitudes.

Correlation between the measured strains and the measured transformation volumes and microcrack densities is complicated by several factors. Some of these are the unknown twinning or martensite variant state of the transformed particles, possible preferred orientations of transformed particles relative to the applied stress, and the occurrence of transformation in conjunction with microcracking (the strain contributions from the transformation and the microcracks are then not separately additive). Nevertheless, a rough estimate is instructive. The x-ray measurements indicate that the



stress-induced transformation prior to failure amounts to ~ 6% (of the total volume), of which ~ 3% is reversible (Fig. 7). It is hypothesized that the reversible component causes the reversible surface rumpling (Fig. 6) and the irreversible component occurs in conjunction with microcracking and causes the irreversible surface uplift around the cracks (Fig. 5). The macroscopic linear strain due to the dilation component of the transformation strain is given by

$$\epsilon_d = f \epsilon^T / 3 \quad (2)$$

where f is the volume fraction of transformed particles and ϵ^T is the unconstrained transformation strain (dilatational component). With $\epsilon^T = 0.04$ and $f = 0.06$, Eq. (2) gives $\epsilon_d = 8 \times 10^{-4}$. Transmission electron microscopy observations³⁹ have shown that the permanently transformed monoclinic particles surrounding cracks in these materials are twinned, so that long range shear strains resulting from the shear component of the transformation are eliminated. However, it is conceivable that the particles that transform reversibly may not form twins, or that the twinning does not completely eliminate the long-range shear stresses (especially for particles oriented favorably relative to the applied stress). In that case, an additional strain component will result. For particles oriented with the transformation shear direction at 45° to the uniaxial stress, the contribution to the measured elongation strain is

$$\epsilon_s = f \gamma^T / 2 \quad (3)$$

where γ^T is the unconstrained transformation shear strain. For randomly oriented particles, $\epsilon_s = 0$. With $f = 0.03$ and $\gamma^T = 0.14$, the additional strain is between zero and 10×10^{-4} . Therefore, the total strain available from the measured transformation volume is between 8×10^{-4} and 18×10^{-4} . This is sufficient to account for the measured nonlinear strain component at



failure (15×10^{-4} , Fig. 3). The additional strain due to microcracking is not estimated here because of the above mentioned difficulty.

Calculated and observed strains after unloading do not agree. The stress strain measurements indicate that the recoverable portion of the non-linear strain component is less than 1×10^{-4} . However, the observed transformation of 3% of the volume from monoclinic to tetragonal implies a minimum strain recovery of 4×10^{-4} . Moreover, additional strain recovery from the microcracks should be observed. The reasons for this discrepancy are not clear, but one possibility is that the fraction of particles that transform reversibly is larger near the surface than in the bulk.

The magnitude of the surface deflections associated with the reversible rumpling can be correlated with the measured volumes of reversible transformation and the resultant strains. The general appearance of the rumpling, with adjacent grains being uniformly uplifted or depressed relative to each other, suggests that the rumpling is caused by unequal transformation volumes within adjacent grains, but uniform distributions within each grain. Variations of $\sim 3\%$ in the transformed volumes of adjacent grains would give differences in transformation strains $\sim 4 \times 10^{-4}$, which, for a grain size $\sim 50 \mu\text{m}$, yields relative surface displacements $\sim 20 \text{ nm}$. This is within the range of surface deflections detected by Nomarski interference, and thus, further substantiates the correspondence between the surface uplift and the reversible transformation.

(3) Strength-Toughness Relations

A meaningful comparison of the flexural strengths of toughened and overaged materials (Fig. 2) requires calculation of the true failure stresses in the toughened material, rather than modulus of rupture (Sect. IV(1)). Failure stresses computed from the data in Fig. 2 for uniaxial flexure and the analysis of the Appendix are shown in Fig. 9. As indicated previously, correction of the apparent flexural strength to a true failure stress yields a strength in flexure equal to the measured strength in uniaxial tension.



Moreover, since the magnitude of the correction increases with increasing strength, the effect on the data in Fig. 2 is to reduce the higher apparent strengths (i.e., nonindented surfaces and low indentation loads) more than lower strengths (i.e., high load indentations). With this correction the true failure stress shows almost no degradation at indentation loads up to 1000 N. Thus, the tensile strength of this material is insensitive to surface damage.

The reduction of the failure stress of the undamaged toughened material from the apparent value ~ 600 MPa to the true stress ~ 400 MPa enlarges the discrepancies discussed earlier between the observed strength toughness and strength flaw-size relations and the expectations of conventional theories of strength of brittle materials. The strength of the nonindented, toughened material is only a factor of $4/3$ larger than that of the overaged material, whereas the fracture toughness is a factor of 3 larger. However, the strength difference at high indentation loads increases to a factor of 4 and is thus more consistent with the relative fracture toughnesses.³² This variation can be interpreted in terms of R-curve behavior, as discussed in the following section.

(4) Crack Growth Resistance

In situ observations, such as those shown in Fig. 5, indicate that failure of toughened PSZ is preceded by stable development of the strength-controlling flaw with increasing applied stress. This response is characteristic of a system in which the resistance to crack growth is defined by an R-curve which increases with crack extension, rather than by a unique fracture toughness.

An approximate ^{*}R-curve was constructed from observations such as those in Fig. 5, by identifying the crack that eventually caused failure and calculating the applied stress intensity factor at each stage during its precursor stable growth. Assuming that the crack maintains a half-penny shape oriented normal to the surface, the stress intensity factor is given by¹⁶



$$K_a = 2\sigma_a(c/\pi)^{1/2} \quad (4)$$

where σ_a is the applied stress and c is the crack radius. Equation (4) is plotted in Fig. 10 for two values of σ_a ; the lower value ($\sigma_a = 365$ MPa) represents the stress at which the dominant crack in Fig. 5(D) first initiated and the larger value represents the failure stress. The data in Fig. 10 represent the critical stress intensity factors, $K_a = K_R$, required to extend the crack at intermediate loading stages, obtained by inserting the measured crack lengths and applied stresses into Eq. (4). The solid curve thus represents the approximate* form of the R-curve, fitted to the data subject to the requirements that the limiting toughness obtained from double cantilever beam measurements be approached at large crack lengths and that the R-curve be tangent to the plot of $K_a(c)$ at the failure condition.

V. IMPLICATIONS

The existence of an R-curve of the form indicated in Fig. 10 has important implications for strength and toughness relations in transformation-toughened materials. The strength is defined by the stress at which the R-curve and the applied stress intensity factor curve are tangent at their intersection. Consequently, cracks smaller than the corresponding crack length, c^* , grow stably before failure and the strength is insensitive to pre-existing defects (for defects smaller than c^*). Insensitivity of strength to pre-existing flaws is confirmed by the data in Fig. 9. These results demon-

* The curve in Fig. 5 is approximate for two reasons. One is that the assumed half-penny crack shape was not confirmed by depth measurements. The other is that the test was run in atmospheric environment in which ZrO_2 is known to exhibit some slow crack growth.⁴⁰ However, the effects of subcritical crack growth are small. The load in this test was held constant for several minutes at each measurement point and increased at a constant rate between measurements. Significant crack extension was not observed during any of the measurement periods except the final one, during which spontaneous failure occurred.



strate that the material exhibits desirable damage tolerant strength characteristics, but that the strength cannot be improved by processing changes or microstructural changes that reduce pre-existing flaw sizes without altering the R-curve.

Strength improvement requires the steepness of the R-curve to be increased. Increasing the steepness without changing the limiting toughness, K_C , increases the strength, but also decreases the damage tolerance (i.e., decreases c^*). Therefore, optimum changes would involve increasing both the steepness and K_C . It is also noted that transitions from R-curve controlled strength to flaw size controlled strength are possible, as illustrated in Fig. 11. For the pre-existing flaw size shown and $K_C < K_0$, failure occurs without precursor growth and the strength is controlled by flaw size and toughness. The fine-grained $Al_2O_3-ZrO_2$ and polycrystalline tetragonal materials appear to follow this behavior because their strengths can be dramatically improved by control of processing to eliminate flaws. For the upper R-curve in Fig. 11, the strength is dictated by the R-curve and failure is preceded by stable growth of the pre-existing flaw to the length c^* . The R-curve response for long cracks can be predicted from fracture mechanics analyses.^{22,23} The present results indicate a need for similar analysis of R-curve development for small cracks.

Finally, it is noted that, in the region of R-curve controlled strength, statistical theories of strength (strength-size effects, etc.), that are usually applied to brittle materials, do not apply, for these theories are based on the premise that strength is dictated by a pre-existing flaw population. Instead, the strength appears to be deterministic and thus insensitive to specimen size. Existing theories of delayed failure and proof testing also need to be reevaluated for these materials.



APPENDIX: FLEXURAL STRESSES AND STRAINS

A method for evaluating stresses and strains in beams loaded in flexure was described by Nadai.⁴¹ For the present analysis, a stress strain curve of the form shown in Fig. A1 is assumed:

$$\frac{\sigma}{\sigma_y} = \begin{cases} e & e < 1 \\ 1 + \alpha(e - 1) & e > 1 \end{cases} \quad (A1)$$

where e denotes the normalized strain, ϵ/ϵ_y . The measured curve in Fig. 3 is represented approximately by Eq. (A1) with $\epsilon_y = 0.00175$, $\sigma_y = 370$ MPa, and $\alpha = 0.15$. With the usual assumption that plane sections remain plane, the strain at a distance y from the neutral axis is given by

$$\epsilon = y/r \quad (A2)$$

where r is the radius of curvature. Thus, the strains at the tensile and compressive surfaces can be written

$$\epsilon_T = y_T/r \quad (A3)$$

$$\epsilon_C = y_C/r \quad (A4)$$

where y_T and y_C define the distance of the neutral axis from the tensile and compressive surfaces.



Relations between the applied loads and the stresses and strains are obtained from equations of equilibrium for the beam. The requirements that the sum of the normal forces at any cross section be zero and that the moment of those forces be equal to the applied bending moment lead to

$$r \epsilon_y \int_{-e_c}^{e_T} \sigma de = 0 \quad (A5)$$

and

$$M = br^2 \epsilon_y^2 \int_{-e_c}^{e_T} \sigma e de \quad (A6)$$

Solution of Eqs. (A1) and (A5) provides a relation between the strains on the tensile and compressive surfaces;

$$e_c^2 = \alpha e_T^2 + (1 - \alpha)(2 e_T - 1) \quad (A7)$$

The relative strains ϵ_c/ϵ_T obtained from Eq. (A7) are plotted as a function of e_T for various values of α in Fig. A2.

The apparent flexural stress, σ_B , obtained by assuming a linear elastic beam with rectangular cross section of width b and thickness d , is

$$\sigma_B = 6M/bd^2 \quad (A8)$$



Setting $d = y_T + y_C$, Eqs. (A3) and (A4) give

$$d = r \epsilon_y (e_T + e_C) \quad (A9)$$

Then, the ratio of the apparent flexural stress, σ_B , to the stress, σ_T , on the tensile surface can be expressed (from Eqs. (A1), (A6), (A8), and (A9)) as

$$\sigma_B/\sigma_T = 2 \frac{[e_C^3 + \alpha e_T^3 + (1-\alpha)(3 e_T^2 - 1)/2]}{(e_T + e_C)^2 [\alpha e_T + (1 - \alpha)]} \quad (A10)$$

Using Eqs. (A7) and (A10), this ratio is plotted as a function of e_T for various values of α in Fig. A3. It is noted that for the stress strain curve of Fig. 3, the ratio σ_B/σ_T at failure ($\alpha = 0.15$ and $e_T = 2$) is 1.4.

REFERENCES

1. R.C. Garvie, R.J.H. Hannink, and C. Urbani, *Ceramurg. Int.* 6, 19-24 (1980).
2. D.L. Porter and A.H. Heuer, *J. Am. Ceram. Soc.* 60, 183-84 (1977).
3. F.F. Lange, *J. Mat. Sci.* 17, 255 (1982).
4. F.F. Lange, *J. Mat. Sci.* 17, 247-54 (1982).
5. N. Claussen and M. Ruhle, *Advances in Ceramics, Am. Ceram. Soc.* 3, 137-63 (1981).



6. M.V. Swain, R.H. Hannink, and R.C. Garvie, *Fracture Mechanics of Ceramics*, Plenum, 6, 339-354 (1983).
7. R.J.H. Hannink, *J. Mat. Sci.* 13, 2487-96 (1978).
8. R.J.H. Hannink, K.A. Johnston, R.T. Pascoe, and R.C. Garvie, *Advances in Ceramics* 3, 116-137 (1981).
9. M.V. Swain and R.J.H. Hannink, *Advances in Ceramics* 12 (1984).
10. K. Kobayashi, H. Kuwajimi and T. Misaki, *Sol. State Ionics* 3/4, 489 (1981).
11. K. Tsukuma, Y. Kubota and T. Tsukidate, *Advances of Ceramics* 12 (1984).
12. K. Tsukuma and M. Shimada, *Amer. Ceram. Soc. Bull.* 64[2], 310-313 (1985).
13. M. Marmach and M.V. Swain, *J. Aust. Ceram. Soc.*, in press.
14. M.V. Swain, *Acta. Met.*, in press.
15. K. Tsukuma, Y. Kubota and T. Tsukidate, *J. Am. Ceram. Soc.*, in press.
16. B.R. Lawn and T.R. Wilshaw, *Fracture of Brittle Solids*, Cambridge University Press, Lond. (1975).
17. A.V. Virkar, D.K. Shetty and A.G. Evans, *J. Am. Ceram. Soc.* 64[6] 3450-49 (1981).
18. A.G. Evans, *J. Am. Ceram. Soc.* 63[1-2], 115-116 (1980).



19. R.W. Rice, S.W. Freiman and P.F. Becher, J. Am. Ceram. Soc. 64[67], 345-49 (1981).
20. R.W. Rice and S.W. Freiman, J. Am. Ceram. Soc. 64[6], 350-54 (1981).
21. R.F. Cook, B.R. Lawn and C.J. Fairbanks, J. Am. Ceram. Soc., in press.
22. D.B. Marshall, M. Drory, and A.G. Evans, Fracture Mechanics of Ceramics, Plenum, 6, 289-307 (1983).
23. R.M. McMeeking and A.G. Evans, J. Am. Ceram. Soc. 65, 242-46 (1982).
24. M.V. Swain, Fracture Mechanics of Ceramics, Plenum, 6, 355-369 (1983).
25. D.C. Larsen, IIT Research Institute Tech. Report No. 11, 1981.
26. R.H.J. Hannink, J. Mat. Sci. 18, 457-70 (1983).
27. R.H.J. Hannink and M.V. Swain, J. Aust. Ceram. Soc. 18, 53-62 (1982).
28. D.B. Marshall and A.G. Evans, J. Am. Ceram. Soc., in press.
29. R.G. Hoagland, C.W. Marschall and W.H. Duckworth, J. Am. Ceram. Soc. 59 [5-6] 189-192 (1976).
30. R.H.J. Hannink and M.V. Swain, J. Mater. Sci. 16, 1428 (1981).
31. G.R. Anstis, P. Chantikul, B.R. Lawn and D.B. Marshall, J. Amer. Ceram. Soc. 64[9], 533-43 (1981).
32. P. Chantikul, G.R. Anstis, B.R. Lawn and D.B. Marshall, J. Am. Ceram Soc. 64[9], 539-543 (1981).



33. D.B. Marshall, J. Am. Ceram. Soc. 66[2], 127-131 (1983).
34. M.V. Swain, J. Mat. Sci. Lett. 15, 1577-79 (1980).
35. J. Lankford, J. Am. Ceram. Soc. 66, C-212 (1983).
36. M.V. Swain, J. Am. Ceram. Soc., in press.
37. R.C. Garvie, R.H.J. Hannink and M.V. Swain, J. Mat. Sci. Lett. 1, 437-440 (1982).
38. S.V. Naider and C.R. Hausku, J. Appl. Cryst. 15, 190-98 (1982).
39. L.H. Schoenlein and A.H. Heuer, Fracture Mechanics of Ceramics, Plenum, 6, 309-326 (1983).
40. L. Li and R.F. Pabst, Fracture and Fatigue, ECF3, Permogon, NY, 251-55 (1980).
41. A. Nadi, Theory of Flaw and Fracture of Solids, McGraw Hill, NY (1950).

AD-A159 178

STRENGTHENING AND STRENGTH UNIFORMITY OF STRUCTURAL
CERAMICS(U) ROCKWELL INTERNATIONAL THOUSAND OAKS CA
SCIENCE CENTER F F LANGE ET AL APR 85 SC5295 4FR
AFOSR-TR-85-0731 F49620-81-C-0036

2/2

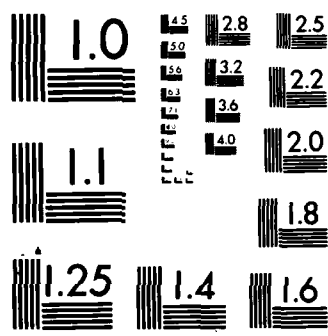
UNCLASSIFIED

F/G 11/2

NL



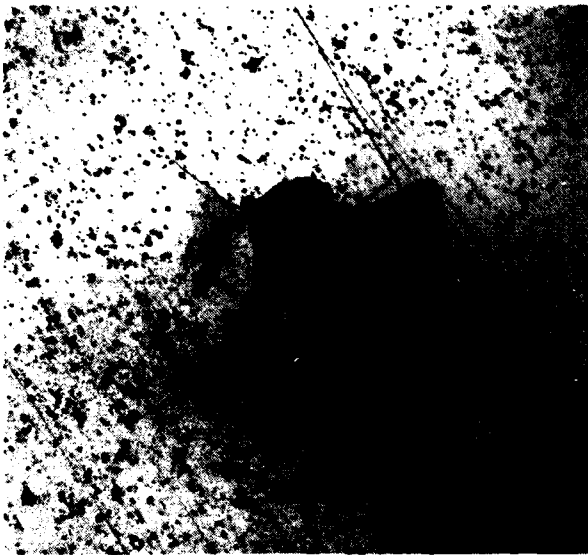
END
FILMED
DHC



MICROCOPY RESOLUTION TEST CHART
NATIONAL BUREAU OF STANDARDS-1963-A



SC85-31239



(A)



(B)



(C)

Fig. 1 (A) Vickers indentation in overaged Mg-PSZ, 200 N load. Width of field 900 μm . (B) and (C) Vickers indentation in toughened Mg-PSZ, 500 N load. Width of field in (B) is 2.2 mm and in (C) is 600 μm .



SC85-30787

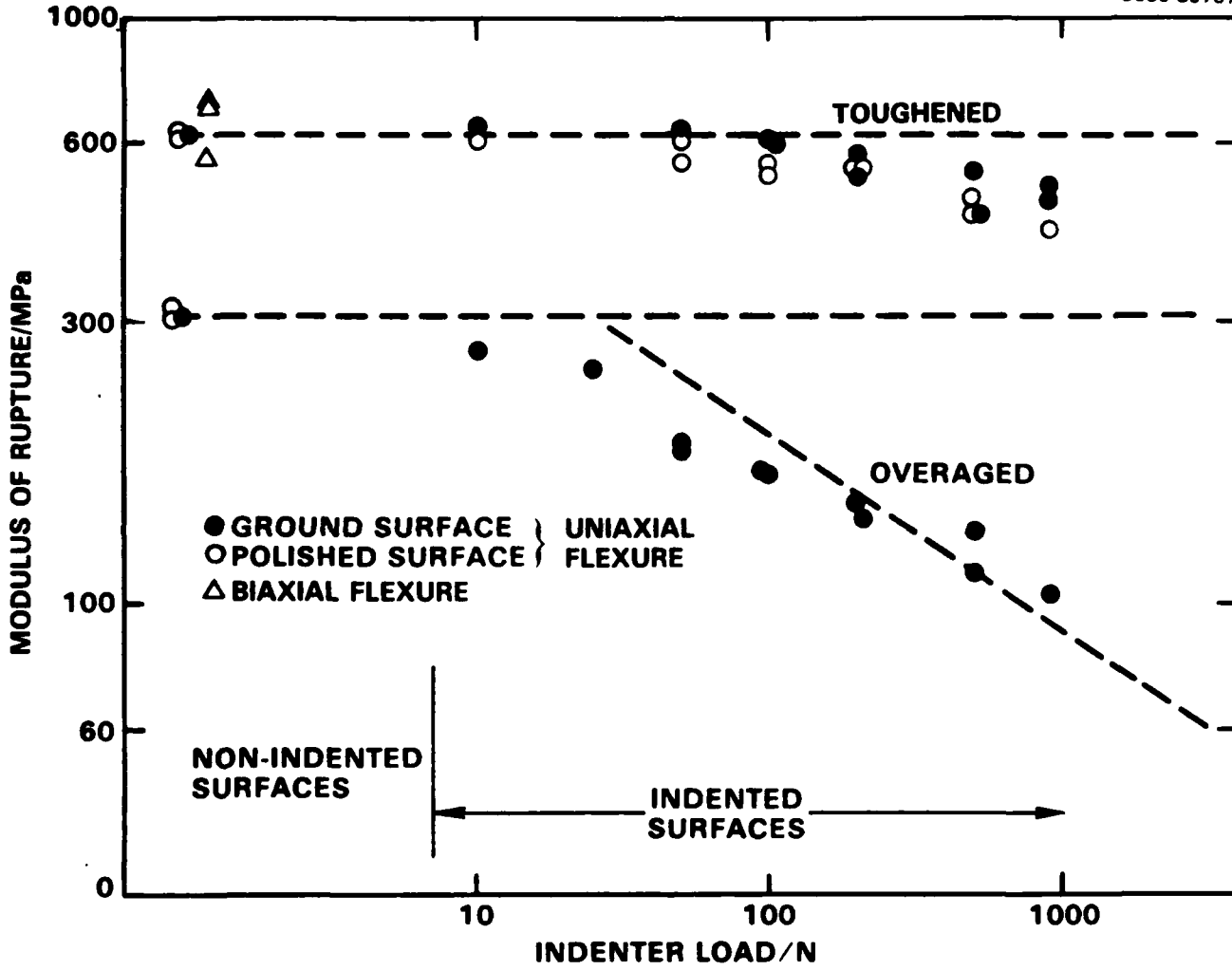


Fig. 2 Variations of modulus of rupture of toughened and overaged Mg-PSZ, measured in flexure, as a function of surface damage introduced by Vickers Indentation.

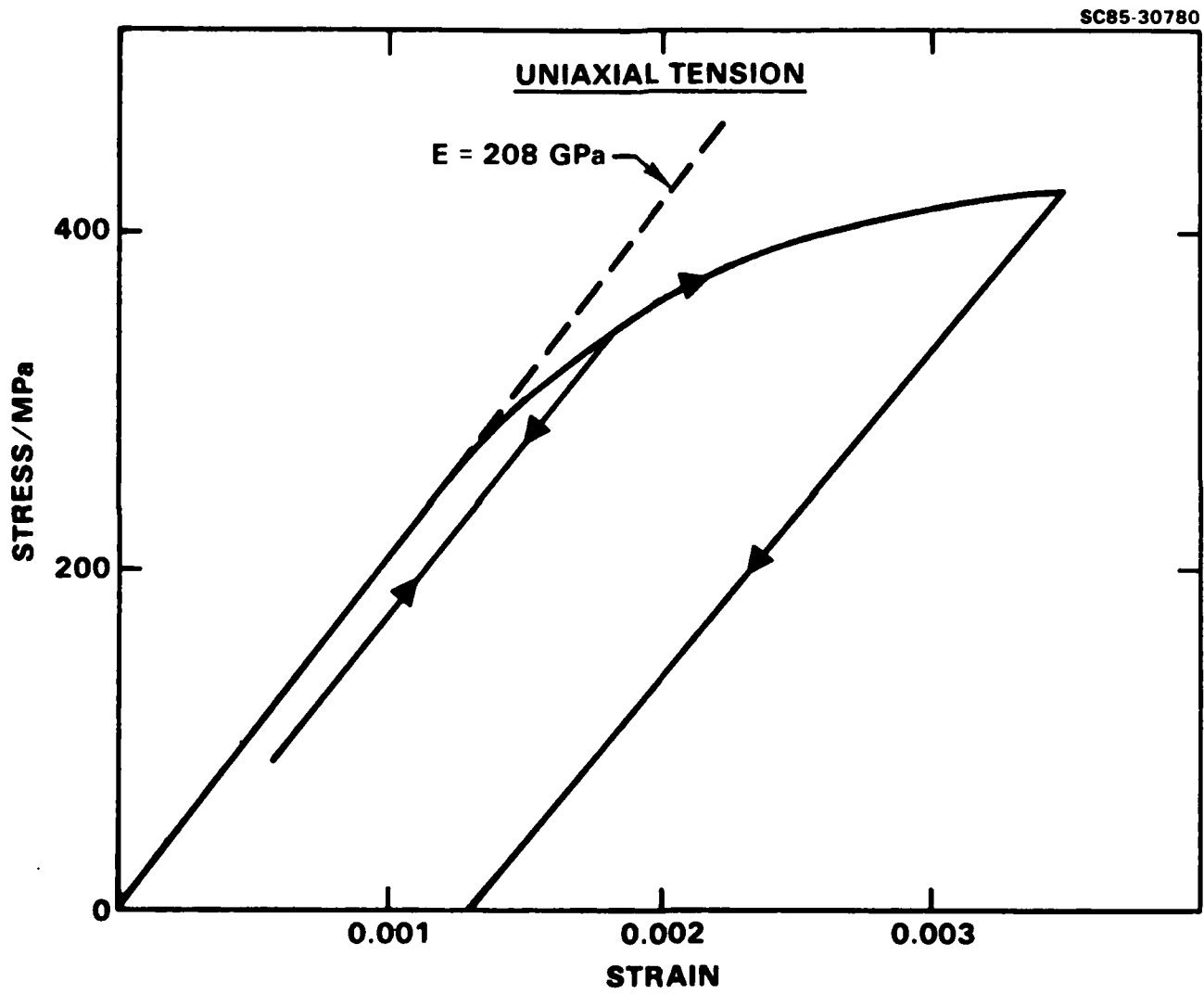


Fig. 3 Stress-strain curve of toughened Mg-PSZ in uniaxial loading.



SC5295.4FR

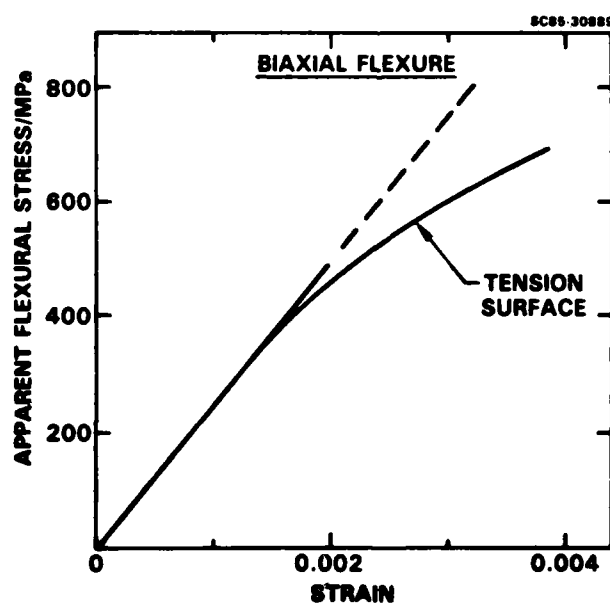
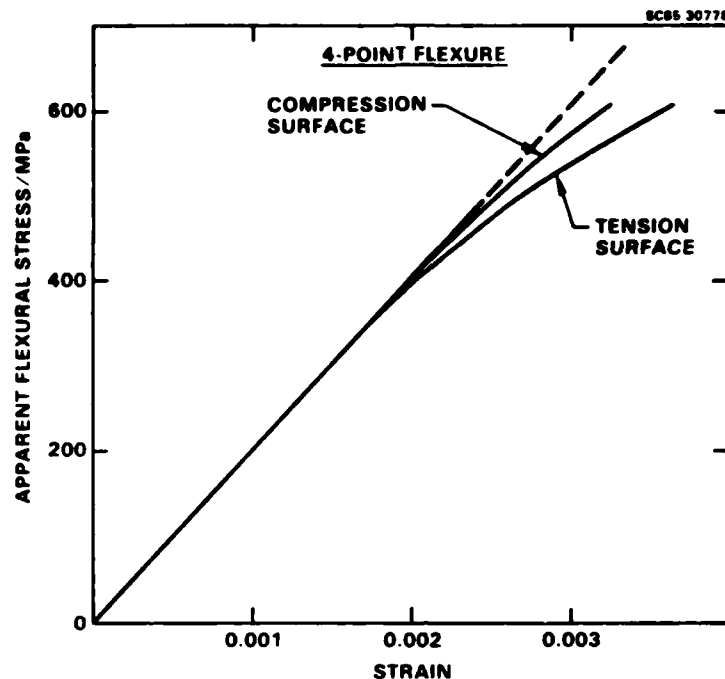
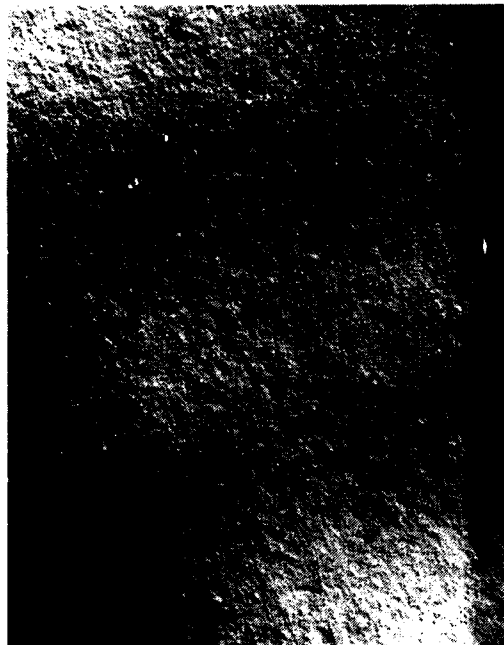


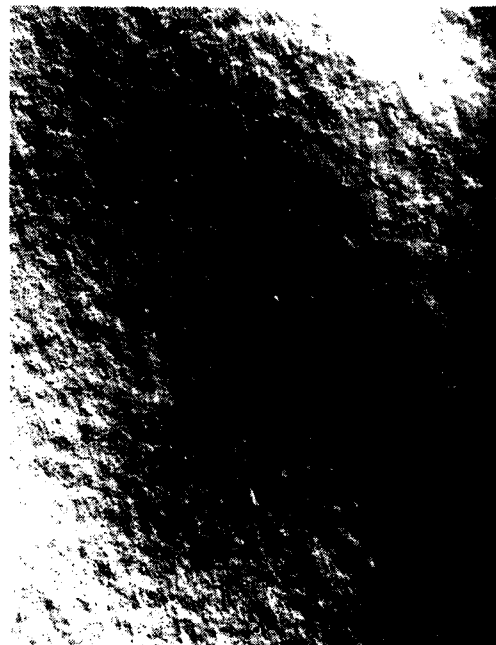
Fig. 4 Apparent flexural stress-strain curves for toughened Mg-PSZ: (A) four-point bending, (B) biaxial loading.



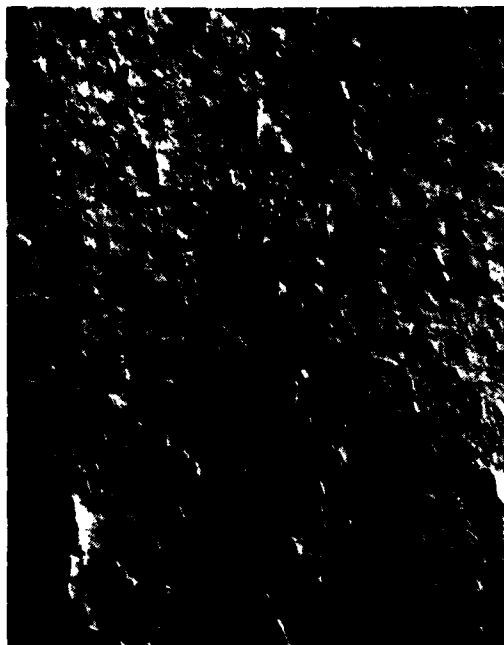
SC84-29656



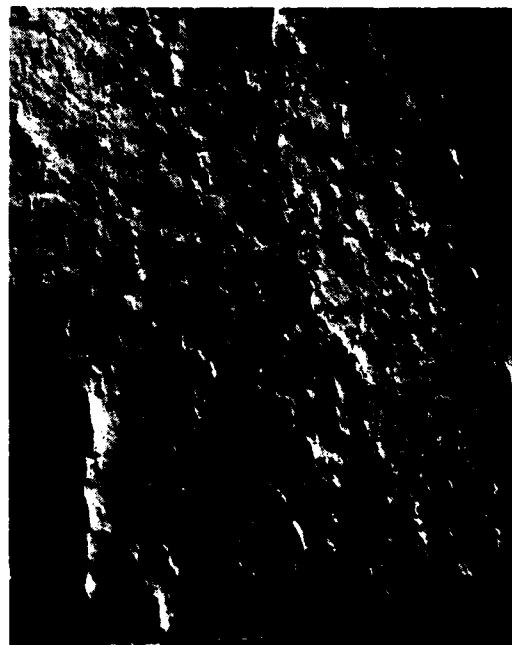
(A)



(B)



(C)



(D)

Fig. 5 Optical observations of tensile surface of flexure beam of toughened Mg-PSZ during loading. Nomarski interference used to highlight surface distortions. Stresses obtained from strain gage measurements: (A) $\sigma = 0$, (B) $\sigma = 360$ MPa, (C) $\sigma = 418$ MPa, and (D) $\sigma = 420$ MPa. Width of field 1.9 mm.



SC84-29657



(A)



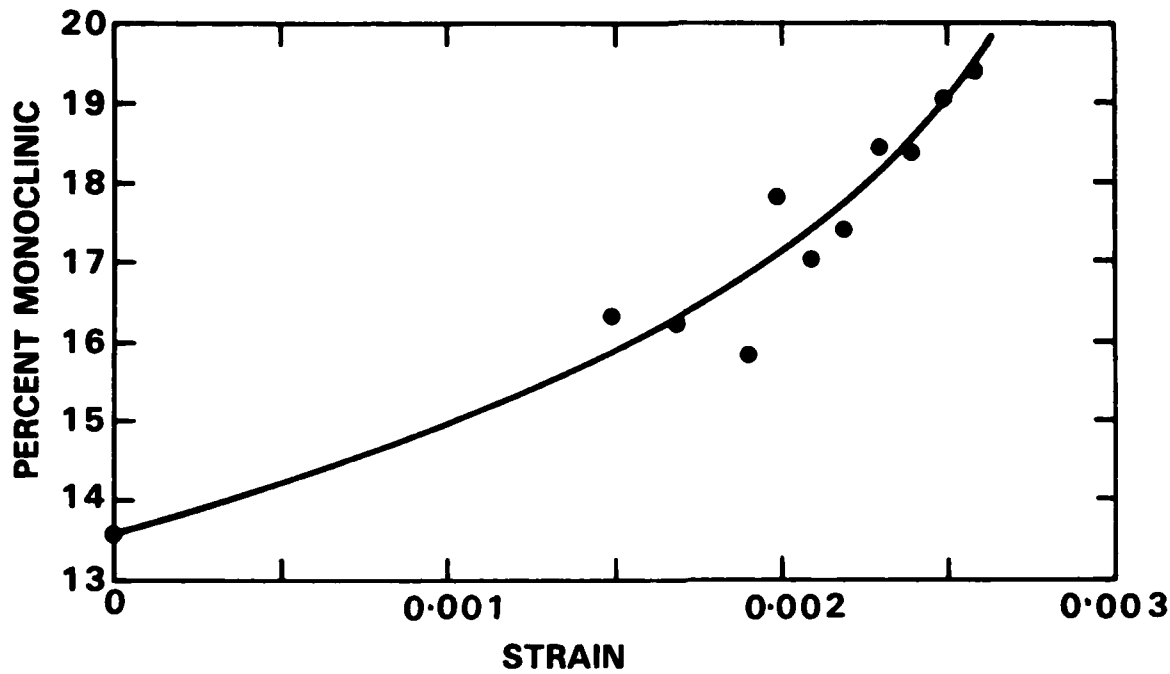
(B)

Fig. 6 Optical observations of tensile surface of flexure beam of toughened Mg-PSZ during load cycling. (A) $\sigma = 360$ MPa and (B) stress reduced to $\sigma = 80$ MPa. Width of field 1.9 mm.



SC5295.4FR

SC85-30805



SC85-30788

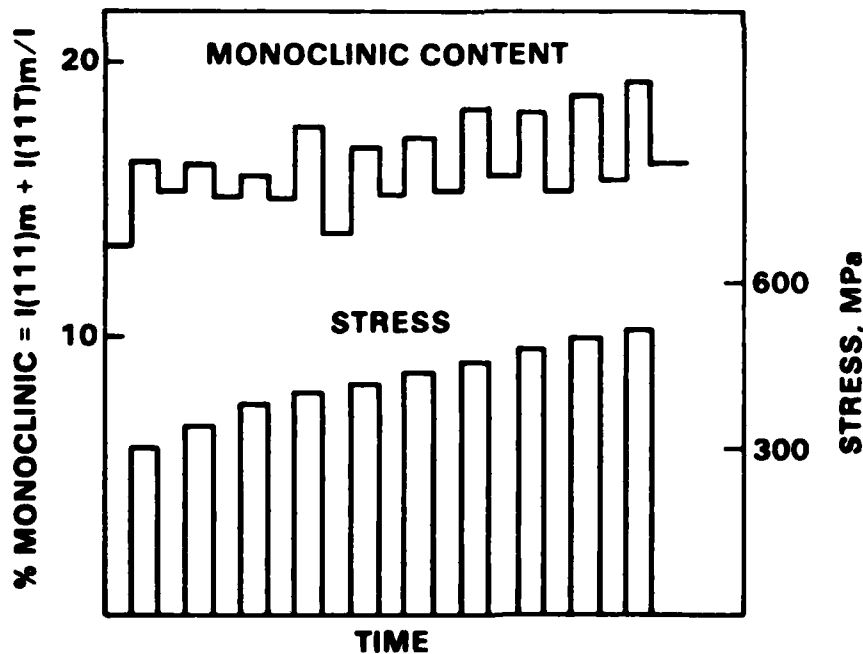


Fig. 7 X-ray measurements of the volume fraction of monoclinic ZrO_2 in toughened Mg-PSZ during flexural loading. (A) Variation of monoclinic content in the tensile surface with strain measured by gage on compressive surface. (B) Variation of monoclinic content at tensile surface during load cycling.



SC5295.4FR

SC85-30785

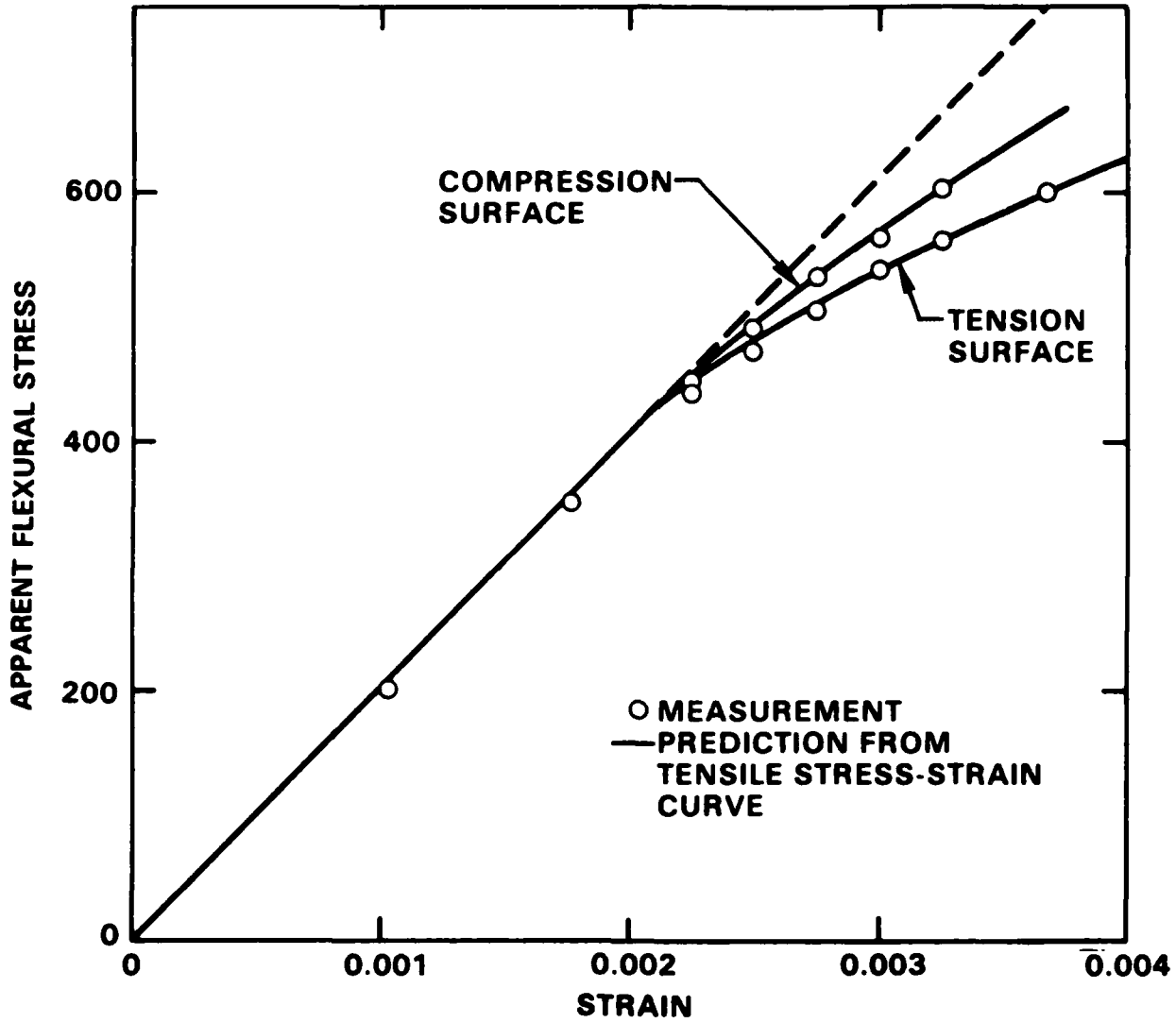


Fig. 8 Comparison of measured and predicted apparent flexural stress-strain curves for toughened Mg-PSZ.

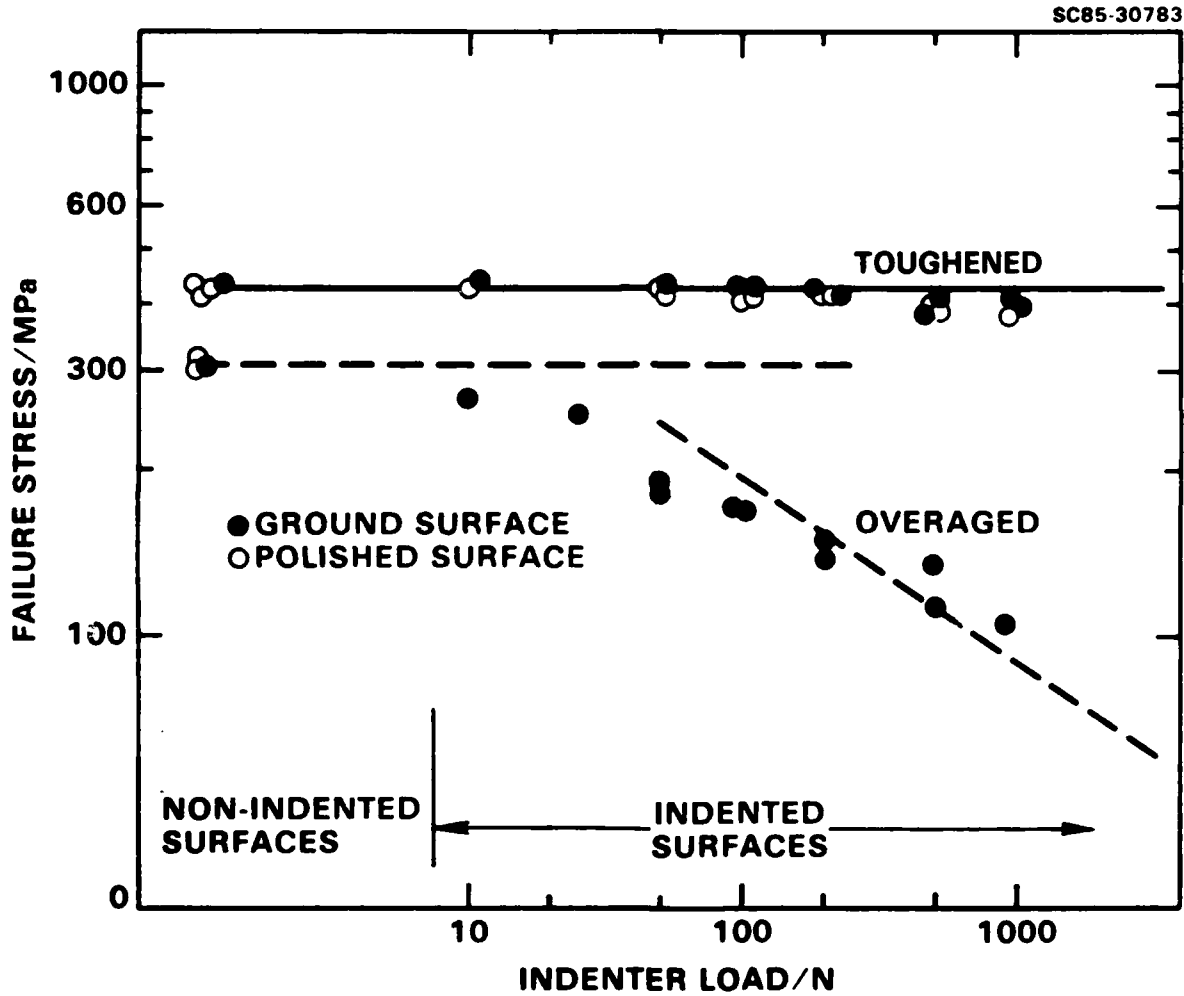


Fig. 9 Variation of failure stress of toughened and overaged Mg-PSZ as a function of surface damage introduced by Vickers indentation. Data from Fig. 2, with apparent flexural stresses corrected to true values using the analysis in the Appendix.

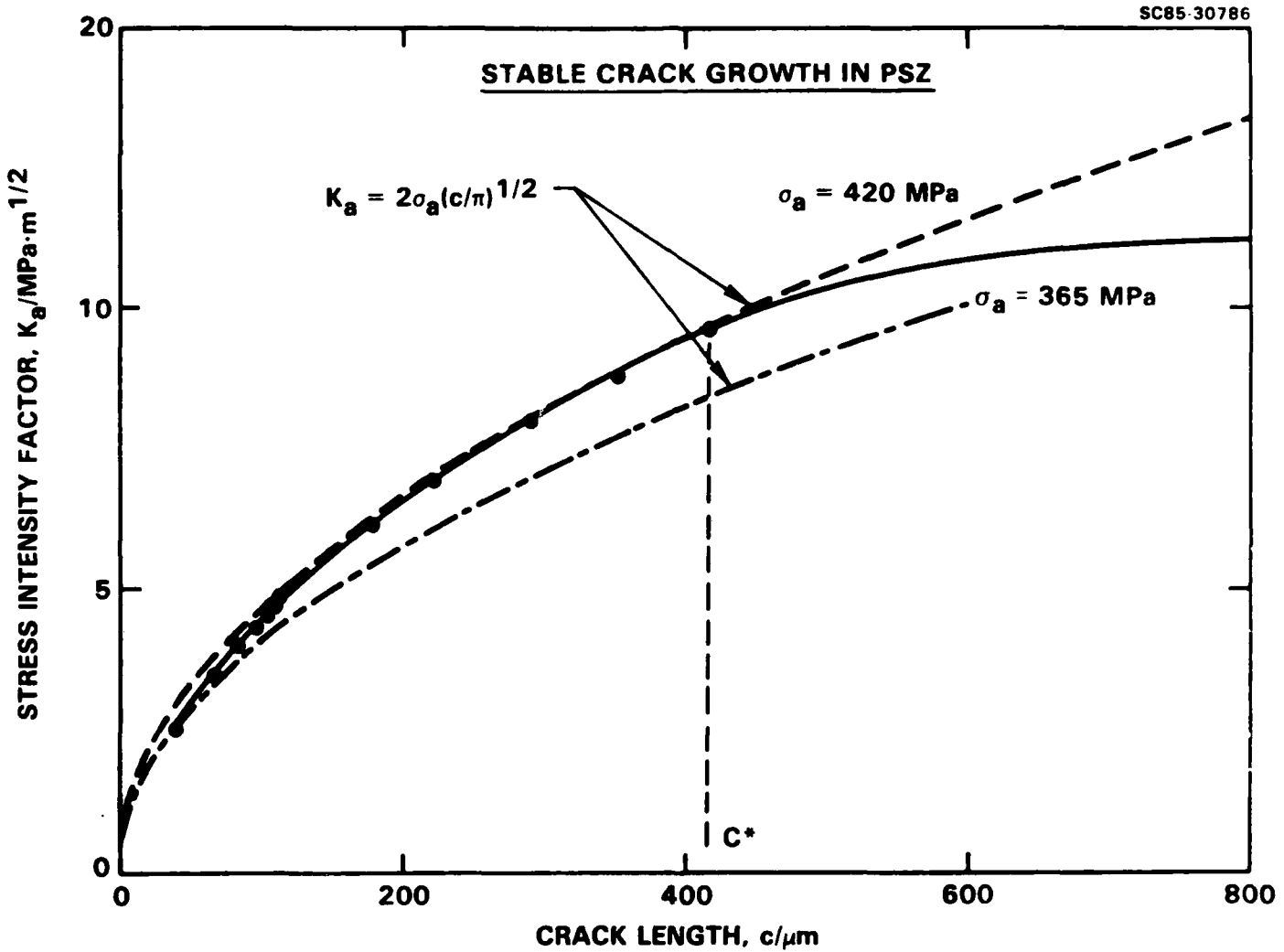


Fig. 10 Variation of stress intensity factor and stable crack growth during loading of toughened Mg-PSZ. Data obtained from the crack shown in Fig. 5(D).

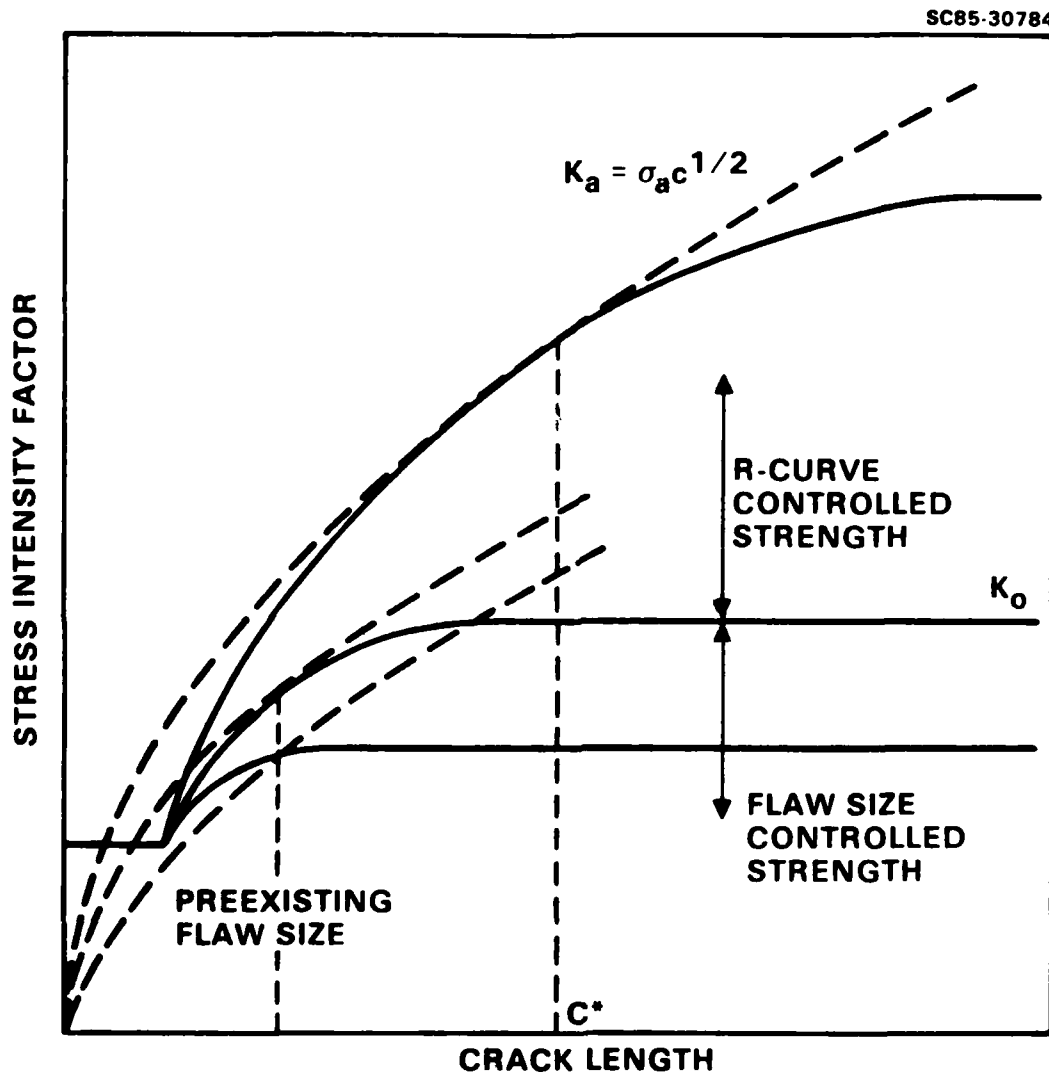


Fig. 11 Schematic representation of transition in strength characteristics with changing R-curves.

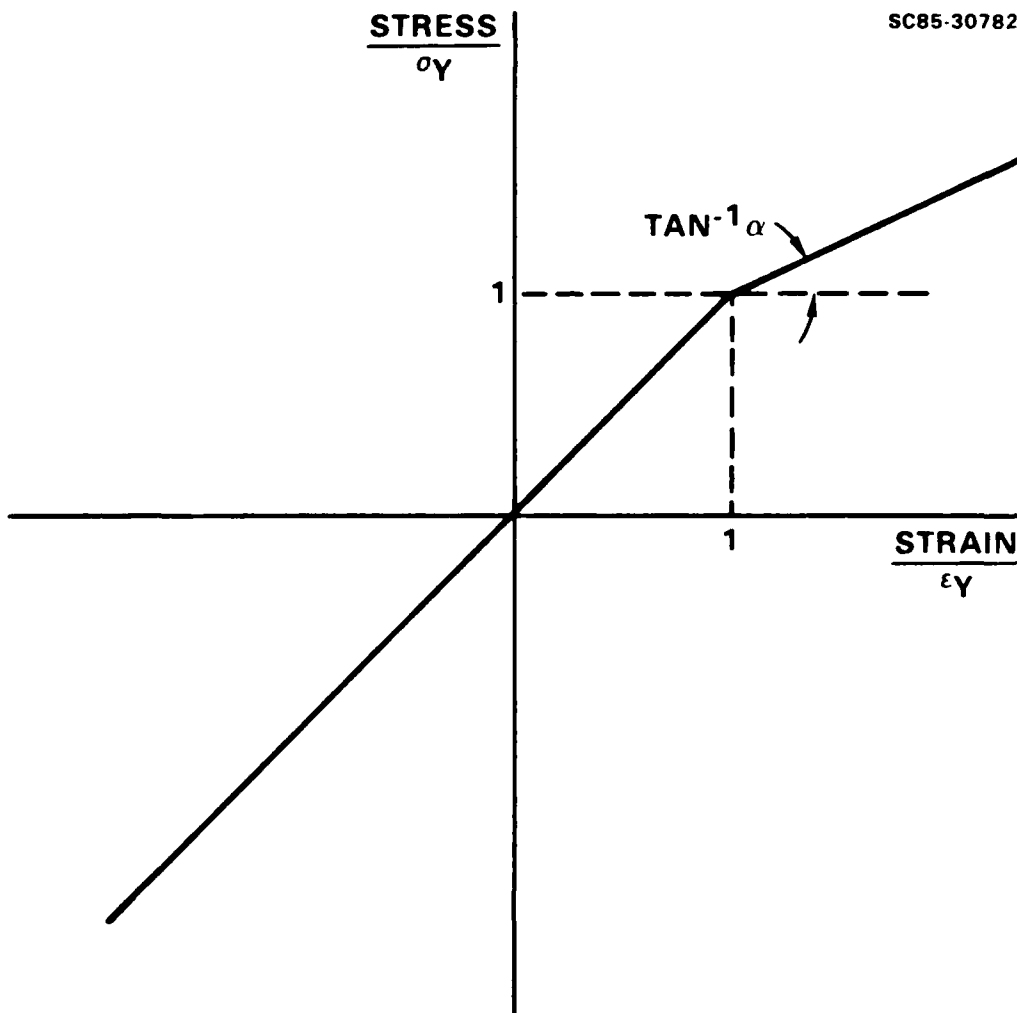


Fig. A1 Stress-strain curve used for calculation of stresses and strains in flexure.



SC5295.4FR

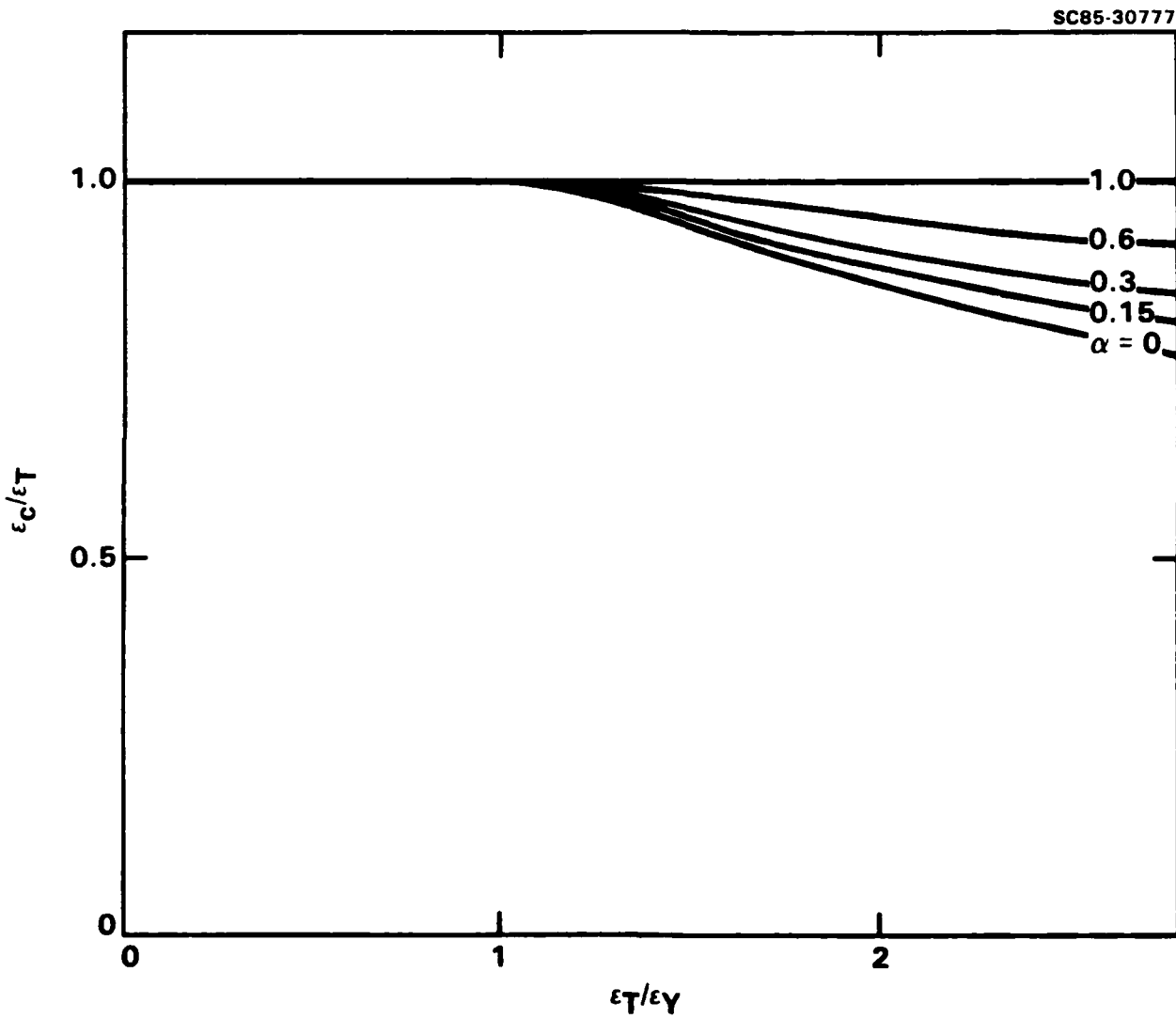


Fig. A2 Variation of the ratio of strains on the compressive and tensile surfaces with increasing flexural loading.

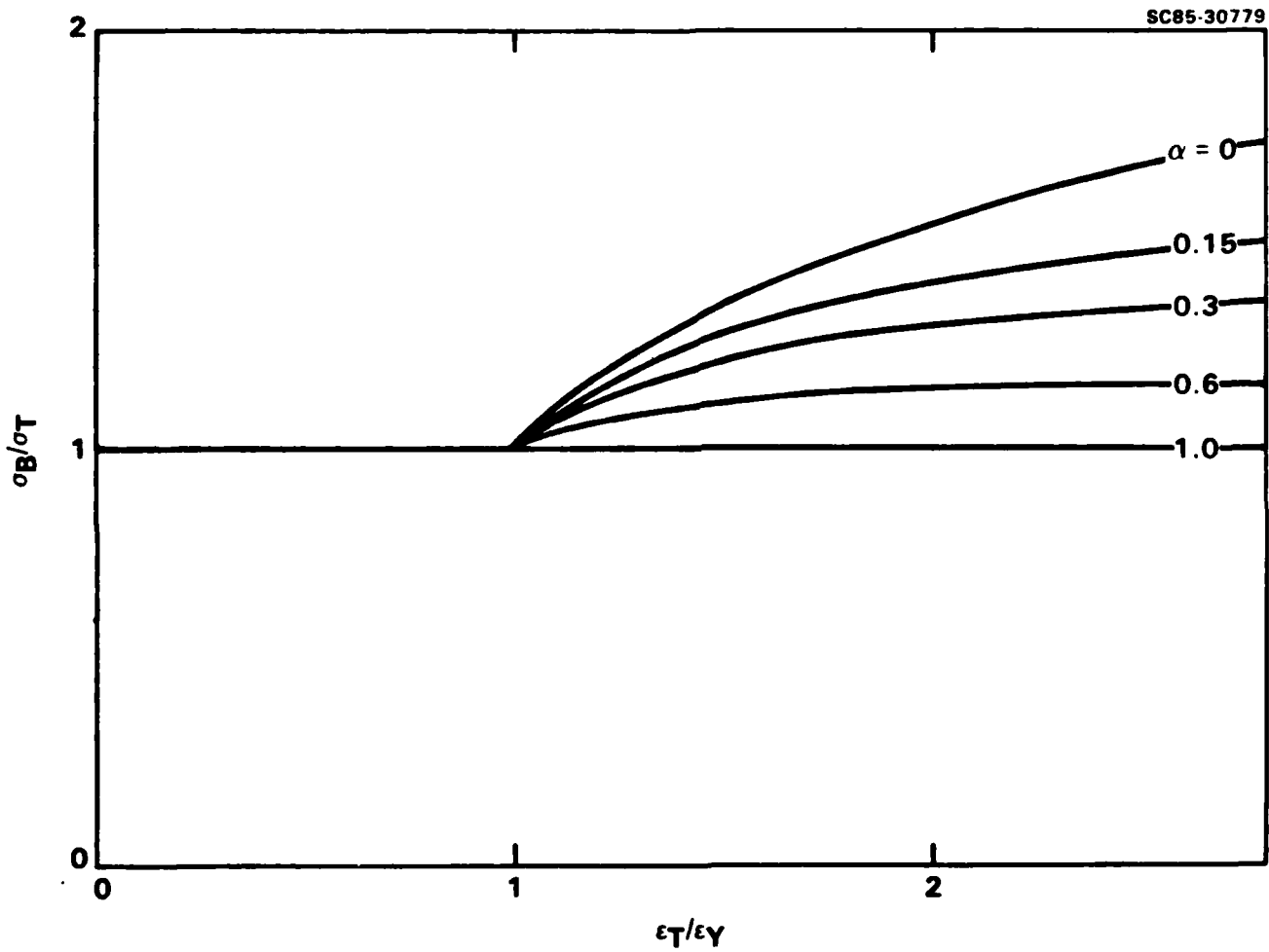


Fig. A3 Variation of the ratio of apparent flexural stress to the true stress on tensile surface with increasing strain on the tensile surface.

END

FILMED

10-85

DTIC